7

Main Linacs: Design and Dynamics

Contents

7.1 Introduction

The main linacs will accelerate electrons and positrons from an energy of 10 GeV to 250 GeV in the initial stage of running, and from 10 GeV to 500 GeV after upgrades to the rf system. For initial (upgraded) operation, trains of 90 bunches with 0.75×10^{10} (1.1×10^{10}) particles per bunch, and a 1.4-ns spacing between bunches, will be accelerated at a repetition rate of 180 (120) Hz.

There are two major design issues for the main linacs: the efficient acceleration of the beams and the preservation of the small beam emittances that are required to achieve the desired collision luminosity. The acceleration of the beams will be accomplished using X-band rf technology which is described in detail in Chapter 8. In this chapter, we discuss the design and operation of the linacs with the emphasis on the underlying beam dynamics that have driven the choices made in these regards.

The NLC linac design builds on the experience that has been gained over the last ten years from the operation of the SLC, in particular, in the development of beam-based alignment, tuning, and feedback techniques. Information from beam measurements are now routinely used in the SLC to align magnets, tune dispersion and chromaticity, compensate for accelerator structure misalignments, and to stabilize beam energy and orbits, including the beam-beam offset at the collision point. Such methods will also be crucial for the NLC operation as will become clear in this chapter. Their success in the SLC has given us confidence they will work in the NLC as well.

The NLC design also draws on the SLC operation experience in such areas as the transport of flat beams, the use of BNS damping, and linac energy management. From this, we have identified many things that need to be improved for the NLC. For example, drifts in the energy profile along the SLC linac have made tuning difficult, so in the NLC we are considering the use of beam-derived signals to keep the rf phases synchronous with the beams.

In areas where we cannot directly verify NLC operational issues with the SLC, we have built test facilities. These include ASSET for X-band structure wakefield measurements, ASTA and NLCTA for X-band accelerator technology testing, and the FFTB for final focus evaluation, although some of its features, such as quad movers, test linac concepts as well. Of these facilities, the NLCTA will provide the most direct test of the basic linac design in its ability to accelerate multibunch beams and to control the effects of beam loading. These facilities are discussed further in Chapters 8 and 11.

In this chapter, we begin with a discussion of parameters and specifications for the main linacs, followed by an overview (Section 7.3) of their design and layout. Many of the issues touched upon here (*e.g.,* alignment and stability, design of individual components, and instrumentation) will be treated in greater detail later in the chapter and elsewhere in this report, but Section 7.3 will provide a general orientation to the main issues and tradeoffs that have led to the present design.

Following the section on design and layout, we begin a detailed discussion of linac dynamics issues most closely related to emittance preservation. Of major importance are issues associated with the wakefields generated in the X-band accelerator structures by the beams. Although these structures will provide a high accelerating gradient, they will also heavily load the bunch train and will generate strong short- and long-range transverse wakefields when the bunches travel off-axis though them. Of particular concern is the long-range wakefield, which if not heavily suppressed, will resonately amplify the betatron motion of the bunch train by many orders of magnitude. Much work to date has been devoted to solving this problem, the outcome of which is an accelerating structure that incorporates both detuning and damping of the wakefield. Most of the details of the structure design are given in the next chapter: here, at the beginning of Section 7.4, we review how the wakefields, both longitudinal and transverse, were computed for this structure.

With this foundation, we next consider the dynamics issues associated with single-bunch and multibunch phase space, both longitudinal and transverse. These include operational issues such as the optimal single-bunch energy spread profile for BNS damping and the methodology used to compensate long-range beam loading. Most of the discussion, however, is devoted to the tolerances required to prevent significant emittance dilution from such sources as misalignments and jitter (the latter can be thought of as producing a dilution of the time-averaged emittance). In particular, we consider only bare tolerances in that we assume no benefit from a beam-based types of correction, including feedback.

In the next section, 7.5, we consider issues of alignment, stability, and feedback, with emphasis on the beam-based methods that will be required in cases where the bare tolerances cannot be met. Where data is available on error sources, we compare their size to the tolerances presented in Section 7.4 We will see, for example, that beam jitter due to ground motion should not be a major problem for the linacs.

Maintaining the quadrupole and accelerator structure alignment, however, will be a key aspect of NLC operation. Quad offsets will lead to dispersive emittance growth while the structure offsets will lead to wakefield related emittance growth. In both cases, beam-based methods will be required as the bare tolerances would be impossible to meet otherwise. The proposed methods will require accurate measurements the beam position. How this will be achieved is discussed later in this chapter.

The quad and structure alignment algorithms are examples of local types of correction in that they correct the problem at the source. Also discussed are non-local correction methods where trajectory bumps, kickers, etc., are used to cancel the dilutions after they have accumulated. We generally consider them fall-back methods since they are sensitive to variations in beam transport properties between the sources of the dilution and the correction point.

Another important feature of the NLC operation will be the use of feedback systems to maintain stability on timescales of seconds and longer. They will be used to stabilize both bunch energies and trajectories at various locations along the linac. Because of their importance, we review the performance of the SLC feedback systems.

The remaining sections of the chapter contain information on beam transport simulations, tolerances, operations, linac components, and instrumentation. Of particular interest, due to the very large number of components in the main linacs, is to quantify the reliability of the various systems; studies of this are just beginning and will be discussed in future revisions of this chapter.

7.2 Parameters and Specifications

7.2.1 System Boundaries

The main linac systems boundaries are from the exit of the bunch compressor complex to the entrance of the collimation system that leads to the final focus. The main linacs consist basically of X-band acceleration sections, interspersed with quadrupoles to focus the beam, along with the necessary diagnostics and supporting systems. The rf system feeding the main linac accelerating structures and the details of the design of those structures are discussed in the next chapter.

On each rf pulse, a train of up to 90 bunches enters the main linacs from the bunch compressor. The two main tasks of the main linacs are to accelerate the bunches to high energy and to minimize the growth of the beam emittance. Even with care taken to minimize emittance growth and development of transverse “tails” on the beam, it will be necessary to clip the tails to minimize backgrounds in the detector; the collimation systems needed to do this are discussed in Chapter 9.

	NLC-I			NLC-II		
	a	b	c	a	b	c
N (10^{10})	0.65	0.75	0.85	0.95	1.10	1.25
Bunches/Train		90			90	
Repetition Rate (hz)		180			120	
σ_z(μm)	100	125	150	125	150	150
Unloaded Gradient (MV/m)		50			85	
Multibunch Loading (%)	25.5	29.4	33.34	22.0	25.5	28.9
Multibunch Loading (MV/m)	-12.8	-14.7	-16.7	-18.7	-21.5	-24.6
Single-bunch Loading[a] (MV/m)	-0.2	-0.3	-0.4	-0.4	-0.5	-0.6
Average $\phi^b_{\rm rf}$ (°)	-15	-15.5	-16	-7.5	-8.2	-11.2
BNS Overhead (%)	3	3	3	3.5	3.5	3.5
Feedback Overhead (%)	2	2	2	2	2	2
Repair Margin (%)	3	3	3	3	3	3
$L_{\rm acc}$ (m)		8150			8834	
Number Structure		4528			4908	
$L_{\rm total}$ (m)		8807			9550	
$E^c_{\rm max}$ (GeV)	266.7	250	232.2	529	500	468

[a] Single-bunch loading only includes HOM contribution.

[b] Average rf phase for 0.8% FWHM energy spread.

[c] Including 10-GeV initial energy.

Table 7-1. *NLC linac parameters.*

7.2.2 Main Linac Parameters and Requirements

Parameters of the main linacs are listed in Table 7-1 for NLC-I, which has a 500-GeV center-of-mass energy, and NLC-II, which has a 1-TeV center-of-mass energy. The length of each of the two main linacs in NLC-I is 8.8 km. This will increase only slightly in the upgrade to NLC-II, with the bulk of the energy gain coming from an increase in the unloaded gradient from 50 to 85 MeV/m. This increase in gradient will be performed adiabatically by upgrading and doubling the number of klystrons which supply the rf power. It will be accompanied by an increase in beam charge which will leave the fractional beam loading roughly constant. However, the repetition rate will be decreased to keep total site power consumption from becoming too large. Since the total linac length required for NLC-II is not much longer than that for NLC-I, we will probably construct the full NLC-II linac length initially and use the additional length in NLC-I to attain beam energies slightly higher than 250 GeV.

For both NLC-I and NLC-II, three different parameter sets are listed. These correspond to the same rf power and linac length, but assume different bunch charges and bunch lengths. This leads to different loading through the linacs and therefore different final beam energies. The total beam energy is determined from the accelerating gradient, $Grad_{\rm rf}$, the average beam phase, $\phi_{\rm rf}$, and the single and multibunch beam loading:

$$\Delta E = L_{\rm acc} Grad_{\rm rf} \cos\phi_{\rm rf} (\%fdbk)(\%BNS)(\%off) - L_{\rm acc} q (k_{||\,\rm multi} + k_{||\,\rm single}) \quad . \tag{7.1}$$

In addition, there must be sufficient energy overhead for the energy feedback systems, the phase profile required for BNS damping, and the energy loss from klystron stations that have to be repaired. The value assumed for the klystron repair margin is roughly 50% larger than that needed in the SLC linac. The overhead assumed for the energy feedback is similar to that used in the SLC. Finally, the additional energy needed for BNS damping arises because the linac will

	NLC-I			NLC-II		
	a	b	c	a	b	c
N (10^{10})	0.65	0.75	0.85	0.95	1.10	1.25
σ_z (μm)	100	125	150	125	150	150
$\gamma\epsilon_{x\,\mathrm{inj}}$($10^{-6}$ m-rad)		3.6			3.6	
$\gamma\epsilon_{y\,\mathrm{inj}}$($10^{-8}$ m-rad)		4			4	
$\sigma_{\epsilon\,\mathrm{inj}}$(%)		<1.5			<1.5	
$\gamma\epsilon_{x\,\mathrm{ext}}$($10^{-6}$ m-rad)		4			4	
$\gamma\epsilon_{y\,\mathrm{ext}}$($10^{-8}$ m-rad)	7	9	11	9	11	13
$\Delta E/E_{FWHM\,\mathrm{ext}}$ single bunch (%)		0.8			0.8	
$\Delta E/E_{FWHM\,\mathrm{ext}}$ train (%)		1.0			1.0	

Table 7-2. *NLC linac emittance requirements*

not be operated at a constant rf phase. Instead, the rf phases are set in the first part of the linac to produce the desired BNS bunch energy spread; in the remainder of the linac, they are set to achieve a final energy spread that is within the final-focus bandwidth. This will be discussed further in Subsection 7.4.3.

The design-normalized emittance of the bunches entering the main linacs is $\gamma\epsilon_x = 3.6 \times 10^{-6}$ m-rad, $\gamma\epsilon_y = 4.0 \times 10^{-8}$ m-rad, and the energy is 10 GeV. It is the task of the main linacs to accelerate the bunches to ∼250 GeV (NLC-I) or ∼500 GeV (NLC-II), while preserving the low transverse emittance and maintaining the small final beam energy spread; these requirements are listed in Table 7-2.

The three parameter sets listed for NLC-I and NLC-II reflect a tradeoff in bunch charge versus beam size where the luminosity is kept nearly constant. As discussed in the introduction to this document, this is the main tradeoff that remains in a linear collider design when all constraints are taken into account. Larger beam sizes are desirable since they loosen many of the tolerances. However, increasing the beam charge to compensate the loss in luminosity produces problems related to beam power, and generally leads to tighter wakefield-related tolerances. The three parameter sets each represent compromises among these competing effects: together they span the range of operating conditions that we consider reasonable.

In this chapter, we will concentrate the mid-range parameters, that is, sets NLC-Ib and NLC-IIb. Note that we have allowed for over 100% vertical emittance growth in the linacs in these cases. This lets us set fairly conservative tolerances on the accelerator structure alignment. However, we believe that we will do better than these tolerances as we gain more experience with X-band accelerator construction and operation.

7.3 System Design

7.3.1 Design Overview

Although the layout of the main linacs is fairly simple, an array of X-band accelerator structures interleaved with a FODO quadrupole lattice, one faces a number of challenges to accelerate low-emittance bunch trains without significantly degrading the beam phase space. The X-band structures that provide a high-acceleration gradient also heavily load the beam, so careful control of the rf pulse shape will be needed to achieve the small beam energy spread that is required at the end of the linac. The X-band structures also have the drawback that large transverse wakefields, both long-range (bunch-to-bunch) and short-range (intra-bunch), are generated when the bunch train passes off-axis through the structures. Although damping and detuning of the dipole modes of the structure will be used to suppress the long-range wakefield, and autophasing will be used to offset the short-range wakefield effect on betatron motion, the structures will still have to be aligned precisely to limit emittance growth from both short-range and long-range wakefield effects. The small bunch sizes also make the beam sensitive to other emittance growth mechanisms such as dispersion from quadrupole misalignments, focusing from the ions generated in the residual gas of the beam-line vacuum chambers, and dilution from beam trajectory jitter, like that caused by vibrations of the quadrupole magnets.

Most of the deleterious effects will be limited by design. For example, the quadrupole magnet power supplies will be chosen to be stable enough not to cause significant beam trajectory jitter. For some of the effects, however, we will rely mainly on measurements of the beam properties to control emittance growth. In particular, beam trajectory measurements will be used to adjust the positions of the quadrupoles and structures to minimize the emittance growth caused by their misalignment. For this purpose, each quadrupole and structure in the linacs will contain a beam position monitor (BPM), and will be supported by movers that can be remotely controlled (*e.g.,* like the magnet movers in the FFTB).

A beam-based approach will also be used in a trajectory feedback system to suppress low-frequency jitter of the bunch train as a whole, and if necessary, bunch-to-bunch position variations within the train (special multibunch BPMs will be used in this case). These feedbacks will be included in each of five instrumentation regions that will be located along the linacs. These regions will also include high-dispersion sections so that bunch energy and energy spread can be measured and used for rf control feedback. As with the operation of the SLC, if the feedback and alignment algorithms fail to suppress emittance growth to the desired level, non-local types of tuning will be used, such as orbit bumps. To aid in this tuning, and to monitor the beam phase space, the instrumentation regions will also contain beam size monitors.

Finally, we note some of the machine protection strategies that will be used to deal with the high-power beams. Initial tuning and recovery from beam shut-off will be done by running with a single bunch per pulse, and with a larger than nominal emittance so that the bunch will not damage the beam pipe if it were steered into it. A series of thin spoilers, one per structure, will be the first material intercepted by the bunch, and will disperse the resulting shower of secondary particles to prevent damage to other beam line elements. For nominal beam operation, a series of safeguards will be used to shut off the beam before it hits the beam pipe, and to prevent fast changes ($<$ pulse period) that could steer the bunches into the beam pipe.

7.3.2 Linac Optics

The linac focusing system is designed to contain the beam transversely as it is accelerated. In the NLC linacs, there are many effects that will dilute the transverse projected emittance of the beams. The three primary sources of emittance dilution are:

- Short- and long-range transverse wakefields.
- Dispersive and chromatic effects.
- Transverse jitter induced by quadrupole vibration.

Ideally, one would like to design a lattice that will minimize all three of these effects without significantly increasing the length of the linac. Unfortunately, these three sources of dilution impose opposing constraints on the focusing lattice. The wakefield dilutions are minimized by increasing the focusing strength, while the other dilutions are increased by the stronger focusing. In the NLC main linacs, we will use beam-based alignment of the quadrupoles and BPMs to minimize the dispersive emittance growth; the technique for this is straightforward. Thus, in principle, the optimization becomes a balance between the dispersive and jitter dilutions and the wakefield dilutions.

In practice, the optimization is actually a balance between the additional length due to the strong focusing and the wakefield dilutions. That is, we want to have a sufficiently strong focusing system so that the wakefield dilutions are small but not an excessively strong lattice that would unnecessarily increase the length of the linacs due to the additional quadrupole magnets that would be required. A parameter that characterizes the strength of the wakefield relative to the focusing is the BNS energy spread needed for autophasing: autophasing is the condition where the chromatic growth of a beam performing a coherent betatron oscillation exactly cancels the wakefield growth and thus the beam oscillates as a rigid body.

The energy spread required for autophasing can be estimated from a two-particle model as:

$$\sigma_{\delta\,\mathrm{BNS}} \approx \frac{N r_0 W_\perp(2\sigma_z)}{8\gamma}\frac{L_c^2}{6}\left(1+\frac{3}{2}\mathrm{ctn}^2\frac{\psi_c}{2}\right) \ , \tag{7.2}$$

where N, r_0, and $W_\perp$ are, respectively, the number of particles per bunch, the classical electron radius, and the transverse wakefield. In addition, L_c and ψ_c are the FODO focusing cell length and the betatron phase advance through the cell. A shorter cell length and larger phase advance yield stronger focusing and smaller BNS energy spreads.

In the NLC linacs, we have limited the BNS energy spread to less than 1.6%. This yields tolerances on the trajectory control and alignment of the accelerating structures that are reasonable using high-resolution BPMs and a beam-based alignment technique for the structures. For comparison, in most of the SLC linac $\sigma_{\delta\,\mathrm{BNS}} \gtrsim 4\%$.

Lattice Design

The main linacs are based upon simple FODO cells where the quadrupoles are separated by an integral number of pairs of accelerator structures—see discussion in Section 7.3.3. Two structures are paired together since this simplifies the waveguide routing that is required. For the NLC linacs, we considered two basic approaches: (1) placing quadrupoles, all having the same length, after every structure pair and (2) increasing the number of structure pairs between quadrupoles as $(E/E_0)^\alpha$ where α typically varies between 0.2 and 0.8.

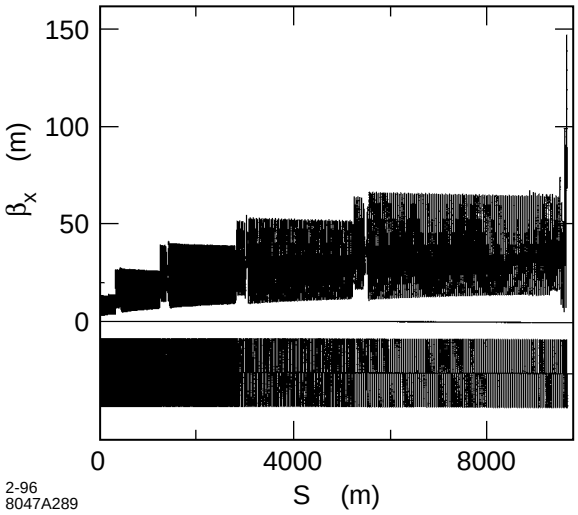

Figure 7-1. *Horizontal beta function in the NLC-II linacs.*

While the first option has the most flexibility, allowing one to set the "optimal" lattice regardless of the final beam energy, it is very space inefficient. This arises because many quadrupoles are located in regions where the horizontal and vertical beta functions are nearly equal. Thus these quadrupoles do not contribute to the net focusing and are wasting space.

In the cases we studied, the length of the linac occupied by the quadrupoles was more than 15% with the first option while it was roughly 7% with the second option. For this reason and because we feel that it can provide sufficient flexibility, we have chosen to adopt the second approach.

For NLC-I and NLC-II, the primary center-of-mass energy range that needs to be considered is between 500 GeV and 1 TeV. We have designed a lattice where the quadrupole spacing is increased by pairs of accelerating structures such that the cell length scales with $\alpha \sim 0.5$ when the center-of-mass energy is roughly 700 GeV; this is a compromise between the 500-GeV center-of-mass energy and the 1-TeV center-of-mass energy. This lattice will provide sufficient focusing at even lower center-of-mass energies, and the focusing can be decreased at the higher energies to decrease the sensitivity to quadrupole vibration.

To decrease the final beam energies much below 250 GeV while constraining the beam emittance dilution due to the transverse wakefields would be difficult. In this case, one would likely add a bypass line to skip part of the linac. For example, to operate the collider at 92 GeV to study the "Z_0" boson would only require the first fifth of the accelerating structures. The wakefields in the remaining structures simply increase the longitudinal and transverse emittance dilution and thereby decrease the performance of the collider.

In the lattice, the cell lengths increase in five steps, from roughly 8-m cells to 40-m cells, and the beta functions must do the same. We have matched across these transition regions without any significant increase in sensitivity. The horizontal and vertical beta functions for the NLC-II linacs are plotted in Figures 7-1 and 7-2. Notice that immediately following a transition point, the lattice contains a diagnostic section where the focusing is slightly weaker and is less uniform to provide optimal conditions for the emittance measurements; these diagnostic sections are discussed in Section 7.3.4. Figure 7-3 shows the horizontal and vertical phase advance per cell, and Figure 7-4 shows the horizontal and vertical BNS autophasing energy spreads. Figure 7-5 shows the location of the diagnostic stations on a plot of the horizontal dispersion.

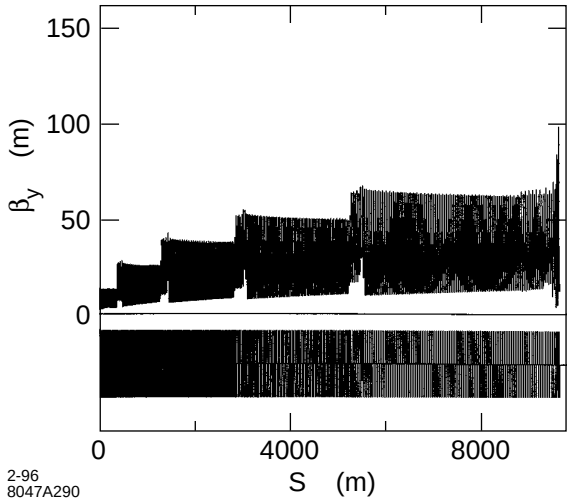

Figure 7-2. *Vertical beta function in the NLC-II linacs.*

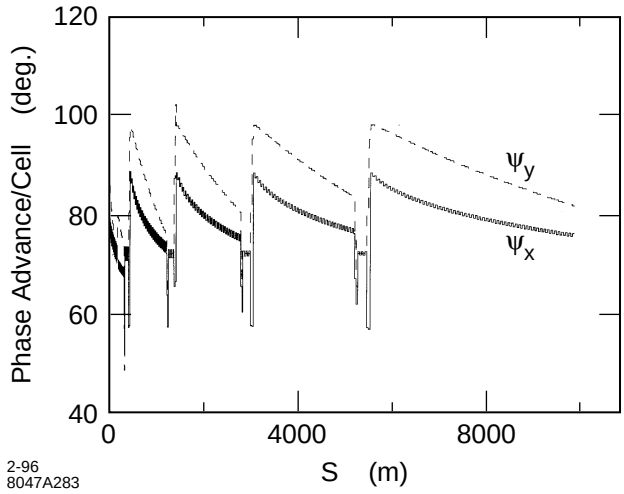

Figure 7-3. *Horizontal and vertical phase advance in the NLC-II linacs; the vertical phase advance is larger than the horizontal to optimize the focusing in the vertical plane.*

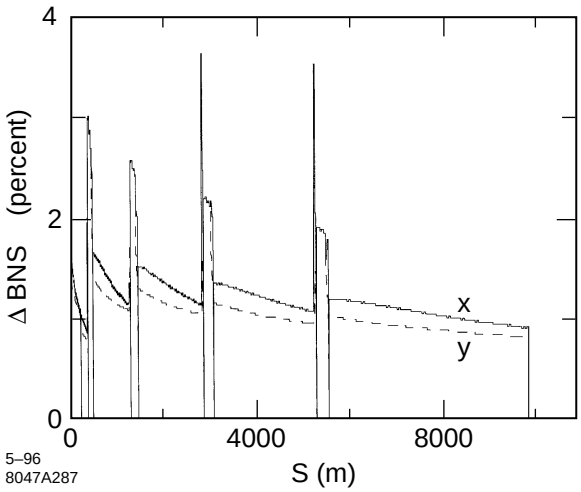

Figure 7-4. *Horizontal and vertical BNS autophasing energy spreads for NLC-IIb; the large values occur in the diagnostic regions.*

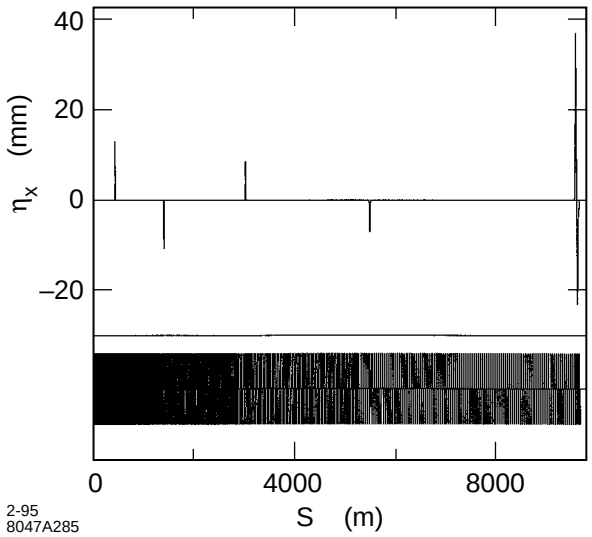

Figure 7-5. *Horizontal dispersion function in the NLC-II linacs; note that the diagnostic stations are located at the non-zero dispersion regions.*

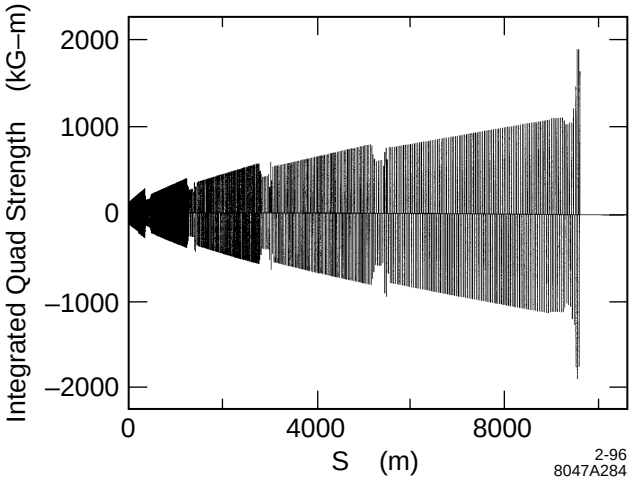

Figure 7-6. *Integrated quadrupole strengths in NLC-IIb lattice.*

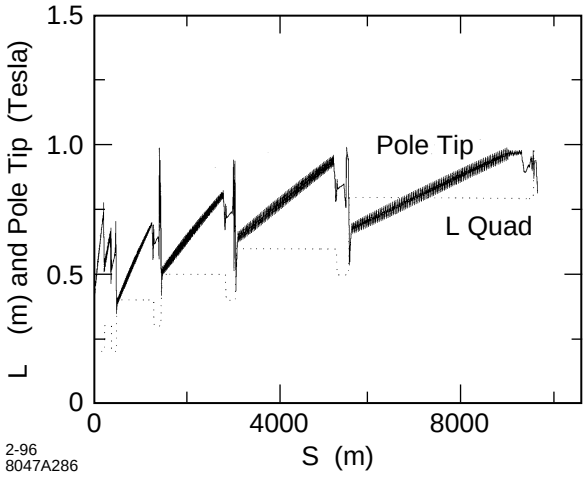

Figure 7-7. *Quadrupole lengths (dotted) and pole-tip fields (solid) in NLC-IIb lattice.*

The integrated quadrupole strengths required for the NLC-IIb lattice are plotted in Figure 7-6. The quadrupoles are assumed to have a 0.7-cm pole-tip radius. To keep the pole-tip fields reasonable, the quadrupole lengths are increased as the cell lengths are increased. The linac lattice uses five different quadrupole lengths: 0.2 m, 0.3 m, 0.4 m, 0.6 m, and 0.8 m in the regular lattice, while the final energy diagnostic section assumes a 1-m quadrupole with a 5-mm pole-tip radius; these longer quadrupoles are similar to those required in the collimation and final focus sections. The assumed lengths and the corresponding pole tip fields are plotted in Figure 7-7; note that some of the matching quadrupoles in the diagnostic sections are far too strong and must be lengthened.

Finally, we have studied the bandwidth of the linacs assuming that injection energy was correct but the accelerating gradient was too high or too low. The results are plotted in Figure 7-8 as a function of $B_{\rm mag} - 1$. The parameter $B_{\rm mag}$ is equal to:

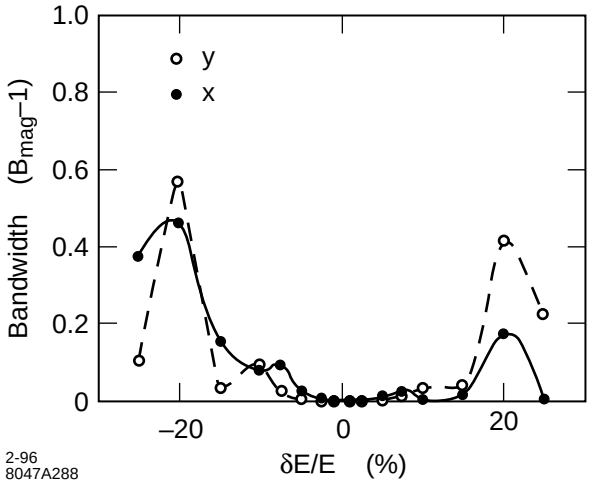

Figure 7-8. *Bandwidth of the NLC-II linacs plotted in terms of $B_{\rm mag}-1$ which is proportional to the emittance increase after filamentation. The energy deviation is due to an increased or decreased acceleration gradient.*

$$B_{\rm mag} = \frac{1}{2}\left[\frac{\beta^\star}{\beta} + \frac{\beta}{\beta^\star} + \left(\alpha\sqrt{\frac{\beta^\star}{\beta}} - \alpha^\star\sqrt{\frac{\beta}{\beta^\star}}\right)^2\right] \quad , \tag{7.3}$$

where $\beta^\star$ and $\alpha^\star$ describe the beam ellipse and are equal to the lattice functions β and α when the beam is "matched" to the lattice. With this definition, $B_{\rm mag}$ times the beam emittance is equal to the emittance after filamentation. Thus, when $B_{\rm mag} - 1$ equals one, there is 100% emittance growth. Figure 7-8 indicates that the optical bandwidth of the linacs is more than sufficient.

7.3.3 Beam Line Layout: Normal Sections

The main linacs are basically an array of X-band accelerator structures interleaved with a FODO quadrupole lattice. In this section, we describe the general layout and components of these "normal" beam line regions. The special diagnostic regions of the main linacs are described in Section 7.3.4. Further details on components and instrumentation are given in Sections 7.9 and 7.10, including newer concepts for the support system for the beam line components.

Structures

Figure 7-9 shows the beam-line layout near the beginning of the linacs where there is a quadrupole between each pair of accelerator structures; Figure 7-10 shows the end view and a close-up side view of the linac components. Note that the accelerator structures are supported in pairs on a common strongback, and that the strongback itself is supported by mechanical movers, which we call structure movers. Grouping the structures in pairs is motivated by the fact that they have a common rf feed and therefore are mechanically constrained, at least for large movements. The two structures will each be supported on the strongback at six locations and will be aligned on the strongback before installation (five of the six supports can flex to allow for thermal expansion of the structure along the beam axis). It will still be possible to adjust the six supports *in situ*, although not easily, given that an alignment precision of about 10 μm will be required.

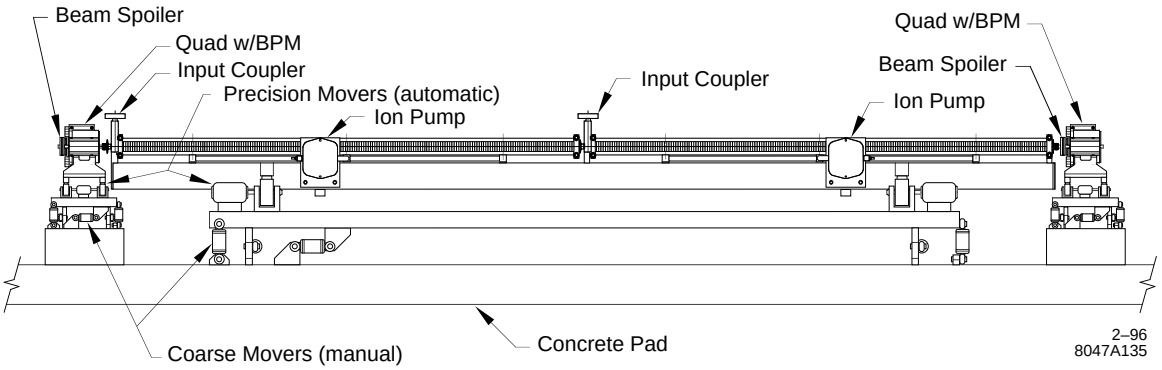

Figure 7-9. *Side view of linac components near the beginning of the linacs, where there is a quadrupole between each pair of accelerator components.*

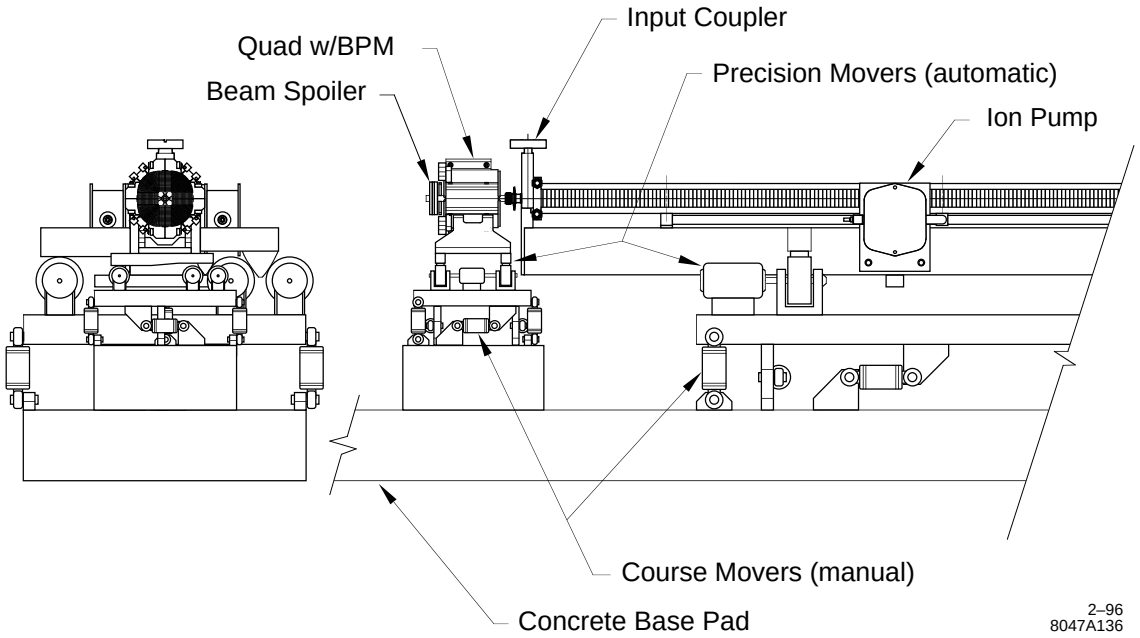

Figure 7-10. *End view and close-up side view of the linac components.*

The structure mover system will be similar to that used to move the SLC final focus triplet. The movers will provide independent horizontal and vertical positioning control at two points along the strongback, and will be used to remotely align the two structures as a whole relative to the beam trajectory. The alignment correction will be based on measurements of beam-induced signals from the structures, and the position changes will be made via five stepper motors that drive off-axis cams. Steps as small as 1 μm will be achievable over a range of ± 1 mm. Structure roll can be adjusted as well but will not be changed. This capability is a byproduct of using a mounting system that does not over-constrain the object that is being supported.

The structure movers will be attached to a common girder that will be attached to the beam line support pedestal via manually adjustable supports. These girder supports will be used to set the initial position and orientation of the structure pairs, and will have a ± 1-cm range of travel. They will also be used if a global realignment of the beam line is necessary due to ground settling.

Quadrupoles

Near the beginning of each linac, there will be a quadrupole magnet after each structure pair (Figure 7-9). However, the separation of the quadrupoles will increase in two-structure increments along the linac, from one pair of structures to five pairs at the end of the linac. These quadrupoles will form a FODO optical array as discussed in Section 7.3.2.

The quadrupoles, each of which will contain a BPM, will be moved as one unit for alignment purposes. Each quadrupole/BPM unit will be mounted on a magnet mover, which in turn will be mounted on a manually adjustable support. This system will have the same adjustment capability as was described for the structures, but the movers will be similar to those used in the FFTB.

BPMs

A stripline BPM will be located inside each quadrupole and will contain four strips at an inner radius of 5 mm with strip lengths of 105 mm. This length was chosen because it makes the period between the forward and reflected pulses from a single bunch equal to half of the bunch spacing, which is optimal for multibunch measurements. Since this length is shorter than the minimum quadrupole length, the addition of the BPMs will not significantly increase the beam-line length.

Spoilers

After each structure, there will be a spoiler that will be the first material hit if the beam is steered far off-axis. The spoiler will be a titanium disk that is 0.2-radiation-lengths long (about 8 mm), with a 2-mm inner radius and a 1-cm outer radius. For normal beam operation, it will do little to prevent damage to the beam pipe, but for tuning, it allows a single high-emittance bunch to intercept the beam pipe without causing damage; the Machine Protection System (MPS) is discussed further in Section 7.8. The integrated transverse wakefield kick due to a spoiler is about 10% that of the wakefield due to a single accelerator structure.

7.3.4 Beam Line Layout: Special Diagnostic and Control Sections

In a linac, it can be difficult to localize sources of emittance dilution, optical errors, and beam energy errors. If these errors propagate a sufficient distance, the emittance dilutions and optical errors will filament into unrecoverable

emittance dilution and the beam energy errors will lead to large variations in the betatron phase. The relevant length scale is the number of betatron oscillations. The NLC linacs are sufficiently long (roughly 80 betatron wavelengths compared to 30 wavelengths in the SLC linac) that it is important to measure the beam emittance and energy at multiple points along the linacs. In addition, because trajectory errors will also filament into unrecoverable emittance dilution, it is important to provide fast feedbacks that will stabilize the trajectory at multiple points along the linacs.

To monitor the beam emittance, energy, and trajectory, there are four diagnostic stations located in each linac and one station located at the end of each linac. The stations within the linacs are located at 400, 1300, 2900, and 5300 m; they are concentrated more closely at the beginning of the linacs because the beam is more sensitive at the low-energy end. In terms of betatron phase advance, these placements (including the station at the end of the linac) are located at 10, 22, 36, 54, and 78 oscillations. The diagnostic stations will provide five main functions:

- Beam emittance measurements.
- Energy and energy spread measurements.
- Fast feedback correctors.
- Bunch-by-bunch measurement and trajectory control.
- Beam dump.

Each of these will be described after briefly discussing the layouts.

The diagnostic stations are constructed from six FODO cells, each of which is roughly one-m longer than a normal FODO cell. This additional space is used by the diagnostics and kickers which are located near the quadrupole magnets. The accelerating structures occupy the middle of the cells just as they do in normal FODO cells. The quadrupole and accelerating section supports and girders are also identical to those of the main linac sections.

In addition to the six lengthened FODO cells, each of four diagnostic sections within each main linac includes a chicane which introduces dispersion for the energy and energy spread measurements; the length of the chicanes and matching quadrupoles is roughly equal to that of a single FODO cell. Finally, a much higher-resolution energy diagnostic section with a length of roughly 100 m is located at the end of each linac. This final energy diagnostic section also provides a net bending angle to compensate for the collimation section that follows the linac.

Emittance Measurement

The beam emittance measurements are performed using laser wire scanners located at different betatron phases which allows the beam matrix to be measured without changing the optics between scans. Only three independent X and Y wire scanners are needed to reconstruct the uncoupled 2×2 X and Y beam matrices. This effectively measures the projected horizontal and vertical emittances along with the beta and alpha parameters that describe the beam. If one also wants to measure the off-diagonal X and Y coupling terms, then at least four scanners with X, Y, and diagonal wires (U-wires) are needed since there are ten rather than six independent parameters that describe the beam. In this case, the horizontal and vertical phase advances must be separated to get independent measurements of the coupling terms.

In the NLC linacs, we do not expect betatron coupling to be a significant source of emittance dilution; the roll tolerances on the quadrupoles are relatively loose. Regardless, when commissioning the linacs or tracing sources of emittance dilution, it is important to be able to verify the degree of coupling in the beams. Finally, experience with the SLC emittance measurements suggests using an additional wire scanner to over-constrain the measurement

Station		Energy (GeV)	S (km)	σ_x (μm)	σ_y (μm)
NLC-Ib	Diag 1	20	0.4	26	7
	Diag 2	45	1.3	21	6
	Diag 3	90	2.9	18	5
	Diag 4	154	5.3	15	4
	Diag 5	245	8.6	12	3
NLC-IIb	Diag 1	30	0.4	22	6
	Diag 2	75	1.3	17	5
	Diag 3	155	2.9	14	4
	Diag 4	280	5.3	11	3
	Diag 5	490	9.4	8	2

Table 7-3. *Beam sizes at laser wire scanners in linac diagnostic stations for the NLC-I and NLC-II.*

and provide an estimate of the measurement error; this additional scanner also provides a backup if one scanner fails. Thus, each of the diagnostic stations includes five laser wire scanners which can measure the emittances and coupling while providing an estimate of the measurement accuracy.

The wire scanners are located near maxima of the vertical beta function where the vertical beam size is largest and the aspect ratio σ_x/σ_y is smallest. The beam energy and beam sizes at the wire scanners are listed in Table 7-3 assuming normalized emittances of $\gamma\epsilon_x = 3.6 \times 10^{-6}$ m-rad and $\gamma\epsilon_y = 4 \times 10^{-8}$ m-rad; these emittances are smaller than those expected through most of the linacs. To optimize the diagonal measurements, the U-wires should be aligned at an angle given by the inverse tangent of the beam aspect ratio. For the NLC linacs, this corresponds to an angle of roughly 15 degrees. The laser wire scanners should be optimized to measure vertical beam spots in the range $1.6\,\mu\text{m} \lesssim \sigma_y \lesssim 20\,\mu\text{m}$; these spot sizes correspond to a vertical emittance ranging from $\gamma\epsilon_y \lesssim 6 \times 10^{-7}$ m-rad at 20 GeV to $\gamma\epsilon_y \gtrsim 3 \times 10^{-8}$ m-rad at 500 GeV.

Energy and Energy Spread Measurement

The beam energy and energy spread is determined by measuring the trajectory and beam size in dispersive regions. The dispersion is generated by chicanes in the linacs and by short arc sections at the end of the linacs. The chicanes produce a maximum transverse displacement of roughly 1 cm and do not have a net bending angle or net transverse displacement. The arc sections at the ends of the linacs provide a total bending angle of roughly 0.5 mr to compensate for bending in the collimation sections that follow the linacs.

The locations, maximum dispersion values, and lengths of the energy diagnostic sections are listed in Table 7-4 for the NLC-II; the stations have the same length and dispersion in the NLC-I, but the beam energy differs because of the lower accelerating gradient. In all cases, the lengths and strengths of the systems were adjusted to limit the emittance growth due to synchrotron radiation to ~1%. Finally, the sections will cause the beam phase and bunch length to change as a function of the beam energy and energy spread. These changes are quantified by the value of the R_{56} and are very small. Assuming a 10% energy error through the entire linac, the bunch length will be increased by less than 2% and the beam phase will be changed by 0.3° which is insignificant compared to the 10% energy error. The values of the R_{56}, as well as the emittance growth due to the synchrotron radiation, are also listed in Table 7-4; in the NLC-I, the R_{56} values are the same, but the emittance growths are negligible since the growth depends upon the sixth power of the beam energy.

Station	E (GeV)	η_x (mm)	Length (m)	R_{56} (μm)	I_5 (1/m)	$\Delta\epsilon_x/\epsilon_x$ (%)
Diag 1	32	13	8	-125	1.6×10^{-10}	0.1
Diag 2	80	11	16	-41	4.7×10^{-13}	0.1
Diag 3	165	8.6	23	-17	1.5×10^{-14}	0.3
Diag 4	290	7.0	30	-9	8.4×10^{-16}	0.4
Diag 5	500	37	110	-4	7.9×10^{-17}	1.2

Table 7-4. *Parameters of linac energy diagnostic stations in the NLC-II.*

Station	η_x (mm)	$\delta E/E$ Res. (%)	$\sigma_{x\beta}$ (NLC-I)(μm)	σ_ϵ Res. (%) (NLC-I)	σ_ϵ Nom. (%)
Diag 1	13	0.08	37	0.34	0.8
Diag 2	11	0.09	28	0.30	1.0
Diag 3	8.6	0.12	25	0.32	1.1
Diag 4	7.0	0.14	24	0.34	0.8
Diag 5	37	0.03	21	0.06	0.3

Table 7-5. *Energy resolution of energy diagnostic stations for NLC-I and NLC-II.*

In the chicanes, the beam energy measurement will be performed using a single BPM located at the maximum of the dispersion, and several BPMs located in nearby nondispersive regions. These latter BPMs will be used to remove the dependence on the incoming trajectory. The BPMs at the high dispersion points will differ from the normal linac BPMs in that they will need roughly twice the horizontal aperture. The primary purpose of the energy measurement is to track changes in the beam energy over time. These energy changes lead to variations in the phase advance along the linacs which can lead to changes in the beam emittances and trajectories, and the feedback system efficiencies. In the NLC, we would like to limit the phase advance variations to roughly 15°. This requires limiting the beam energy changes to 0.5% at the beginning of the linacs and 0.25% at the end of the linacs.

The expected resolution of the energy measurements is listed in Table 7-5 for the NLC-I and NLC-II, assuming a systematic error of 10 μm on the BPM measurement. This error is assumed to arise from both the stability of the BPM measurement and the resolution on determining the incoming trajectory from the surrounding BPMs which are in nondispersive regions. These different measurements are insensitive to the absolute value of the bending fields or the horizontal alignment of the BPM. In addition, assuming that the bending fields have been measured with a relative error of 10^{-3}, the absolute beam energy can be calibrated to less than 1% by varying the chicanes.

In the final energy diagnostic, the absolute beam energy can be calibrated much more accurately by measuring the angular separation of the synchrotron radiation generated at the beginning and end of the bending magnets. In this case, it should be straightforward to attain an absolute measurement with a relative error less than 10^{-3}. A similar procedure is used in the SLC final focus beam dump with a relative accuracy of roughly 2×10^{-4}.

In addition to the beam energy measurements, the chicanes and arc sections will provide energy spread measurements. The energy spread will be determine from either the synchrotron light spot size or a laser wire scanner. The resolution, estimated from the ratio of the dispersion to the betatron spot size for a horizontal emittance of $\gamma\epsilon_x = 4 \times 10^{-6}$ mr, is listed in Table 7-5 for the NLC-I; the values for the NLC-II are roughly 30% smaller. The nominal beam energy spread, which is much larger than the expected resolutions, is also listed.

It is envisioned that the chicanes will be used during normal operation to continuously measure the energy and energy spread. Regardless, the vacuum chamber through the chicanes will be designed to allow the bending fields to be varied continuously from zero to full excitation and to accept beams with an energy as low as 50% of nominal. This range

Station	Energy (GeV) (NLC-I/NLC-II)	Corrector Strength [G-m] (NLC-I/NLC-II)
Diag 1	20 / 30	3 / 4
Diag 2	45 / 75	4 / 6
Diag 3	90 / 155	6 / 10
Diag 4	155 / 280	8 / 14
Diag 5	245 / 490	12 / 25

Table 7-6. *Fast Feedback corrector strength in the NLC-I and NLC-II*

of conditions requires a horizontal aperture that exceeds twice the nominal beam displacement in the chicane. In a chicane, the maximum displacement is equal to the peak dispersion function which is listed in Table 7-5 and varies between 13 mm and 7 mm. A vacuum chamber aperture of 3 cm by 1 cm in cross-section is more than sufficient.

Fast Feedbacks

At each diagnostic station, there are fast trajectory feedbacks that will control the horizontal and vertical trajectories. The feedback systems consist of horizontal and vertical pairs of dipole correctors followed by 10 high-resolution BPMs. The horizontal correctors are located at the first two horizontally focusing quadrupoles in the diagnostic sections while the vertical correctors are located at the adjacent defocusing quadrupoles. The BPMs are located at the subsequent focusing and defocusing quadrupoles.

To prevent the dipole correctors from driving the beam into the vacuum chamber, the corrector strength will be limited so the maximum trajectory deflections are less than 100 μm; the maximum required strengths are listed in Table 7-6. The feedback systems need to operate at the full 180-Hz repetition rate. Thus, the correctors and the vacuum chamber should be designed so the fields attain a consistent slew rate.

For more details of the fast feedback system see Section 7.5.3.

Bunch-by-Bunch Trajectory Control

In addition to the fast feedback for the bunch train trajectory, we will implement high-speed vertical kickers to realign the bunches in a train. This system is designed to compensate for the long-range transverse wakefields induced by accelerator structure offsets. The high frequency kickers will be short striplines separated by roughly 90° in betatron phase; details are described in Section 7.5.4. Because the system is designed to correct static offsets of the structures, it will be controlled by a slow feedback system.

Beam Dumps

At this time, the only beam dumps we are planning for the linacs are ones that will be located at the ends. Beams would be deflected to the dump by a 180-Hz kicker magnet so that the beam direction can be switched from the dump line to the collimation section in a single interpulse period. The dump line begins in the beta matching section for the collimation region; this is located after the final energy diagnostic station and consists of drifts roughly 100 m in length. Although a detailed design does not yet exist, at 500 GeV, an integrated field of 5.6 kg-m will deflect the beam by 2 cm after a drift of 60 m. This would allow a simple septum to further deflect the beam into the dump line. The kicker field of 5.6 kg-m is roughly 75% larger than the field of the 2–9 single-beam dumper in the SLC.

For more details of the beam dump, see Chapter 11.

7.3.5 Site Requirements and Tunnel Layout

Since the main linacs are the largest components of the NLC, the impact of the site on their cost and operation will be the dominant factor in choosing a location to build the accelerator. Although a systematic study of the site requirements has yet to be done, several factors that will impact the site selection can be readily identified. For example, the beam line must be located at least 20 ft below ground to provide radiation shielding. Access shafts to the surface will probably be required about every kilometer to provide cooling tower and substation connections, and to allow maintenance crews to reach the beam line. A flat terrain is desirable to minimize the depth of such access shafts and would also facilitate the establishment of a global coordinate system for alignment on the surface and the subsequent transfer of the reference system to the beam line.

There are a number of ground composition issues that will influence the site location. The general experience in constructing long beam line tunnels such as LEP is that the ground should be compact, homogeneous, hard and dry. The hardness of the ground has a number of tradeoffs. Tunnels bored in hard rock, such as granite, will generally be more stable in terms of ground vibrations and long-term settling than those bored in softer rock. However, the tunneling costs may be prohibitive and the site would likely be located in a mountainous region. Areas with softer rock such as sandstone and limestone, which are likely to have flatter terrain, would make the tunneling easier, but the tunnel would have to be better reinforced, which may offset much of the cost savings. Also, ground water variations are likely to have a bigger effect on the alignment of a tunnel built in softer rock. In this regard, the tunnel movement over several years should be < 1 cm on kilometer-length scales. Much larger variations will require that a global realignment of the beam line be performed.

Seismic activity on all scales will be a factor in the site selection. While one certainly wants to avoid areas with a high-rate of major earthquakes, even areas with low seismic activity should be carefully considered since minor fault lines may act as "slip-joints" for any geo-mechanical forces. On a smaller amplitude scale, ground motion will impact the machine operation due to the pulse-to-pulse beam position jitter generated by the movements of the quadrupole magnets. The ground motion frequencies of concern are those above about 0.1 Hz where the feedback systems that will be used to stabilize the beam may not produce the suppression that is required. The large micro-seismic activity (≈ 0.14 Hz) that originates from ocean waves tends to be fairly directional so its effect on beam motion can be minimized by orienting the beam line perpendicular to the direction of these ground waves (*i.e.,* a correlated motion of all quadrupoles produces less net beam motion). At higher frequencies, where the correlation lengths generally become shorter, the beam motion becomes more sensitive to quadrupole vibrations although the amplitude of ground motion tends to decrease as well. The tolerances in this regard depend on several factors and are discussed in Section 7.4. In general, however, the preference is for a naturally "quiet" site that is not subject to large "cultural" noise such as that produced by heavy machinery.

So far we have considered the site requirements without a specific model of the tunnel layout. However, the tunnel layout will influence the site selection, and vice-versa. The minimal requirement for the cross-sectional tunnel layout is that there be two areas, one that houses the beam line, and one that houses the klystrons, modulators and control electronics, which we call the gallery. We want to be able to inhabit the gallery while the beam line is in operation which will require that the two areas be separated by at least an equivalent of 10 ft of concrete for shielding purposes. With these constraints, we have begun to examine more seriously the two layout configurations shown in Figures 7-11 and 7-12. The KEK-type, so named because the JLC group at KEK has proposed this design, houses both the gallery and beam line areas in one tunnel, but with a 10-ft-wide concrete wall separating them. The semicircular shape of this tunnel would require the use of specialized boring machines. The second design is modeled after the SLAC linac in which the gallery is separated from the beam line with the ground in between serving as shielding. In its

construction, the gallery would be located just below the surface and would follow the terrain where possible. It would be built using a "cut-and-cover" method whereas the beam line area would be constructed with circular tunnel boring machines. Having the gallery underground will aid in stabilizing the gallery air temperature to within the 1°C requirement. In the beam-line area, we want a 0.1°C stability, which should not be too difficult to achieve with either design since the beam line tunnels will be well isolated.

Careful evaluation of a number of tradeoffs will be required prior to selecting a tunnel design. The SLAC design will likely be cheaper to build and will allow easier access to the gallery where most of the maintenance work will be done. The beam line is also better isolated, thus reducing the vibrations there due to the maintenance work, pumps, and pulsed-power systems in the gallery. The impact of the shielding requirements on the design, including the complications caused by the numerous penetrations to the beam line, will also be less significant. However, the SLAC design requires longer rf runs with more bends between the pulse compression system and the structures, which will reduce the rf power transmission efficiency by a few percent. Also, the long penetrations through the ground between the two tunnels will have to be well-sealed to prevent water seepage into the beam line.

For costing purposes, we have developed in more detail the SLAC-type layout, including the utility distribution. This is presented in Chapter 18 which describes the conventional facilities.

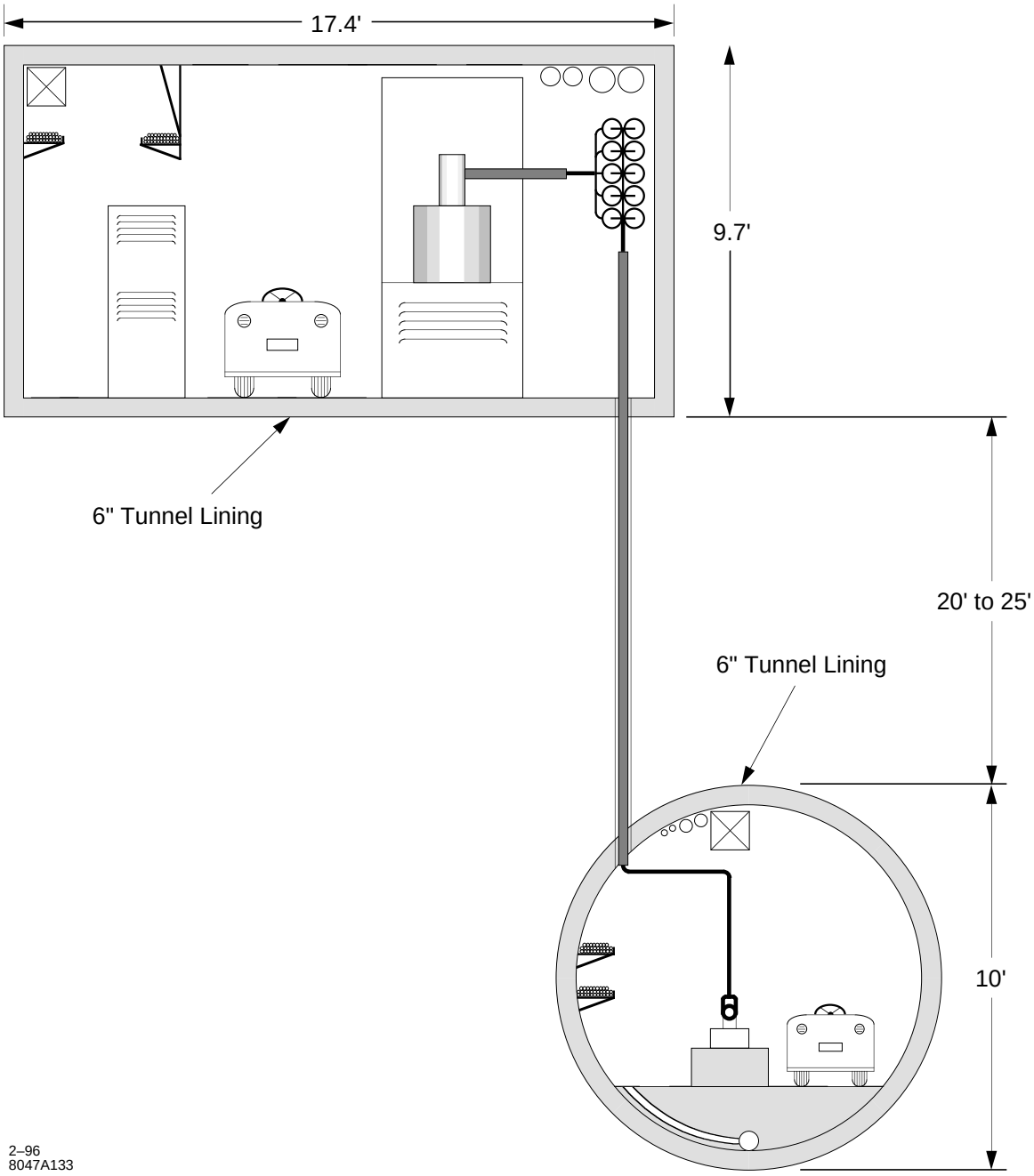

Figure 7-11. *Klystron gallery and beam line tunnel layout ("SLAC type").*

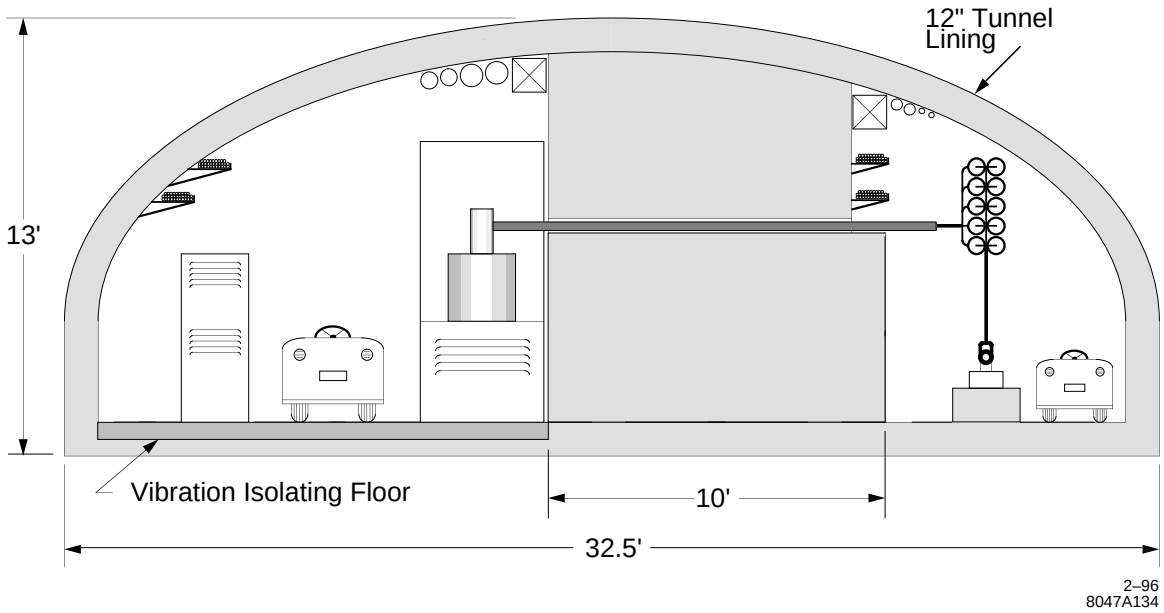

Figure 7-12. *Semi-elliptical highway-style tunnel layout ("KEK-type").*

7.4 Emittance Dynamics

The preservation of the transverse beam emittances and the control of the beam energy spread in the main linacs will require tight alignment and rf control tolerances. In this section, we is describe these tolerances with an emphasis on the underlying dynamical effects. We consider only the bare tolerances which are derived assuming no benefit from beam-based correction methods, including feedback. In the next section, we continue with discussions of stability, alignment, and feedback, where the emphasis is on the errors sources that set the scale of the problem, and the beam-based methods that will be required in cases where the bare tolerances cannot be met by other means.

We start this section by discussing the calculation of the short-range and long-range wakefields for the X-band accelerator structures. Although the intra-bunch dynamical effects of the wakefields in the NLC linacs are weak when compared with the SLC linac, they are still very important. Control of long-range wakefield effects is crucial to the operation of the NLC, due to its multibunch beam. Following the discussion of wakefield calculations, we discuss single bunch phase space issues (longitudinal and transverse), then multibunch phase space issues (longitudinal and transverse).

The discussion of single-bunch longitudinal phase space focuses on the need to adjust the average rf phase of the linac so the final energy spread is within the final-focus bandwidth. This average phase puts constraints on the energy spread profile in the linac which impacts wakefield and dispersive effects.

We next turn to single-bunch transverse effects where we present the bare tolerances for injection jitter, ground motion, power supply stability, quad, BPM and structure alignment, and rf deflections. In the case the quad and structure alignment, the results clearly indicate that conventional techniques will not be applicable as micron-level alignment will be required on lengths scales over 100 m.

For simplicity, the single bunch tolerances were computed assuming that the linac is autophased, that is, the energy spread of the bunches are adjusted so that the effect of the differential focusing along the longitudinal bunch profile exactly cancels the head-to-tail driving effect of the short-range transverse wakefields (using a correlated energy spread to offset resonate betatron growth is generally referred to as BNS damping). Because this requires energy spreads that are larger than the final-focus energy bandwidth, we will not be able to achieve this condition everywhere in the linac. Thus we consider how to optimize the rf phase profile along the linac to minimize betatron growth and yet keep the final bunch energy spread within the final-focus bandwidth.

Another option, that of using rf quadrupoles instead of (or in addition to) introducing a correlated energy spread to produce BNS damping, is also discussed. This would bring the linac closer to being autophased, but would require either a more complicated accelerating structure design or the introduction of special lossy rf quadrupole cells that would increase the length of the linacs.

The discussion of multibunch longitudinal phase space focuses upon the compensation of the multibunch beam loading, which varies from 20% to over 30% for the various linac parameters. The compensation scheme that has been chosen is "local" in that the rf input pulse is shaped to keep the energy of all the bunches in a train the same to within a few tenths of a percent throughout the linacs. The bunch-to-bunch charge variations and the ripple in the rf phase and amplitude must be well-controlled; simulation studies to set tolerances on these and other parameters are discussed in this subsection.

The discussion of multibunch transverse phase space includes the effects of the long-range transverse wakefield on emittance growth due to injection jitter and structure misalignments. The structure alignment tolerances are characterized by the length scale of the misalignments and are compared to the tolerances due to single-bunch effects. Finally, tolerances associated with the effect on ions on multibunch transport are presented.

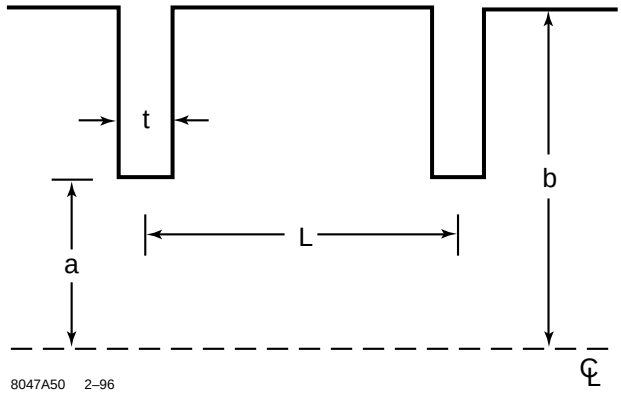

Figure 7-13. *The model of one cell of the NLC structure that is used in the calculations.*

7.4.1 Short-range Wakefields

Accelerator Structures

The accelerator structures in the main linacs will each consist of 206 cells and will operate at a frequency of 11.424 GHz. The structure design incorporates damping and detuning which is described in detail in Chapter 8. When computing the short-range wakefields generated in these structures, we ignore the manifolds that are used for damping but not the cell geometry variation that produces the detuning. Figure 7-13 illustrates the cell geometry (note the actual irises are rounded). Each cell is slightly different from its neighbors. The cell period is fixed at $L = 8.75$ mm and the cavity radius varies slightly but is roughly $b = 11$ mm. As one moves from the beginning to the end of the structure the iris radius varies from $a = 5.90$ mm to $a = 4.14$ mm and the iris thickness from $t = 1.26$ mm to $t = 2.46$ mm. The average value of a/λ for the cells is 0.187 where $\lambda = 26.25$ mm is the wavelength of the fundamental mode.

For our wakefield calculations we locally approximate the structure by a periodic model. The calculation method is as follows [Bane 1980a]: For the geometry of five representative cells, numbers 1, 51, 103, 154, and 206, we use the computer program KN7C [Keil 1972] to obtain the synchronous frequencies and loss factors of the first 250 or so monopole modes, which give us the low-frequency impedance. We approximate the high frequency contribution using the Sessler-Vainsteyn optical resonator model [Keil 1972, Brandt 1982]. Fourier-transforming these two contributions, we obtain the longitudinal wakefield for the given geometry. To calculate the wakefield of the entire NLC linac structure, we average the wakes obtained in this way for each of the five representative cells. The transverse (dipole) wakefield is obtained in an analogous manner, but using the computer program TRANSVRS [Bane 1980b] to obtain the dipole mode frequencies and loss factors. We first obtain the longitudinal dipole wakefield $W_z^{(1)}(s)$, then applying the Panofsky-Wenzel theorem [Panofsky 1956], we obtain the transverse dipole wakefield: $W_x(s) = \int_0^s W_z^{(1)}(s')\,ds'$.

The short-range longitudinal wakefield for cells 1, 51, 103, 154, and 206 of the NLC structure are shown in Figure 7-14 as a function of the distance behind the particle that is generating the wake. We should point out that the values at the origin, which should equal $W_z(0) = Z_0 c/(\pi a^2)$ [Palmer 1990, Gluckstern 1989] are about 5%–10% low, indicating some calculation error. The average wakefield for the entire structure is given by the dashed curve. A fit to the average wakefield, given by

$$W_z = 1388(V/pC/m) \cdot \exp\left[-1.16(s/mm)^{0.55}\right] \quad , \tag{7.4}$$

is shown by the dots. The net intra-bunch wakefield is obtained by convoluting this function with the longitudinal charge profile of the bunch. To set the length scale, the rms bunch length in the NLC will be in the 100- to 150-micron range.

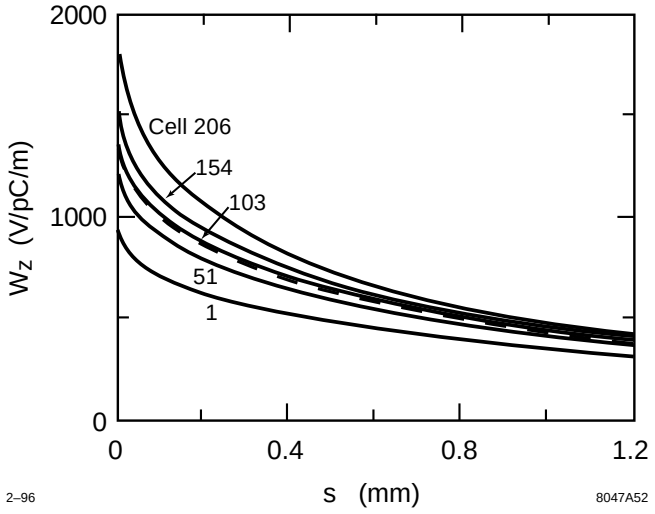

Figure 7-14. *The longitudinal wakefield of cells 1, 51, 103, 154, and 206 of the NLC structure. The average is the same as that of cell 103. The dashed curve represents the average wake, the dots, the empirical fit (see text).*

The short-range transverse wakefield for the representative cells are given in Figure 7-15. In this case, the slopes at the origin should equal $W_x'(0) = 2Z_0c/(\pi a^4)$; our results are slightly higher, but in no case by more than 4%. The average wakefield for the entire structure is indicated by the dashed curve in Figure 7-15. A fit to the average wakefield, given by

$$W_x = 88(V/pC/mm/m) \cdot \left(1 - \exp\left[-0.89(s/mm)^{0.87}\right]\right) \quad , \tag{7.5}$$

is indicated by the dots.

MPS Spoilers

There is one 8-mm-long MPS spoiler with an iris radius of 2 mm following every accelerator structure. Because the aperture is roughly a factor of two smaller than that of the accelerator structures, the transverse wakefield of these spoilers can be significant even though there is only one per structure. Figures 7-16 and 7-17 show the spoiler geometry and transverse wakefield kick on a 100-μm-long bunch; this kick is roughly 10% of the kick due to a single accelerator structure and thus has a small, but noticeable, effect on the dynamics. Finally, the relative magnitude of the longitudinal wakefield and the long-range wakefields are much smaller than those of the structures and can be neglected.

7.4.2 Long-Range Wakefields

In this section we discuss how the wakefield produced by a single bunch varies on the length scale of the bunch train. Given the transverse positions of the bunches in the train, these results can be used to compute the net wakefield acting on any bunch.

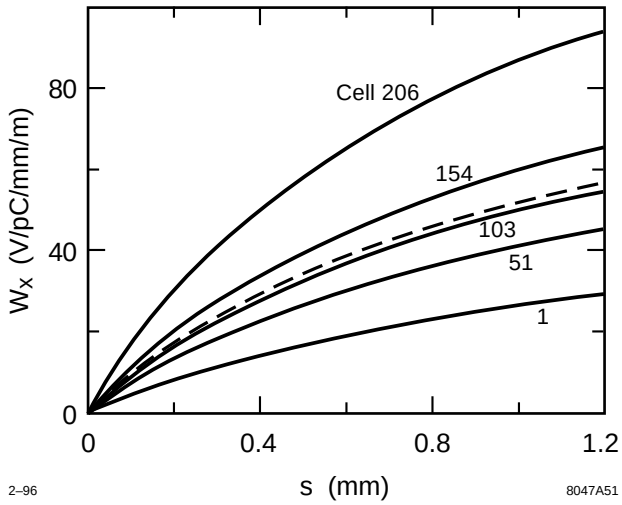

Figure 7-15. *The transverse (dipole) wakefield of cells 1, 51, 103, 154, and 206 of the NLC structure. The dashed curve gives the average wakefield; the dots, the empirical fit.*

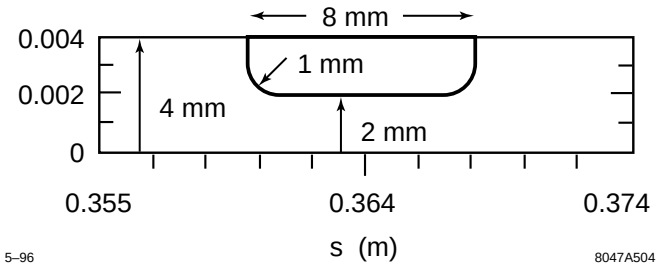

Figure 7-16. *Geometry of MPS spoiler located at the ends of the accelerator structures.*

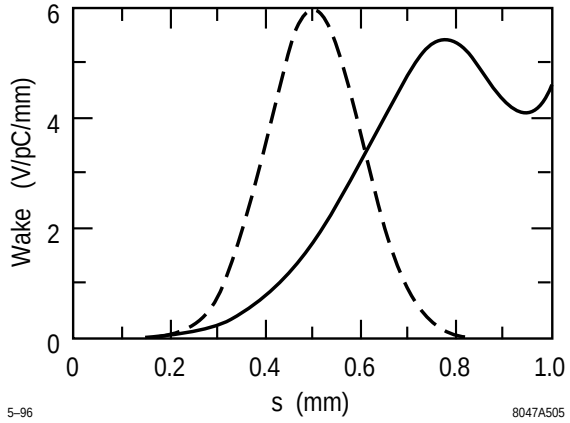

Figure 7-17. *Transverse wakefield (solid) due to a 100-μm-long bunch passing an MPS spoiler; this is roughly 10% of the transverse wakefield due to a single 1.8-m accelerator structure. Dashed curve is bunch profile with 100-μm σ_z.*

Detuned Structures

We first discuss the calculation of the long-range wakefield for a structure with detuning alone [Bane 1993]. The detuning involves varying the cell geometry to produce a Gaussian distribution in frequency of the product of the dipole mode density and the mode coupling strength to the beam. This yields an initial Gaussian fall-off of the integrated wakefield through the structure, which eventually levels off due to the discreteness of the modes. Further details of the detuning are given in Section 8.2. Here we outline the computational methods used to obtain the wakefield.

In this derivation, we consider each cell to be excited in some combination of cell modes (in practice, from the lowest or the lowest two dipole bands) and that the coupling holes determine the relation between the coefficients of these modes in two adjacent cells. Since the longitudinal electric field vanishes on the axis, we expect the coupling to be magnetic. We represent the structure by a single or double chain of circuits, where each circuit corresponds to a single-cell mode.

The uncoupled frequencies and the coupling parameters are obtained by applying the program TRANSVERS to periodic structures with the local cell dimensions at several points in the structure, and interpolating to obtain the values of these parameters at each cell. The coupled-circuit equations, supplemented by the appropriate boundary conditions in the first and last cells, are solved numerically by matrix inversion. The kick factors are then calculated from the resulting eigenfrequencies and eigenfunctions.

Most of the modes are localized in the structure in the lowest band. The results are shown in Figures 7-18 and 7-19 for the double-band model where only the two lowest bands are modeled. Note that the modes of the second band (roughly, those above 17 GHz) have low-kick factors and therefore do not contribute significantly to the wakefield. The wakefields obtained from the single- and double-band models do not differ greatly.

So far we have considered only the lowest two bands of dipole modes. When we perform a calculation that ignores cell-to-cell coupling but includes the effects of the modes of bands 3–8 [Bane 1994], we find that the wakefield amplitude is now an unacceptable 10% at the position of the second bunch, and it decreases only slowly as we move further back in the bunch train. This results from lack of detuning in some of the higher bands, especially the third and the sixth. Running URMEL [Weiland 1983], we find that near the light line, band 3 is a TM111-like mode and band 6 is a TM121-like mode. This suggests that by varying the iris thicknesses along the structure, with the thinner irises in cells with the larger radii—*i.e.*, near the beginning of the structure, and the thicker ones in cells with smaller radii—*i.e.*, near the end of the structure, we could detune these modes more. This variation has been incorporated in the our structure designs: a Gaussian distribution of iris thicknesses with an average of 1.5 mm, an rms of 0.25 mm, and a total variation of 1 mm is used. This is expected to reduce to 1% the contribution of Bands 3–8 to the wakefield at the subsequent bunch locations.

Damped Detuned Structure

Although the structure detuning significantly reduces the long-range wakefield, the amplification of the betatron motion of the bunches in an NLC built with these structures would be larger than can be tolerated. One solution would be to use different structure types with interleaved modes to improve the long-range decoherence of the wakefield. Another solution is to also damp the dipole modes, which has the added benefit of loosening the internal alignment tolerances for the structure. This approach is being actively pursued; the basic method is to channel the dipole mode energy to an external load through four manifolds that run along structure and couple to each of the cells (see Chapter 8 for details).

The equivalent circuit models used for the detuned structure may be extended to this damped detuned structure (DDS). Although the theoretical treatment of this problem is still being refined, the results so far are encouraging. The initial calculations were performed using a single-band model for the accelerating structure and coupling it to a transmission

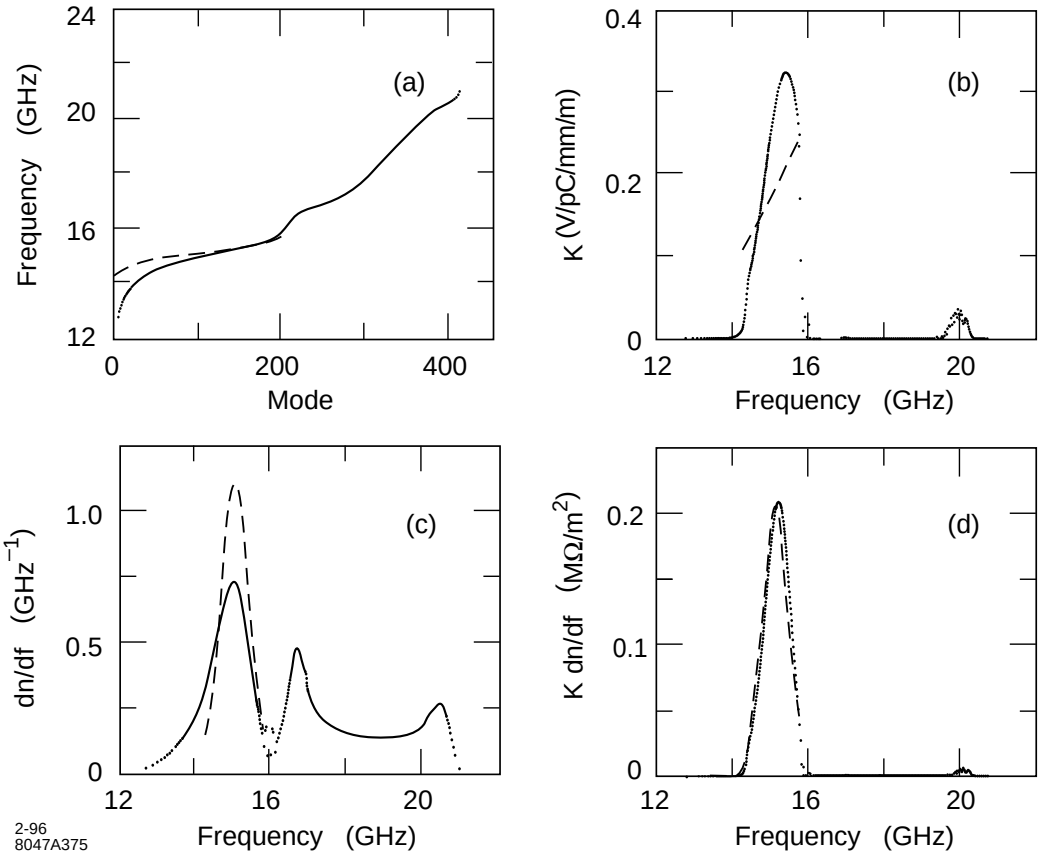

Figure 7-18. *Results of double-band coupled model: (a) the mode spectrum, (b) the kick factor, (c) the mode density (normalized so that the integral of dn/df over the first half of the modes is one), and (d) the product of kick factor and mode density. For comparison, dashed lines show the results from a model that does not include the effect of cell-to-cell coupling.*

line representation of each manifold mode that is included. The Qs of the modes from this treatment are shown in Figure 7-20 and the envelope of the resulting wake function is shown in Figure 7-21. The effect of copper losses have been included by combining the Q values shown in Figure 7-20 with an assumed copper loss value of 6500.

7.4.3 Single-Bunch Longitudinal Phase Space

The bunches will enter the NLC linacs with a 1% rms energy spread, which will be uncorrelated with longitudinal position along each bunch. In the linacs, the bunches will acquire a longitudinally-correlated component of energy spread due to the short-range wakefields and the curvature of the rf wave. Whereas the uncorrected component decreases inversely with energy, the correlated component will vary depending on how the phases of the accelerating rf field are set with respect to the beam timing.

There are three main constraints that one must consider when choosing the rf phase profile along the linacs. (1) The final energy spread of the beam must fit within the energy bandwidth of the final focus systems that are downstream of the linacs. (2) A correlated energy spread is needed in each bunch, with the bunch head at a higher energy than

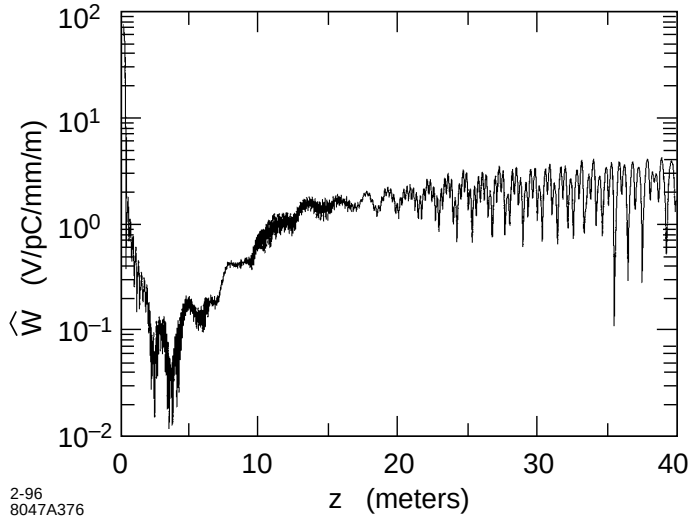

Figure 7-19. *The envelope of the wake function calculated using the double-band model.*

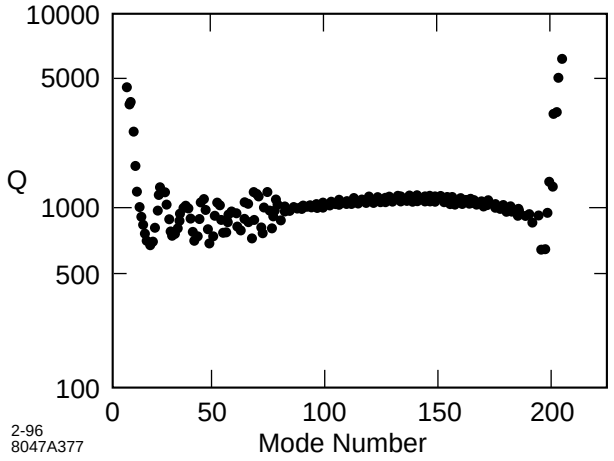

Figure 7-20. *The Qs of the modes in the lowest dipole passband, calculated for the damped detuned structure (DDS).*

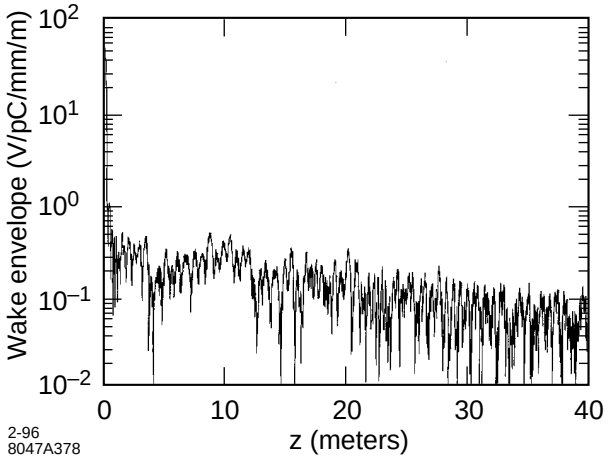

Figure 7-21. *The envelope of the wakefield function calculated for the damped detuned structure (DDS).*

the tail, to counteract the amplifying effect of the short-range wakefield on the betatron motion of the bunch. This approach to suppressing resonant growth is usually referred to as BNS damping; using an energy spread to exactly cancel the resonate driving term, so all parts of the bunch oscillate uniformly, is generally referred to as autophasing [Balakin 1983]. We want to run as close to the autophasing condition as possible. (3) rf power is precious so the phasing must be done efficiently to maintain a high accelerating gradient.

Satisfying these constraints will require some compromises. For example, in our linacs where the beta function scales roughly as the $\sqrt{E}$, the optimal energy spread for autophasing is nearly constant along the machine. This could be achieved by running the beams at a constant phase behind the rf crest but the resulting final energy spread would be larger than the final-focus bandwidth. Thus the beams will need to run more forward on the crest, on average, than is optimal for autophasing. The proposed solution is to run the beams somewhat behind the crest early in the linacs, and then sufficiently in front of the crest near the end to reach the desired final energy distribution, as is done in the SLC. This method requires some extra energy overhead so we must be efficient in selecting the phase profile.

The tradeoffs in this regard are discussed in Section 7.4.4 where we examine single-bunch transverse phase space effects in general. Another approach to this problem that uses rf quadrupoles is also described. Below we discuss the constraints on the average rf phase due to the final-focus bandwidth.

The Average Linac RF Phase

Let us consider the NLC-I parameters: initial energy $E_0 = 10\,\text{GeV}$, final energy $E_f = 250\,\text{GeV}$, and total structure length $L_{\text{acc}} = 8150\,\text{m}$. Let us assume that the bunches have a Gaussian longitudinal profile with rms length $\sigma_z = 125\,\mu\text{m}$, a population $N = 0.75 \times 10^{10}$ particles, and an initial uncorrelated energy spread of 1%. For this case, the single-bunch loading is 590 keV/ m. Also, the minimum rms energy spread is obtained when the average linac rf phase $\langle\phi\rangle = -18.0°$ (a negative phase represents a position in front of the rf crest); in this case the energy distribution is double-horned, with an rms spread of 0.27% and a horn spacing of 0.56%. Taking advantage of the larger energy bandwidth of the final focus systems, we choose to run the beams at $\langle\phi\rangle = -15.5°$, where the horn separation becomes 0.81%. In this way we introduce a slight, longitudinally correlated, energy variation, which will reduce the energy overhead needed for autophasing. Figure 7-22 shows the resulting energy distribution and energy correlation at the ends of the linacs.

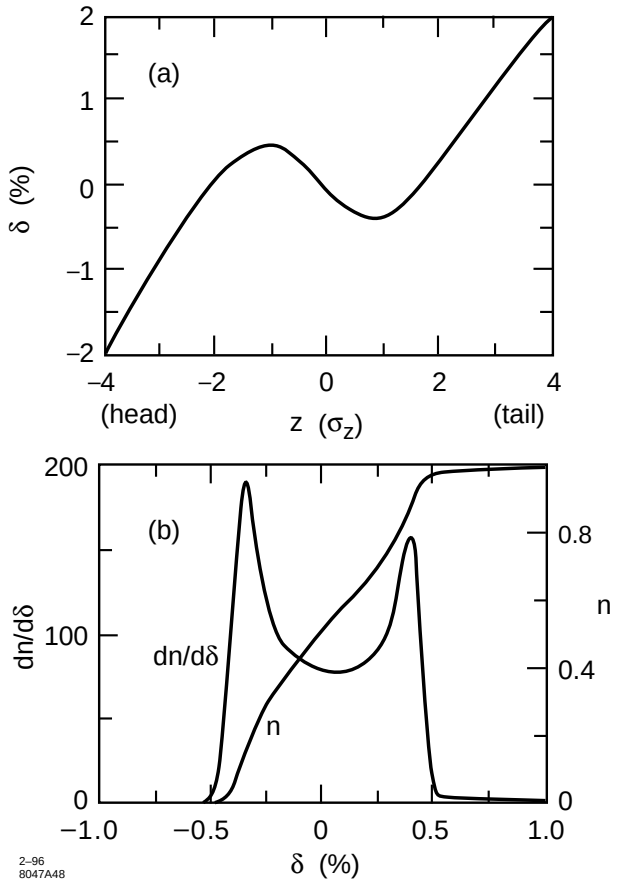

Figure 7-22. *For the NLC-I when $\langle\phi\rangle = -15.5°$: the correlated energy variation along the bunch (a), and the energy distribution and its integral (b).*

For NLC-II with $E_f = 500\,\text{GeV}$, $L_{\text{acc}} = 8150\,\text{m}$, $\sigma_z = 150\,\mu\text{m}$ and $N = 1.1 \times 10^{10}$, the single-bunch loading is 830 keV/m. In this case, we will run with $\langle\phi\rangle = -8.5°$ to achieve the energy distribution width of 0.8%.

7.4.4 Single-Bunch Transverse Phase Space

To transport the micron-size bunches through the main linacs without significantly degrading the bunch emittances will require that certain tolerances be met in regard to stability and alignment. In this section we discuss those tolerances that result from effects which degrade the transverse emittances of the all bunches equally, and ignore those effects which degrade the emittance of the bunch train as a whole (*e.g.*, kicks from long-range transverse wakefields). In doing so, we effectively treat the linacs as if only a single bunch were being transported per rf pulse. With this caveat, we examine jitter tolerances on injection and quadrupole motion; alignment requirements for the quadrupoles, BPMs, and accelerator structures; and limits on the transverse components of the rf field. In particular, we present only the bare requirements in that no beam-based alignment or feedback techniques are assumed to be used. In some cases, we

will see that the bare tolerances will be nearly impossible to meet, and so the use of these techniques will be essential. A description of these techniques and their effect on the tolerances are presented in Section 7.5.

To compute the tolerances, a number of simplifying assumptions were made. An important one is that the linacs are operated in the autophased condition so that the effect of short-range transverse wakefields on betatron motion can be ignored. For the linac lattice, it was assumed that the beta function and the spacing between quadrupoles scale as $\sqrt{E}$, and that the horizontal and vertical phase advance is 90° per cell. For the NLC Ib (NLC IIb) configuration, an initial quadrupole spacing of 4.2 m (3.2 m) was assumed which yields a beta function profile and quadrupole magnet count that are similar to that of the proposed optics (Section 7.3.2). Only the NLC IIb results for the vertical plane are presented here: the vertical tolerances for the NLC Ib configuration are generally about 35% looser, and the tolerances for the horizontal plane in either configuration are about a factor of three looser. The emittance growth values that are quoted are averages and are relative to $\gamma\epsilon_y = 4 \times 10^{-8}$. In most cases, the emittance growth is distributed as χ^2 with two degrees of freedom, which is exponential.

We next turn to a more detailed consideration of how one implements the desired BNS damping, *i.e.,* how one obtains as nearly as possible the autophased condition while staying within acceptable bounds of energy overhead and final energy spread. Also we examine the use of rf quadrupoles as a possible alternative to achieving autophasing.

Injection Jitter

Pulse-to-pulse variations of the bunch trajectories at injection to the linacs will degrade the machine performance in two ways. In traversing the linacs, the energy spread of the off-axis bunches will lead to filamentation, and thus increase the bunch emittances. Even in the absence of this effect, the bunches will collide off-center at the IP, thus reducing the collision luminosity. The effect of this jitter can be characterized by an equivalent increase in the bunch emittance, but requires an assumption about the transverse phase space of the jitter. If we assume that the jitter phase space is matched to the beam, as is generally seen in the SLC, then the emittance growth is equal to the square of the ratio of rms jitter to beam size. Hence, to keep the emittance growth below 3%, one must limit the jitter to less than 17% of the beam size.

Including the effect of filamentation does not change this result since the jitter phase space is matched to the beam. However, its effect would be a limiting factor if one could remove the jitter in a feed-forward manner between the end of the linacs and the IP. If the filamentation in the linac was complete, the jitter tolerance would not change, but we expect only partial filamentation, about 50° rms assuming a 0.1% uncorrelated energy spread that is independent of energy, plus a 1% uncorrelated energy spread component at the beginning of the linacs that decreases as 1/E (note the BNS energy spread can be ignored for this calculation if the beams are autophased). With this partial filamentation, the injection jitter tolerance would increase to about 26% of the beam size, which would hardly justify an effort at a feed-forward correction.

Quadrupole Vibration and Ground Motion

Another source of bunch trajectory jitter is from quadrupole magnet vibrations. If the transverse position of a quadrupole is displaced, it will kick the beam by an angle equal to the offset divided by the focal length of the quadrupole. If all quadrupole positions vary pulse-to-pulse, then the bunch trajectories at the end of the linacs will vary as the sum of the betatron trajectories produced by the individual kicks during each pulse. The size of this jitter depends on the spectrum of the individual quadrupole motions as well as the correlations of the quadrupole motions. As a simplification, we assume isotropy in that we suppose that all quadrupole motion spectra are equal and that the correlations depend only on the distance between quadrupoles.

A major concern in the NLC design is the effect that ground motion will have on beam transport via the quadrupole vibration it generates. When computing ground motion tolerances in this regard, one can treat each region of the NLC, such as the electron linac, independently from the rest of the machine to a good approximation. The quantity of interest is the deviation of the beam motion from the ground motion at the end of the region when the initial beam trajectory follows the ground motion at the beginning of the region. When computing the effect on luminosity, the deviation at the end of the region is assumed to remain unchanged relative to the beam size as the beam travels to the IP, where by symmetry, it can be shown to be related to that of the opposing beam. Thus the effect of ground motion on luminosity can be computed for both halves of the machine from the relative beam motion it induces in one half.

If the ground motion is uncorrelated quad-to-quad, then the tolerance one finds on the vertical rms motion is 6 nm for a 1.5% reduction in the time-averaged luminosity ($\gamma\epsilon_y = 4\times10^{-8}$ is assumed at the IP). In the NLC linac tunnels, the rms vertical ground motion, when computed over periods of several seconds, will likely be larger than this tolerance. However at low frequencies, where the ground motion is largest, the motion is generally correlated over long distances which loosens the tolerance.

While much data exists on ground motion spectra, little is available on long-range correlations. To see how typical these measurements are, and to better understand the dynamics of ground motion, we did a series of seismic measurements in the SLAC linac tunnel. These are described in Appendix C together with the formalism needed to analyze the data and to compute the effect of ground motion on beam transport.

From this study, it was found that the vertical ground motion can be reasonably well described by a model in which the motion is due to horizontally-traveling waves that are isotropically distributed in direction. For two points separated by distance Δz, the model predicts that the correlation in the vertical motion equals $J_0\left(2\pi f\Delta z/v\right)$ where J_0 is the zero-order Bessel function, f is the frequency of the waves, and v is the wave phase velocity, which we find depends on f:

$$v(\mathrm{km/s}) = 0.45 + 1.9\exp(-f(\,\mathrm{Hz})/2.0) \quad . \tag{7.6}$$

Using this correlation function, the tolerance on the rms vertical ground motion for a 1.5% reduction in the time-averaged luminosity was computed as a function of frequency. As a worst case, the tolerance was computed assuming that in addition to wave-like motion, there is an uncorrelated component of the motion that is equal to the seismometer electronic noise contribution to our measurements (see C.4 for details). The results for these two cases are shown in Figure 7-23. One sees that for frequencies above 4 Hz, the tolerance is roughly equal to the 6-nm value for uncorrelated ground motion. Below 4 Hz, the tolerance rises rapidly due to the fact that the wavelengths of the ground motion, v/f, are longer than the betatron wavelengths, so that the sum of the quadrupole kicks average out. In fact, it is the 180-m betatron wavelength at the end of the linac that determines this transition point. With the inclusion of uncorrelated motion, the tolerances at low frequency reflect the fraction of the measured power that is due to seismometer noise (*e.g.,* 1% noise power yields a $6/\sqrt{.01}$ = 60 nm tolerance).

In Section 7.5.1, we compare these tolerances to measured ground motion spectra, and discuss ways to actively suppress the effects of quadrupole vibrations. We should note, however, that ground motion will not be the only source of quadrupole vibration. Vibrations caused by the water flow through the cooling circuits for the quadrupoles will have to be controlled, as will the motions of the structures if they couple through the supports and vacuum pipe to the quadrupoles (the structures themselves have a much looser vibration tolerance than the quadrupoles). Also, care will have to be taken in designing the support systems to avoid mechanical resonances.

Finally, we consider the beam trajectory jitter that results from random fluctuations in the quadrupole power supply currents. Since the beam will not travel exactly on-axis through the quadrupoles, pulse-to-pulse changes in the quadrupole magnetic fields will produce an effect similar to uncorrelated ground motion. We expect that the beam will be centered in the quadrupoles to better than 100-μm rms (10 μm if no non-local steering is used), so the quadrupole

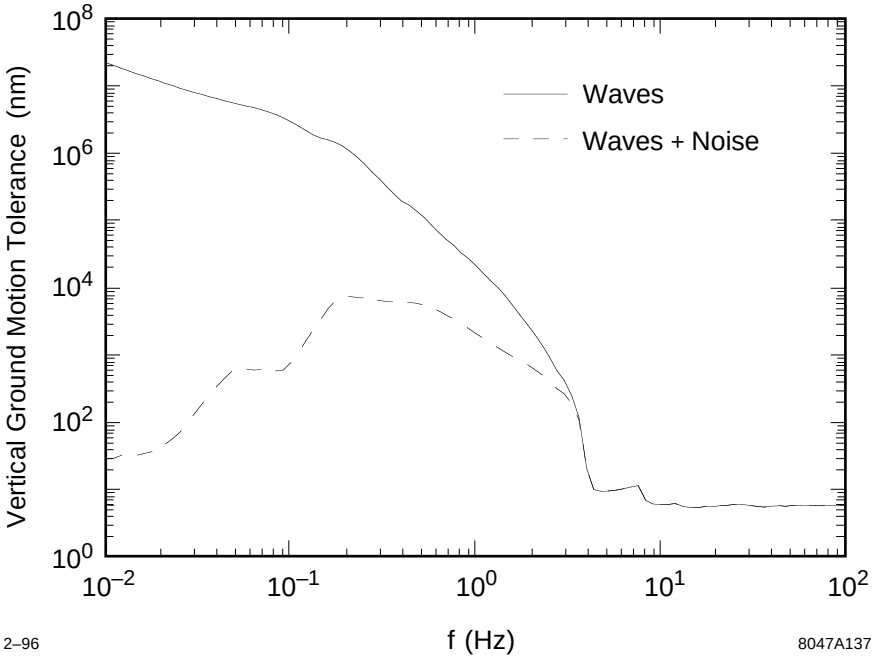

Figure 7-23. *Linac rms vertical ground motion tolerance for a 1.5% luminosity reduction as a function of frequency for pure wave-like motion (solid) and for wave-like plus uncorrelated motion equal to the seismometer electronic noise (dashed).*

power supplies must be regulated to 6×10^{-5}, assuming they are independent, to limit the luminosity reduction to less than 1.5%.

Quadrupole and BPM Offsets

If the quadrupoles are perfectly aligned along the linac axis and a bunch is injected on-axis, no dispersive emittance growth will occur. However, if the quadrupoles are offset from this axis, and the bunch is steered to the centers of the quadrupoles, then the differential kicks that the bunch receives due to its energy spread will generate emittance growth. This growth will be worse if the BPMs themselves are not centered within the quadrupoles since they will be used to steer the beam. The BPM offsets, which we define as the difference between the BPM centers (mechanical and electronic) and the quadrupole magnetic centers, will add in quadrature to the quadrupole offsets in their effect on dispersion if they are random. In this case, the tolerance on the sum is 3 μm for a 25% emittance growth in the vertical plane assuming an effective bunch energy spread of 0.6%.

Since the quadrupole alignment accuracy will depend on the distance scale over which the alignment is done, a better way to characterize the tolerance is in terms of the wavelength of the misalignments. For this purpose, we assume that the quadrupole offsets are sinusoidal with wavelength λ, and that bunches are steered to zero in the BPMs, which themselves are centered in the quadrupoles. Figure 7-24 shows the tolerance on the offset amplitude for a 25% vertical emittance growth as a function of λ assuming that the beam is injected on-axis. One sees that for $\lambda < 180\,\mathrm{m}$, the tolerances are nearly all less than 10 μm, and at larger λ, they rise rapidly. This rise occurs because λ becomes larger than the longest betatron wavelength in the linac, so the dispersion averages out (*i.e.*, for the same reason that the ground motion tolerances rise below 4 Hz in Figure 7-23). Using conventional survey methods, one would have a

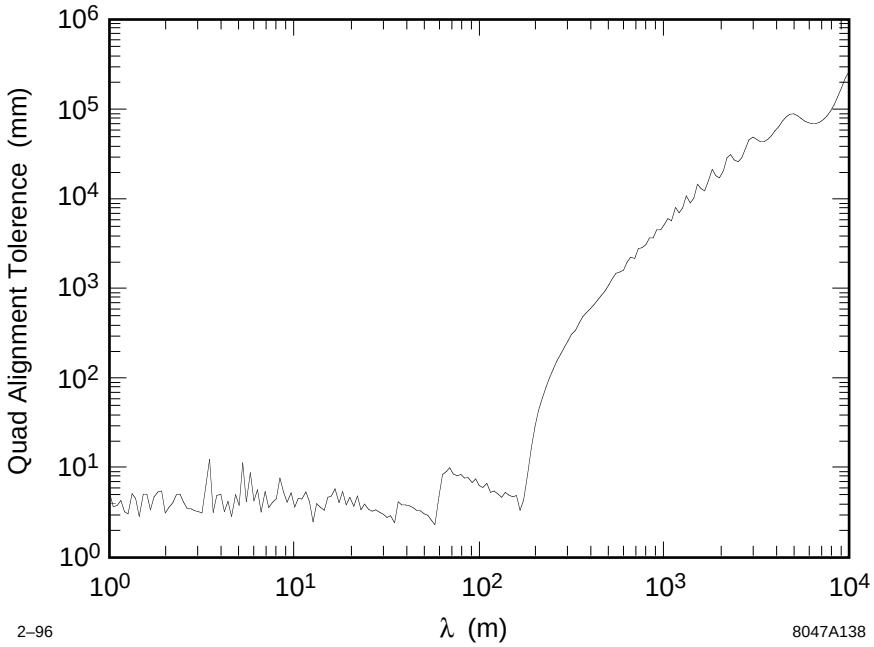

Figure 7-24. *Quad alignment tolerance for a 25% vertical emittance growth as a function of the wavelength* (λ) *of the misalignment. A 0.6% bunch energy spread is assumed.*

difficult time achieving a 3-μm alignment on a 1-m scale, let alone on a 180-m scale. The use of beam-based alignment will alleviate the need for such tight tolerances; this is discussed in Section 7.5.2.

Structure Offsets

If a bunch travels off-axis through a structure, the transverse wakefield that is generated will produce a differential kick along the longitudinal profile of the bunch. Like the differential kicks due to the bunch energy spread, the wakefield kicks will generate an emittance growth. To a good approximation, the effect of the wakefield kicks can be treated to first order where one ignores the position variation along the bunch when computing the generated wakefields. In this approximation, the emittance growth depends on the rms variation of the wakefield kick along the longitudinal profile of the bunch, just as dispersive growth depends on energy spread. The rms wakefield kick used to obtain the results presented here is 6.2 V/pC/ m/ mm, which assumes a 150-μm bunch length.

To compute the structure alignment tolerances, we assume that the quadrupoles and BPMs are perfectly aligned, and that the net wakefield kick to the bunch is removed locally by steering the bunch centroid to zero in the BPMs. In this case, a 6-μm rms random misalignment of the structures parallel to the beam axis yields a 25% vertical emittance growth. Like the dispersion analysis, we also computed the tolerance for sinusoidal misalignments of the structures, where both intra-structure and inter-structure alignment varies. Figure 7-25 shows the results for a 25% vertical emittance growth as a function of the wavelength of the misalignment. One sees that the most sensitive wavelength is about 180 m. This wavelength is resonant with the betatron motion near the end of the linacs where the weaker focusing leads to a larger growth. Like the quadrupole alignment tolerances, achieving these values would be extremely difficult with conventional alignment techniques. Instead, we will rely on beam induced signals from the structures to keep them centered about the beam trajectory. This method is described in Section 7.5.2. Note that we revisit structure tolerances in Section 7.4.6, where we consider multibunch effects as well.

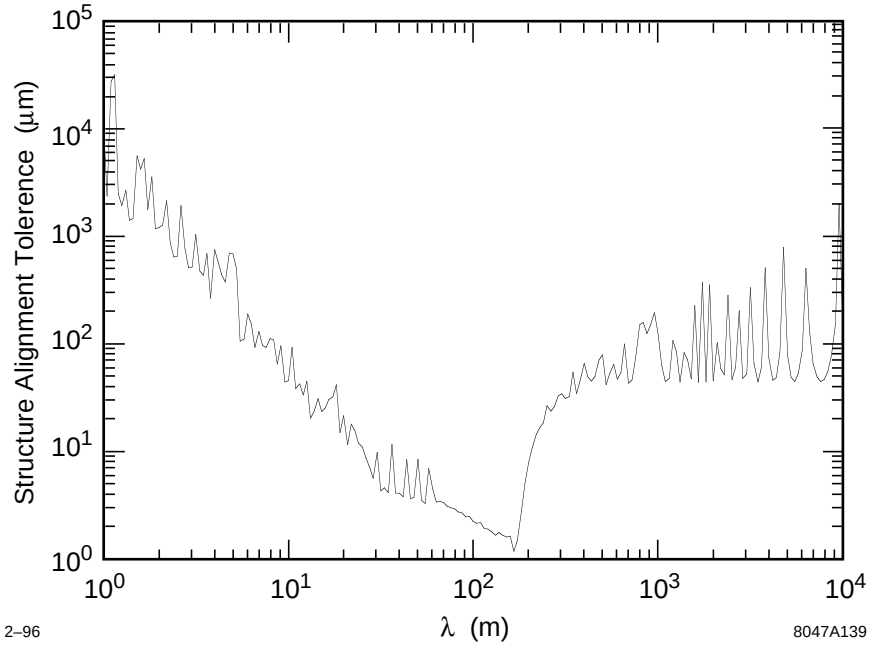

Figure 7-25. *Structure alignment tolerance for a 25% vertical emittance growth as a function of the wavelength* (λ) *of the misalignment.*

RF Deflections

Internal misalignments of the structures (*e.g.*, bookshelving) and dark currents within the structures can generate transverse rf fields that will deflect the beam. These fields, which can be static or vary pulse-to-pulse, will produce both a net and differential kick to the bunches. Using the wakefield tolerance result for uncorrelated structure offsets, one can readily compute the tolerance on the allowed integrated transverse rf field per structure assuming that the rf kicks are also uncorrelated structure-to-structure, as is likely to be the case.

To prevent an emittance growth of more than 3% as the result of the differential kicks produced along the longitudinal profile of a bunch, the tolerance on the integrated rf field amplitude is $1.2\,\text{keV}/\sin(\psi)$ where ψ is the phase offset of the bunch from the crest of the rf field. This tolerance holds whether the kicks are static, or vary pulse-to-pulse in amplitude but with a constant phase relative to the beam. Fields that are 90° out of phase with respect to the beam produce the largest slope and hence the tightest tolerance; for the transverse rf field effect on the net motion of the beam, the opposite is true. Here the tolerance is $0.04\,\text{keV}/\cos(\psi)$ for a 3% emittance growth if the transverse field jitters pulse-to-pulse, and $80\,\text{keV}/\cos(\psi)$ if the field is static but there is 10^{-3} pulse-to-pulse energy gain jitter in the groups of four structures that are powered in common.

For either emittance growth mechanism, it will be especially important that the tolerances be met if the rf transverse fields vary independently pulse-to-pulse since there will be no means to offset their effect. Currently we do not have much information on the size and temporal nature of the transverse rf fields in the X-band structures that have been built. (This is also true for the transverse field jitter in the SLC S-band structures, although there is a hint that it could be as high as 1-keV rms per 12-m section based on the observed white-noise-like beam jitter growth in the SLC linac.) From observing the power in the dipole modes that are excited in the DDS X-band structures without beam, we should be able to put limits on the transverse kicks. Also, from operating the NLCTA, we should learn enough to know whether the tolerances for most cases would be met in an NLC built with the same rf system.

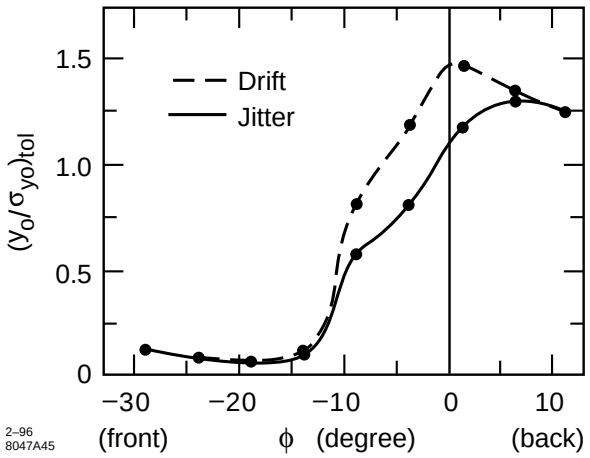

Figure 7-26. *Tolerance to oscillations at injection, i.e., the ratio (y_0/σ_{y0}) that gives 25% emittance growth at the end of the linac, when all klystrons are set to phase ϕ. For the jitter tolerance (solid curve) the emittance is calculated with respect to the beam line axis; for the drift tolerance, with respect to the bunch centroid.*

The RF Phase Profile Along the Linac

To suppress betatron amplification due to short-range wakefields, we plan to vary the klystron rf phase profile along the linacs to best achieve autophasing while keeping the average phase such that the final-bunch energy width is 0.8%, as was discussed previously. To decide which particular rf phase profile to use, we studied the sensitivity of the final beam emittance to betatron oscillations in an error-free linac. As figures of merit, we define t_0 as the injection jitter tolerance, and t as the injection drift tolerance. Specifically, t_0 is the ratio of the initial vertical bunch jitter, y_0, to the initial vertical bunch size, σ_{y0}, that results in a time-averaged emittance growth of 25% with respect to the beam line axis; t is defined similarly except that the emittance growth is with respect to the bunch centroid. Note that for the case of no wakefields and no energy spread, $t_0 = 0.75$ and $t = \infty$, and that for $t_0 > 0.75$, there is actual damping of the initial oscillation. The values of $t_0 = 0.75$ and $t = \infty$ are also the case for exact autophasing in the absence of an uncorrelated energy spread.

The oscillation studies were done using the parameters of the NLC-I, but with an active linac length of 7500 m, for which an energy width of 0.8% is obtained when $\langle\phi\rangle = -14.0°$. The lattice used was a piece-wise FODO array with 90° phase advance per cell. Between the quadrupoles there are an integer number of 1.8-m-long accelerating structures, beginning with two structures between the first two quadrupoles. Overall, β scales roughly as $\sqrt{E}$. Initially, $\langle\beta_0\rangle = 8$ m.

First, let us consider the simple case where all rf phases are equal. Figure 7-26 shows the tolerances as a function of this phase, ϕ. We see that at $\phi = -14.0°$, both the injection jitter and drift tolerances are 0.1. To be near the autophasing condition ($t_0 \approx 0.75$) throughout the linacs, the klystron phases need to be shifted by about $+10°$. Unfortunately, we cannot run this way since the final beam energy spread would be unacceptably large.

To constrain the final energy spread and still allow freedom to adjust the phase profile, we propose a method similar to that used in the SLC. We divide the klystrons into two families, with the first family containing the first n_a klystron units that are set to phase ϕ_a, and the second containing the rest of the units that are set to phase ϕ_b. In all cases the average phase is kept fixed at $\langle\phi\rangle = -14.0°$. For the purposes of this calculation, the i^{th} klystron unit denotes all klystrons that feed into the i^{th} group of four lattice cells; in total there are 88 such units. Injection jitter tolerance curves were calculated for fixed amounts of energy overhead, ΔE_{BNS}, for the phase shifting; here $\Delta E_{BNS} = 2$, 4,

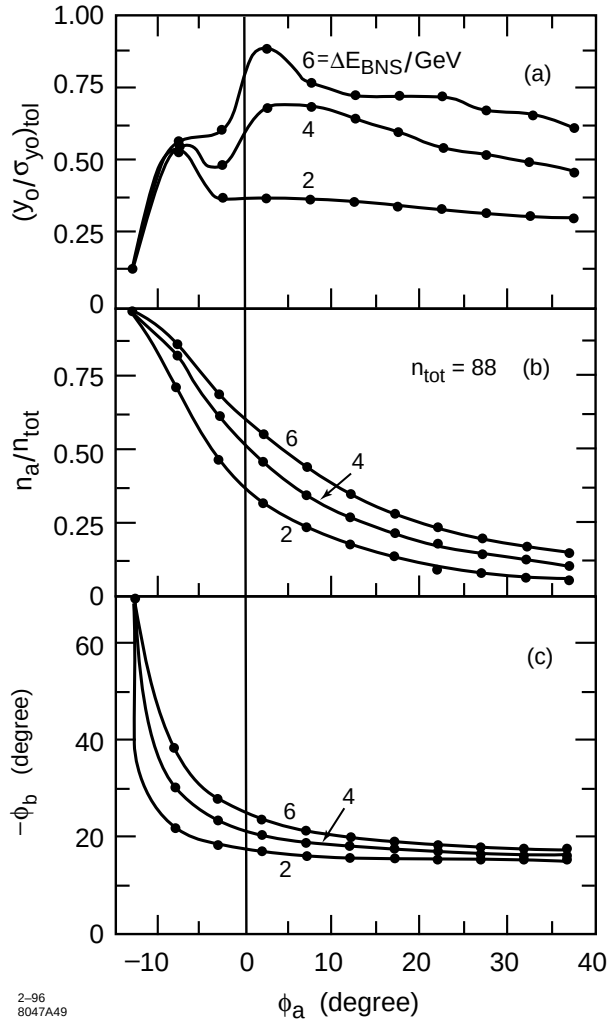

Figure 7-27. *Injection jitter tolerance for 25% emittance growth for klystron configurations employing two families of phases, plotted as (a) function of the phase of the first family ϕ_a for $\Delta E_{bns} = 2$, 4, 6 GeV. In all cases the final energy distribution has a width of 0.8%. Also plotted are (b) the relative number of units in family a, and (c) the phase of the second family ϕ_b .*

6 GeV. Plotted in Figure 7-27 are the injection jitter tolerance, the relative number of a-type klystron units n_a/n_{tot}, and ϕ_b, all as a function of ϕ_a. We see that if we are willing to give up 6 GeV, which is a 2.5% energy overhead, we can reach an injection jitter tolerance of $t_0 = 0.9$ with $\phi_a = 2°$, $n_a/n_{tot} = 0.55$, and $\phi_b = -23.7°$.

Next we studied the effect of jitter that begins at various locations along the linacs, not just at injection. In Figure 7-28 we plot the tolerances as functions of starting location of the jitter for the cases of no BNS damping, and with BNS damping, with $\Delta E_{BNS} = 6$ GeV and $\phi_a = 2°$. Note that BNS damping helps primarily in the first half of the linac, which is precisely where we need it most.

In the tolerance studies described above, we were mainly concerned with the behavior of the core of the beam, which is the part that contributes most to luminosity. In the simulations that were done for these studies, the longitudinal distribution was truncated at $-2.5\sigma_z$ (in front of beam center) and $2.0\sigma_z$ (in back of it), so that a few particles far out in

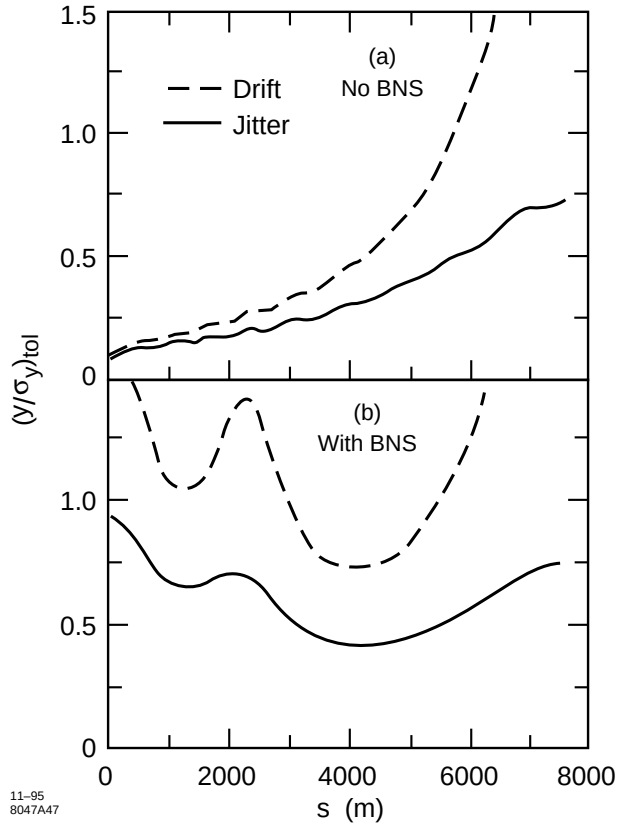

Figure 7-28. *Tolerance to oscillations beginning in the linac as function of the starting location of the oscillation, for the case of (a) no BNS damping, and (b) with BNS damping, with $\Delta E_{BNS} = 6$ GeV and $\phi_a = 2°$. Plotted is the ratio of the initial jitter to beam size at that location that yields a final emittance growth of 25%. For the jitter tolerance (solid curve), the emittance is calculated with respect to the beam linac axis; for the drift tolerance (dashed curve), the emittance is calculated with respect to the beam centroid.*

the tail of the distribution would not significantly affect the results. However, because of their potential for generating backgrounds, we would also like to know the behavior of particles in the tails. To show how a betatron oscillation affects such particles we have repeated the calculation for our BNS example, but now tracking longitudinal slices that cover $\pm 4\sigma_z$ of the bunch. In Figure 7-29, we show the phase space of a bunch that was injected with an initial vertical offset of σ_{y0}. Note that the largest amplitude slices are in the tail of the beam, at $z > 2.5\sigma_z$, followed by slices at the head, at $z < -2.5\sigma_z$. Therefore, it is desirable to truncate the longitudinal distribution of the bunches at $|z| \lesssim 2.5\sigma_z$.

The Option of Using RF Quadrupoles

In the CLIC project, rf quadrupoles have been proposed as a means to suppress wakefield-induced betatron growth as an alternate to the BNS method of using a correlated energy spread [Schnell 1987, Schnell 1991]. A small fraction of the accelerating structure cells (∼10%) are built in a noncylindrically symmetric shape, resulting in a fundamental mode that focuses as well as accelerates. With this system, in principle, BNS-like damping can be effective throughout

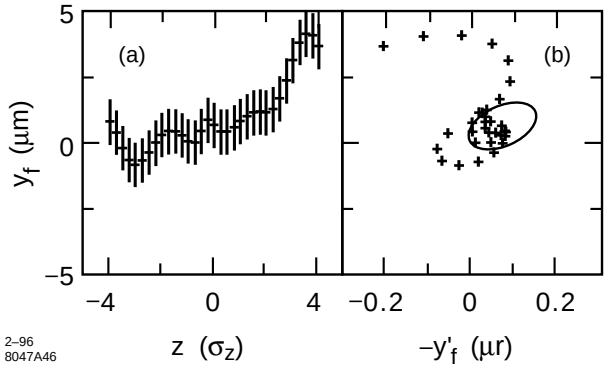

Figure 7-29. *Vertical phase space of a bunch that was injected off axis by σ_{y0} in a linac with $\Delta E_{BNS} = 6$ GeV and $\phi_a = 2^\circ$. Shown are (a) the final centroid positions y_f (the error bars indicate $\pm\sigma_{yf}$) vs. longitudinal position within the bunch z, and (b) the final centroid positions vs. final centroid angles (the curve is the 1σ ellipse of the beam slice at $z = 0$).*

the linacs, with no additional cost in energy overhead. For cavities coupled by narrow slits, the focusing gradient (in T/m) is given by [Schnell 1987]:

$$G = \frac{k_{rf} E_z}{2c} \sin(k_{rf} z + \phi) \quad , \tag{7.7}$$

where k_{rf} is the rf wave number, E_z is the accelerating gradient, and ϕ is the rf phase. Near $\phi = 0$ there is a nearly linear variation of gradient along the bunch. Although the model used to compute G is very simplistic, it has been reported that in realistic accelerator structures, where either the normal irises have been flattened, or where the cavity is elliptical with the ratio of the major to minor axis being about 2, the gradient can be 85% of that given by Equation 7.7 (though, in the latter case, with 25% reduction in fundamental mode R/Q) [Schnell 1991].

From Figure 7-26 we see that we would like an rf quadrupole focusing strength that is equivalent to about a $\Delta\phi = 10^\circ$ shift of average phase, or a focusing strength change at $z = \sigma_z$ of $k_{rf}\sigma_z \tan\Delta\phi \approx 0.5\%$. Assuming that the rf quadrupoles are 80% as effective as Equation 7.7, and using our machine parameters, we find that 4.5% of the structures need to be rf quadrupoles. Considering that we have a piecewise constant lattice, this number increases to 6.3%. Finally, assuming that only two versions of our accelerating structures will be built—one with an x-focusing rf quadrupole and one with an x-defocusing rf quadrupole —and that there will be on average many accelerating structures between neighboring quadrupoles, the fraction of each structure that would be used for rf focusing becomes 10%. This would require a major redesign of our accelerating structures.

Another approach is to build small, lossy rf quadrupole cells, one for each quadrupole (∼350 in total), that are powered to an effective gradient of 100 MV/m. In this case, the total length of the rf quadrupole cells relative to the total accelerator structure length is 1.5%.

7.4.5 Multibunch Longitudinal Phase Space

This section discusses multibunch longitudinal dynamics, and the method of multibunch energy compensation planned for the NLC.

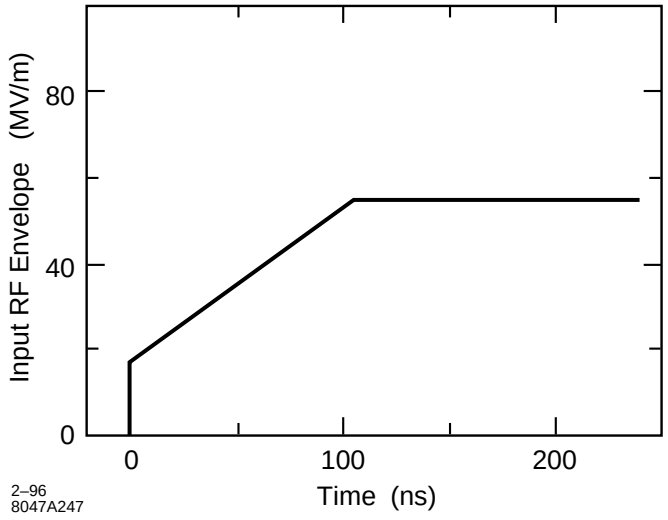

Figure 7-30. *Envelope of input rf pulse, used in long-pulse pre-filling compensation scheme.*

Without some method of compensation, there would be a drop in energy of about 25% from the head of a train to the tail due to beam loading in the accelerating mode. There is also potentially some bunch-to-bunch variation in energy due to HOMs—this must be controlled by detuning and/or damping those modes.

The tolerance on the multibunch energy spread and on the variation in the average energy of the beams have both been taken to be as little as $\Delta E/E \sim 10^{-3}$ in some of the simulations discussed or presented in this section. This may seem somewhat conservative since the energy bandwidth of the final focus is $.8\%$. However, it needs to be kept small due to the residual dispersion in the linac.

The method of beam-loading compensation is to pre-fill the rf structure with a pulse shaped to simulate the steady-state beam-loaded rf profile in the structure. This profile is then automatically maintained if the incoming rf field amplitude is kept constant during the passage of the train. A simple linear ramp yields good compensation, but the rf pulse could be further corrected to increase the compensation (and maintain it via feedback as conditions vary).

The input rf pulse used in our example is shown in Figure 7-30. However, since dispersion creates large amplitude variations on the front of the rf pulse, it is desirable to wait an additional 10 ns before injecting the bunch train, to allow the worst of these dispersion "wiggles" to propagate out of the structure.

We model the linac structures as having a constant unloaded gradient, with $2\pi/3$ phase advance per cell. Parameters are shown in Table 7-7. In this subsection, the parameters of the ramp are chosen to give a loaded average energy gradient of 50 MV/m. Charge per bunch is 1×10^{10} and the bunch spacing is 16 rf buckets ($\sim$1.4 ns).

A detailed simulation program has been written [Thompson 1993] in which one may take into account input rf pulse shaping and timing, the dispersion of the rf pulse as it transits the structure, the longitudinal distribution of charge within the bunches, the long-range wake including both the fundamental (accelerating) mode and higher order modes, the short-range wake, and phasing of the bunches with respect to the crests of the rf.

Figure 7-31(a) shows the average energy gained by each bunch in a single 1.8-m accelerating section. Figure 7-31(b) shows the fractional deviation of the energy centroid of each bunch from the average energy of the bunches. Here we have included the effect of dispersion of different frequencies in the rf pulse as it travels through the structure; this is

rf frequency, f_{rf}	11.424 GHz
Section length	1.8 m
Attenuation τ	0.505
Fundamental mode Q	7107
Fundamental mode loss factor, κ_1	203.75 V/pC
Filling time, T_f	100 ns
Bunch spacing	$16\lambda_{rf} \approx$42 cm
Bunch charge	1×10^{10}

Table 7-7. *Parameters used in energy compensation simulations.*

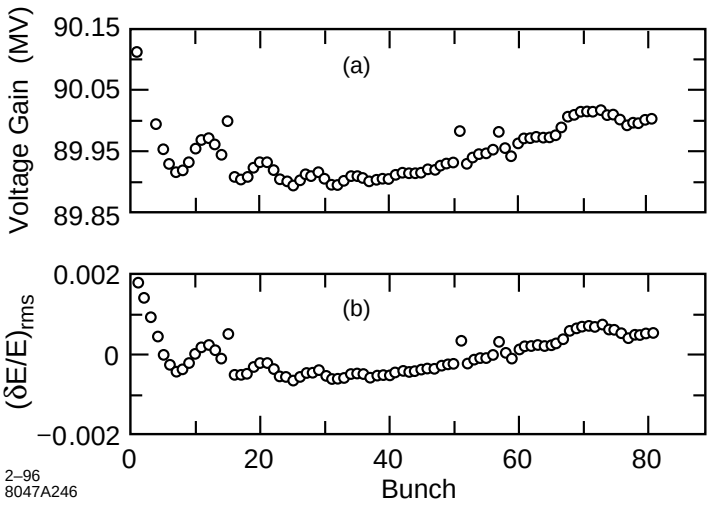

Figure 7-31. *(a) Average energy gained by each bunch in a single 1.8-m accelerating section. (b) Fractional deviation of the energy centroid of each bunch from the average energy of the bunches.*

the cause of the ripples seen in the energy distribution of the bunches. The energy spread can be reduced further by shaping the rf pulse to be slightly different from the linear ramp used here.

We must also run the bunches off-crest to do intrabunch energy compensation of the short- and long-range wakefields. The short-range wakefield used here is an average of the short-range wakes for individual cells of the detuned structure (Figure 7-14).

We assume each bunch has an approximately Gaussian distribution and divide the charge into nine equally-spaced macroparticles with Gaussian weight, assuming $\sigma_z = 100\ \mu$m. We seek the optimum phase for minimizing the energy spread by varying the rf phase, while also adjusting the height of the ramped rf pulse to keep the steady-state bunch centroid energy gain constant; the resulting energy spread as a function of rf phase at the bunch centroid is shown in Figure 7-32. There is some variation in the rms energy spread of individual bunches due to the effects of the long-range wakefields and the compensation scheme; thus optimization of BNS phase will be done for a bunch near the middle of the train which has an average energy spread.

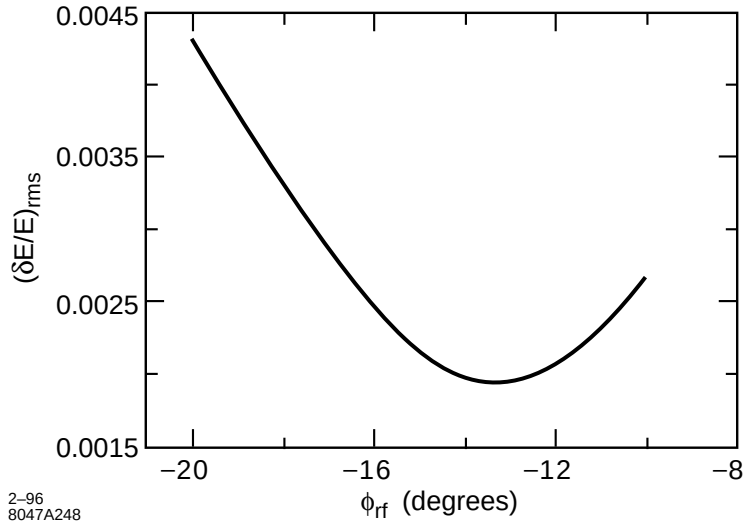

Figure 7-32. *The rms energy spread as a function of rf phase at the bunch centroid.*

Bunch Length Variations

Taking the bunch to be -13° off-crest (*i.e.*, 13° ahead of the crest, so that the tail receives more energy from the rf than the head, to make up for beam loading), we consider the effect of varying the bunch length, while keeping all other parameters constant. The effect on the rms fractional energy spread is shown in Figure 7-33.

Bunch Charge Variations

Taking the bunch to be -13° off-crest, we consider the effect of varying the bunch charge, while keeping all other parameters constant. The effect on the rms fractional energy spread is shown in Figure 7-34(a). The effect on the average (over all slices in all bunches) energy is shown in Figure 7-34(b).

RF Phase Variations

We consider the effect of rf phase ripple superimposed on the incoming 11.424-GHz rf pulse. Suppose the ripple is a cosine with given period (in ns) and amplitude (in degrees at the rf frequency).

It is essential to include dispersion of the rf pulse as it transits the structure, in order to treat this problem correctly. (If dispersion is neglected, a given bunch sees the same phase throughout the structure, since the variation of phase velocity with frequency, away from its value c at the rf frequency, is neglected.) Since calculations with dispersion are quite time consuming, we have treated each bunch as a single macroparticle for the calculations of Figure 7-35. Thus the contribution of intrabunch energy spread to the overall beam energy spread is not included. Here the amplitude of the ripple was taken to be 2°. Figure 7-35(a) shows the rms fractional energy spread as a function of the period of the ripple. Figure 7-35(b) shows the average energy as a function of the period of the ripple.

The variation of the energy spread scales approximately linearly with the amplitude of the ripple.

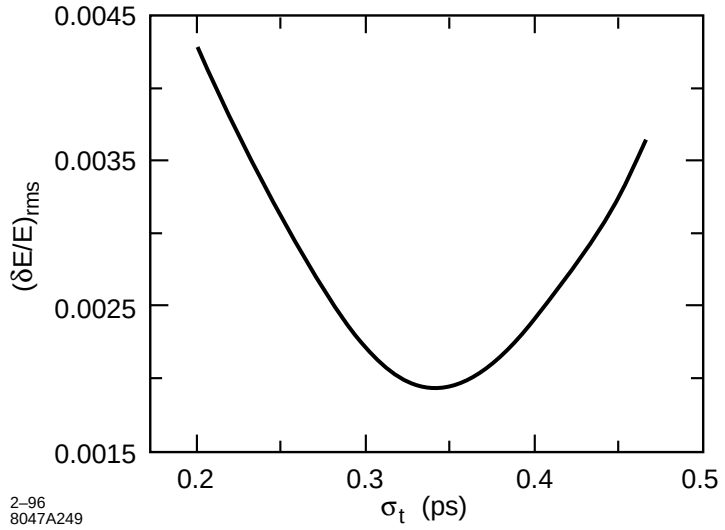

Figure 7-33. *The rms fractional energy spread as a function of bunch length, for bunches -13° off-crest.*

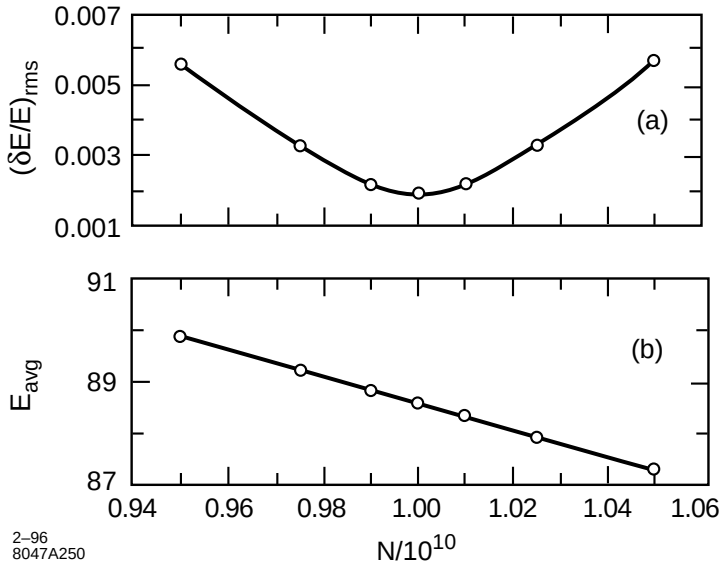

Figure 7-34. *(a) The rms fractional energy spread, and (b) the average (over all slices in all bunches) energy as a function of bunch charge, taking the bunch to be -13° off-crest.*

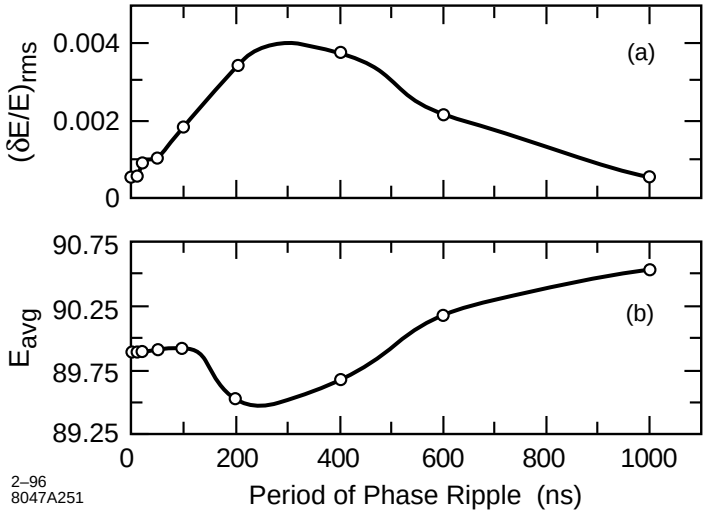

Figure 7-35. *(a) The rms fractional energy spread, and (b) the average energy, as a function of the period of phase ripple with an amplitude of 2°.*

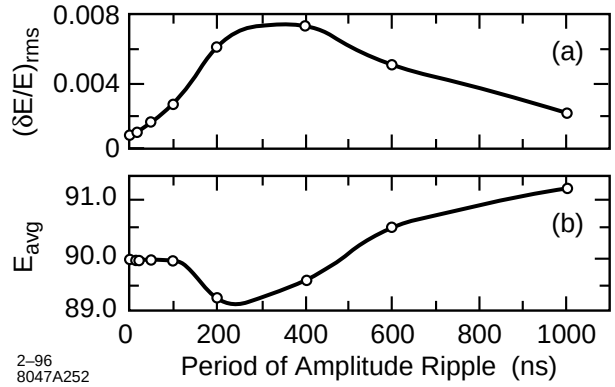

Figure 7-36. *(a) The rms fractional energy spread, and (b) the average energy, as a function of the period of ripple on incoming field amplitude. Amplitude of the ripple is 1 MV/m.*

Note that these are tolerances for variations that are the same from section to section. Thus they are pessimistic compared to tolerances for variations that are random from section to section.

RF Field-Amplitude Variations

We consider the effect of ripple in the amplitude of the incoming rf pulse. Suppose the ripple is a cosine with given period (in ns) and amplitude (in MV/m). We treat each bunch as a single macroparticle and include dispersion. Taking the amplitude of the ripple to be 1.0 MV/m, we obtain the result shown in Figure 7-36. Figure 7-36(a) shows the rms fractional energy spread (again ignoring the contribution from the intrabunch energy spread) as a function of the period of the ripple. Figure 7-36(b) shows the average energy as a function of the period of the ripple.

Again, note that for variations that are random from section to section, the tolerances should be looser than those computed here.

7.4.6 Multibunch Transverse Phase Space

In this subsection we discuss multibunch transverse phase space. Control of multibunch beam break-up has driven much of the work on accelerator structure design for the main linacs, since in the absence of a suitable cure (*e.g.*, detuning, damping of modes) it would be extremely severe. Some of the tolerances on the construction and alignment of these structures are very tight.

Structure Frequency Errors

The accelerating structures are designed to have a cell-to-cell variation in dimensions that detunes the dipole-mode frequencies and thus leads to a reduction in the amplitude of the long-range wakefield via decoherence of the modes. This frequency distribution is a truncated Gaussian (density in frequency space) and should be as smooth as possible to minimize partial recoherence of the wakefield over timescales less than or equal to the bunch train length. Small imperfections in the cell dimensions that lead to deviations in the mode frequencies by amounts comparable to or greater than the spacing between frequencies in the core of the Gaussian distribution produce a significant effect on the wakefield. The effect is worst if the frequency deviation is the same for a given mode in many or all of the structures. If, on the other hand, the frequency imperfections for the dipole modes are totally random from structure to structure, the effect is not as bad; in fact, randomizing the wakes at a given bunch spacing over a large number of sections can in some cases be beneficial.

Errors of 2.5 μm in the cavity diameter $2b$ produce fractional dipole frequency errors of about 1×10^{-4}. This is comparable to the fractional frequency spacing in the core of the Gaussian distribution used for detuning the structure.

The modification of the wakefield due to frequency errors has an effect on both the injection jitter tolerance and the misalignment tolerances. The effect can be quite significant for a detuned structure without any damping apart from the copper losses, and this was part of the motivation for going to the DDS.

Injection Jitter

There will be some offset of the injected trains with respect to the axis of the linac, and this offset will jitter from pulse to pulse. An off-axis bunch produces a transverse wake that drives bunches behind it. This wake must be kept small enough so that the projected multibunch emittance is not blown up significantly.

We have found that the emittance growth due to injection jitter is small if the envelope of the wake function is kept below about 0.8 V/pC/m/mm. For a structure with detuning alone, the wakefield envelope significantly exceeds this value even for a structure without fabrication errors (Figure 7-20).

As alluded to above, there are two extreme cases for the frequency errors: the case where the error in each frequency in the design distribution is the same in all sections (we denote this "systematic"), and the case where the error in each frequency is totally random from section to section. Note that our definition of "systematic" means that the errors are the same in corresponding cells of a given structure type, but they are still random from cell to cell in each structure type. In reality, the errors are not a simple superposition of these "systematic" and "totally random" errors, but for a first estimate, we shall treat them as such. Purely systematic errors of this sort would be a pessimistic extreme case. However, there will generally be some average error over all the cells of a given type, and this may be

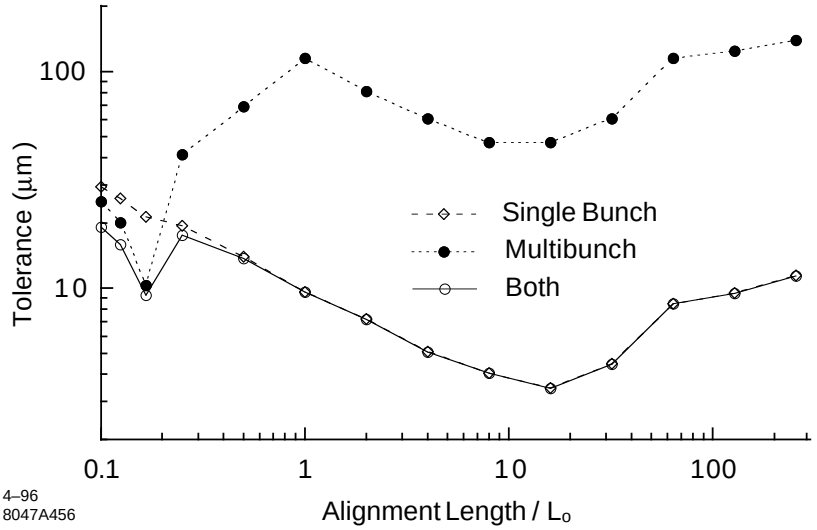

Figure 7-37. *Tolerance on the structure alignment for a 50% emittance growth in the NLC-IIb linacs as a function of alignment length, when considering only single-bunch effects, only multi-bunch effects, and both effects together.* L_0 *is the 1.8-m structure length.*

roughly approximated by the systematic component as defined here. Superimposed on this systematic distribution is the "totally random" component of the errors.

For a detuned structure with no damping, one finds that the blow-up of the betatron amplitudes of the bunches and the resulting multibunch emittance growth are unacceptably large. For the DDS, the situation is much better—even with systematic frequency errors with rms $\delta f/f = 10^{-4}$, the transverse blow-up and projected multibunch emittance growth are acceptable. This is quantified in Section 7.6.5 where we present multibunch simulation results.

Structure Misalignments

One of the tightest sets of tolerances for the NLC is that for the alignment of the DDS accelerator structures. We computed these tolerances by simulating beam transport in the linac, with the accelerator structures randomly misaligned in a piecewise manner. We considered alignment lengths (*i.e.,* piece sizes) ranging from multiples to sub-multiples of the 1.8-m structure lengths. For the sub-multiple lengths, the long-range wakefield was recalculated to account for the relative offsets of the cells.

In computing the tolerance for a given alignment length, a "seed" of random offsets was first generated for the structure pieces. The simulation program then "launched" the beam on axis and "steered" it to the centers of the quadrupoles, which were assumed to be perfectly aligned. Using the resulting emittance growth at the end of the linac and the rms of the piece offsets, the tolerance was computed for a 50% emittance growth.

For the NLC-IIb parameters, the average tolerance obtained from 100 seeds is shown in Figure 7-37 as a function of the alignment length. Three cases are plotted: one where only single-bunch effects are included in the simulation, one where only multibunch effects are included, and one where both are included.

In the figure, a relative minimum occurs in both the single bunch and multibunch curves near the alignment length of $20L_0 \approx 40$ m, which is the average value of the beta function at the end of the linacs; this is expected for a lattice for which $\beta \sim \sqrt{E}$. Also, for short lengths, the single bunch curve increases as the $-1/2$ power of the length: this

is because the wake kicks average out over distances shorter than the betatron wavelength. However, the multibunch curve drops for alignment lengths less than L_0 because the detuning is less effective in the shorter pieces. Finally, note that the combined tolerance is dominated by the single bunch effects except for alignment lengths less than about $0.2L_0$.

As with the quad alignment, we do not expect to align the structures with conventional techniques. Instead we plan to use the signals from the structure manifolds to align them relative to the beam. In Section 7.5.2 we discuss this procedure and the emittance growth that is expected based on the tolerances in Figure 7-37.

Ion Effects

In the NLC linacs, ions are created by collisional ionization of the residual gas. Light ions, such as hydrogen, are over-focused and lost between bunches, while in the first part of the linacs, heavier ions are trapped within a bunch train. Trapped ions affect the beam dynamics in three different ways. First, the additional focusing of the trailing bunches due to the ions will lead to an increased filamentation which is insignificant only for a vacuum pressure below 10^{-8} Torr [Raubenheimer 1992]. Second, the ions cause a nonlinear octupole-like coupling of horizontal and vertical betatron motion, whose effect is greatly reduced when the horizontal and vertical phase advances are separated by about 5% [Raubenheimer 1992]. Third, the coupled motion of beam and ions may result in a fast transverse multi-bunch instability of the electron bunch train in the linacs. If the pressure is 10^{-8} Torr, the expected instability rise time at the start of the Linac is about 160 ns [Raubenheimer 1995], assuming 90 bunches of 6.6×10^9 particles each (NLC-I) and carbon monoxide (CO) ions. The beam-ion instability disappears when the ions are no longer trapped within the train. The distance at which this happens depends on the beam current and on the ion mass. As an example, for a bunch train of 90 bunches and 6.6×10^9 particles per bunch, CO ions are trapped up to a beam energy of about 38 GeV, which corresponds to a distance of about 800 m in the NLC linacs. For an average CO pressure of 2×10^{-8} Torr and an initial bunch-to-bunch offset of $0.01\sigma_y$, the expected total dilution of the vertical emittance due to the beam-ion instability is then about 4% (or $\Delta\epsilon_{yN} \approx 2 \times 10^{-9}$ m). At 5×10^{-8} Torr, the dilution would exceed 100%. For higher beam intensities, less ions are trapped over a shorter distance, and the pressure tolerance is looser.

7.5 Alignment, Stability, and Feedback

In this section, we review the methods that will be used to align and stabilize the quadrupoles, BPMs and structures, and to control the bunch orbits and energies. These methods will be essential for the successful operation of the linacs. Without them, many of the bare alignment and stability tolerances could not be met.

For control purposes it is useful to consider separately short-term (seconds or less) and long-term (hours) variations in the linacs. While feedback systems will certainly be needed to control short-term variations, they will stabilize long-term changes as well. However, it is expensive to employ them everywhere, so one generally uses more invasive beam-based techniques, such as the "autosteering" and "phase-golding" procedures in the SLC, when dealing with long-term variations of large portions of the linacs. Thus we begin in the next section with a review of the error sources and their timescales. In particular, we examine the effect of ground motion on luminosity via the quadrupole vibration it generates.

We then turn to a discussion of the alignment of the quadrupoles and accelerator structures. The quadrupoles will be initially aligned using conventional methods. Achieving the required accuracy for long length scales ($\lambda > 200$ m) will be particularly important since beam-based methods are likely to be limited by systematic errors in this regime. As a prerequisite to the beam-based quadrupole alignment, the offsets of the BPMs with respect to the quadrupoles will be determined by changing quadrupole strengths and measuring the resulting orbit changes. The BPM electronics

will be designed to be stable over tens of hours to minimize the frequency of this procedure. Using the measured offsets, a beam-based quadrupole alignment algorithm will be run as a slow feedback loop ($\sim$30-min timescale) to limit dispersive emittance growth. As a fall-back position, beam-based correction schemes that are more invasive to machine operation will be used (*e.g.*, "dispersion-free" and "wake-free" steering).

For the accelerator structures, the alignment approach is to center them about the beam trajectory using as a guide the signals induced in their manifolds during the passage of the beam. This procedure, which we expect will be accurate to about $15\ \mu$m, will be iterated with the quadrupole alignment algorithm. Further discussion of the use of the DDS manifolds for measuring position of the structure relative to the beam is given in Section 7.10.3. In addition, or as a fall-back position, orbit bumps may be used to control the single-bunch emittance growth. Also, as discussed below, we will likely use multibunch feedback based on a fast kicker to control the projected emittance of the multibunch beam.

After the discussion of alignment procedures, we next consider how the beams will be stabilized using various feedback systems. We first discuss "fast transverse feedback" loops which will be used to stabilize the linac beam trajectory to ground motion and other disturbances that occur on timescales of a second and longer. These loops will measure the average properties of the bunch train with about a 100-nm resolution, and will reside in the five linac diagnostic stations. Information about corrections implemented at one station will be "cascaded" to subsequent stations, as is done in the SLC. As a fallback scheme to deal with ground motion, an expensive but realizable procedure is to implement feedback on each quadrupole based on information from a seismometer at the quadrupole.

Next we discuss bunch-by-bunch transverse feedback. Fast BPMs will be used to resolve transverse offsets at the sub-train level, and a fast kicker will be used to realign the bunches within a train. The main error source in this case is believed to be misalignments within and between accelerating structures, so the feedback loop will likely be operated at a relatively slow rate.

Some of the issues related to energy and energy spread have already been discussed, *e.g.*, manipulating the energy spread by the choice of rf phase profile along the linacs (Subsection 7.4.3) and the compensation of the heavy multibunch beam loading (Subsection 7.4.5). We conclude this section with a discussion of energy and energy spread feedback correction at the diagnostic stations. This last subsection also includes a discussion of linac energy management (LEM), which refers to the rescaling of the quadrupole magnet strengths when changes in the energy profile along the linacs are detected.

7.5.1 Error Sources and Timescales

For the NLC, it is important to know both the size and timescale of the sources of beam motion so that an efficient partition of feedback and alignment-type methods can be used. Data from the SLC linac operation gives us some measure of the quantities of interest. For example, attributing the Sector 18 position feedback corrections to the motions of quadrupoles between Sector 18 and Sector 11, where the next upstream feedback loop is located, yields a 0.3-μm to 0.6-μm-rms position variation per quadrupole on an hour timescale, and a 1.0-μm to 2.5-μm-rms position variation on a day timescale. These values are several times larger than can be tolerated in the NLC linacs if feedback is used only in the instrumentation regions. However, much of the apparent quadrupole motion in the SLC is likely to be the result of dispersion. The measured variations in the betatron phase advance between Sectors 11 and 18 correspond roughly to a 0.2% (0.6%) rms energy variation on an hour (day) time scale. Given the size of the quadrupole misalignments and the orbit bumps, these energy changes could produce orbit variations of the sizes observed. Thus we would need to suppress the dispersion in the SLC to be able to observe the level of quadrupole motion of interest. Until we get a better handle on the temporal characteristics of such motion, we will design correction systems that are as fast as possible.

As for fast beam motion ($f > 1$ Hz), the vertical beam jitter at the end of the SLC linac is about 40 times larger than can be tolerated at the ends of the NLC linacs. Part of the SLC beam motion is due to injection jitter; however, if one subtracts the component of jitter that is correlated with incoming beam motion, generally more than 70% remains. In studies of the jitter, we have observed that both the incoming and additive components have a white-noise-like spectrum above 1 Hz, so neither ground motion nor magnet power supply fluctuations are likely to be the cause. Also, the jitter is not strongly correlated with bunch intensity or energy variations. Understanding the sources of this jitter remains an important goal, for if they are present in the NLC, trajectory feedback will be of little help in this frequency regime, as is the case in the SLC.

Vibration and Ground Motion

At a minimum, there will be a trajectory feedback system in each of the five instrumentation regions of the linacs (see Section 7.5.3 for more detail). In each region, BPMs with resolutions of about 100 nm will measure the average bunch position in the train, and the information will be used to control the beam trajectory on subsequent pulses via air-core dipole magnets. How well these loops will suppress betatron motion will depend on the feedback algorithms chosen. Figure 7-38 shows the response functions of two example algorithms that sample the beam orbit at 120 Hz. The "Exp(-i/6) Weighted" routine applies a correction to the next pulse based on an exponential weighting (6 pulse time constant) of the current and previously measured incident beam trajectories. The algorithm is similar to that used in the SLC except that the correction is not delayed by two pulses. (Figure 7-42 shows the SLC response curve including the effect of systematic errors). The "Next Pulse" algorithm applies a correction to the subsequent pulse to remove any orbit deviation measured on the current pulse. It provides more suppression at low frequencies at a cost of a larger amplification ($\times$ 2) at high frequency. While the SLC loops sometimes oscillate, we believe that this problem will be solved to the degree that will allow us to achieve at least a factor of 10 suppression at 0.1 Hz in the NLC, even when including the complications associated with cascading the loops. We will also measure the stability of other algorithms to see if they would be practical to use as well.

If the ground motion in the NLC linac tunnel is comparable to that observed under "quiet" conditions in the SLAC linac tunnel, then its impact on the NLC luminosity should be small when the effect of trajectory feedback is included. To see this, we compare the measured ground motion spectrum with the tolerances. Figures 7-39 and 7-40 show the measurements of the differential and integrated ground motion spectra, respectively, that were made at SLAC as part of the ground motion study discussed in Appendix C. The power spectrum is actually the average of 10 spectra measured in Sector 4 of the SLAC linac on different days at 2 AM. The average power curve was used to compute the integrated spectrum which is the vertical rms ground motion that would be measured if only frequencies above the frequency plotted contributed to the motion (the plateau in the spectrum near 10 Hz results from the resonant vibration of the accelerator structure support system). Also shown in this figure are the ground-motion tolerances described in Section 7.4.4, "Single-Bunch Transverse Phase Space", for pure wave-like motion ("Waves"), and for wave-like plus uncorrelated motion ("Waves + Noise"), where as a worst case, an uncorrelated ground motion component equal to the seismometer electronic noise contribution to the measured power spectra is included. In addition, tolerances that include the effect of trajectory feedback, "Waves + Noise + FB", are plotted. They were generated by dividing the "Waves + Noise" result by the suppression obtained with the SLC-like "Exp(-i/6) Weighted" feedback algorithm. At frequencies where the integrated spectra are rapidly decreasing, one can compare the integrated spectra directly to the tolerance curves since most of the rms motion at any particular frequency is dominated the motion near that frequency.

The net effect on the luminosity is obtained by integrating the power spectrum weighted by the inverse square of the tolerance. For $f > 0.01$ Hz, this yields a luminosity reduction of 0.12% for the "Waves" case, 20% for the "Waves + Noise" case, and 0.13% for the "Waves + Noise + FB" case. Thus, the addition of feedback will still yield a small luminosity loss in the worst case scenario where uncorrelated ground motion is "hiding" just below our seismometer noise limits. Feedback will also be important for suppressing the non-wave-like components of ground motion that are significant at frequencies below 0.01 Hz.

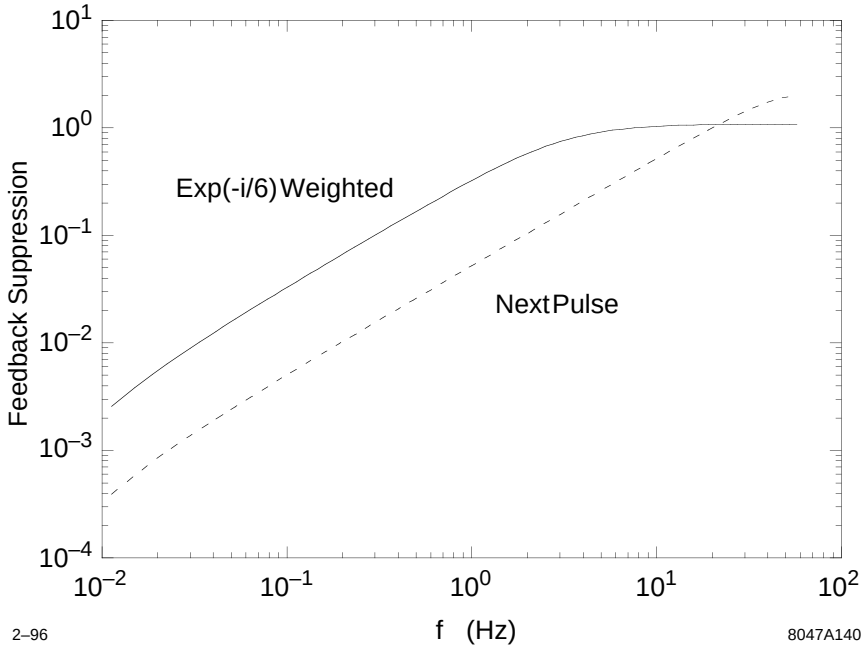

Figure 7-38. *Feedback response curves for an algorithm that exponentially weights the previous pulses (solid) and for an algorithm that makes a 100% correction on the next pulse (dashed).*

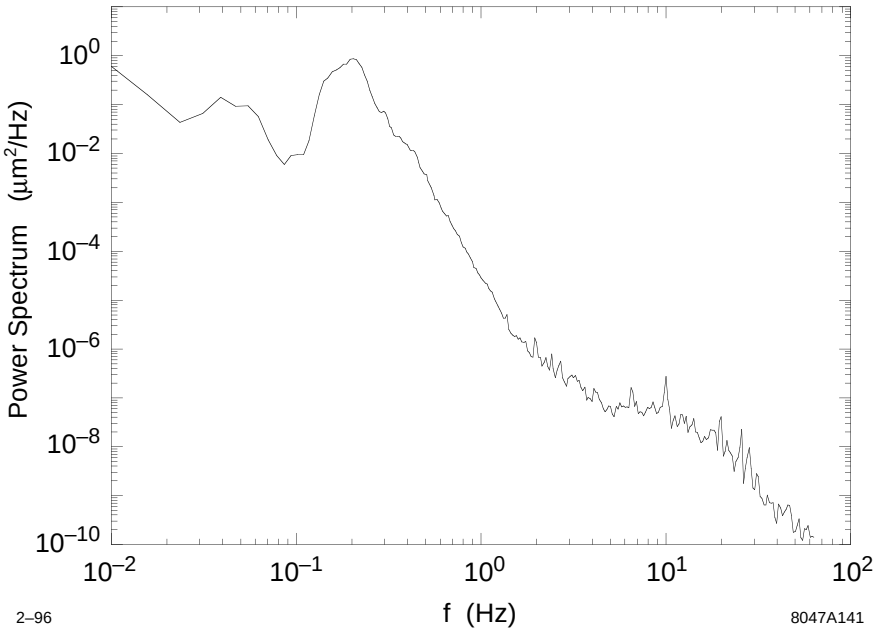

Figure 7-39. *Average of 10 vertical ground motion power spectra that were measured on different days in Sector 4 of the SLC linac at 2 AM.*

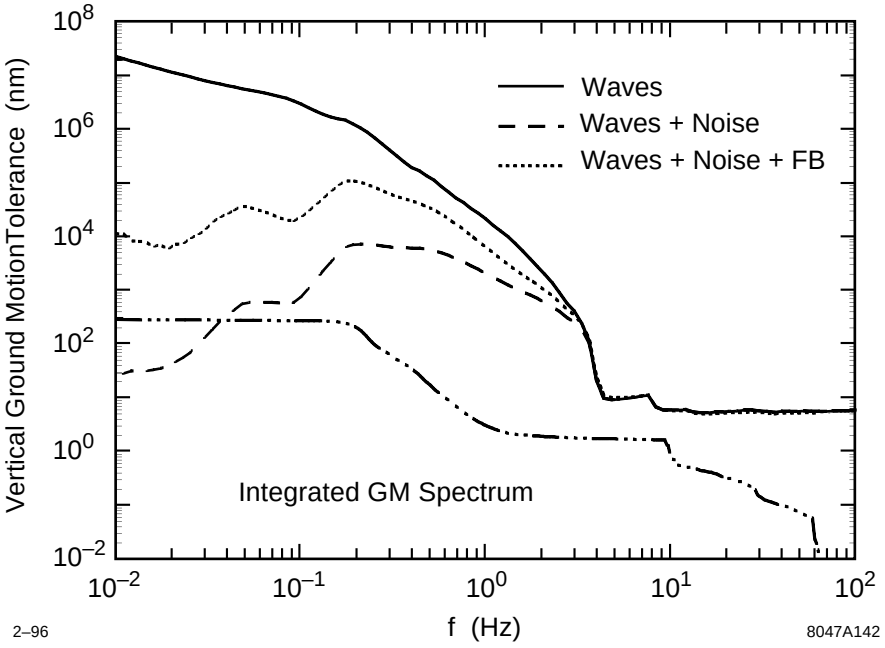

Figure 7-40. *Integrated vertical ground motion spectrum (dot-dashed) and tolerances on the vertical rms ground motion for a 1.5% luminosity reduction for three cases: pure wave-like motion (solid), wave-like plus uncorrelated motion equal to the seismometer electronic noise (dashed), and feedback suppressed wave-like plus uncorrelated motion (dotted).*

The contribution to quadrupole vibration from "cultural" sources is hard to estimate since a site for the NLC has not been chosen. However, if the daytime activities at SLAC are typical of what will occur around the NLC, then the effect on quadrupole motion should not be large since the daytime tunnel measurements at SLAC generally do not exceed the tolerances in Figure 7-40. Also, vibration due to quadrupole cooling and support appear not to be a big problem. Seismometer measurements that were made on top of the quadrupoles and on the floor in the FFTB show that there is only a few nm of relative motion ($f > 0.1$ Hz) between them when the quadrupoles are powered.

As part of evaluating an NLC site, ground motion measurements will be made to obtain the power and correlation spectra. If the ground motion is much larger than that presented above, or if the motion is less correlated over long distances, active types of damping could be used to suppress the effect of the motion on the beam (passive damping would probably be difficult to implement below 10 Hz). For example, the vertical quadrupole vibrations could be measured with seismometers and fed back to fast corrector magnets that would offset the quadrupole kicks. A feed-forward scheme could also be used at the end of the linacs where the measured position of the first bunch in the train would be used to correct the motion of later bunches in the same train. However, limitations due to bunch filamentation would only loosen the quadrupole vibration tolerances by about a factor of three in this scheme.

7.5.2 Alignment Procedures

Quad and BPM Alignment

The initial placement of the quadrupoles and structures will be done with conventional surveying techniques. Most likely, triangulation and leveling methods will be used in combination with Global Positioning System (GPS) data from

satellites. The long-range alignment accuracy will be within the dispersion related tolerances shown in Figure 7-24. However, at wavelengths less than a few hundred meters, the accuracy will level off to something that approaches 100 μm on a 20-m scale. At these wavelength scales, a beam-based approach will be used to control the quadrupole alignment. Beam-based methods tend to be sensitive to systematic errors at longer length scales, which is why we will rely on the initial placement accuracy to achieve the long-wavelength tolerances. As noted earlier, if the displacements due to ground settling significantly exceed the long-wavelength tolerances, a global realignment of the beam line will be done. Hydrostatic monitors may be installed along the beam line to monitor these displacements.

The beam-based quadrupole alignment will use as input the measurements of the average bunch positions from the BPMs that will be located in the quadrupoles. Various beam-based algorithms have been shown to work in theory, although there are many subtleties involved because the derived quadrupole offsets have correlations which vary with length scale. Thus one does not speak of the level of alignment achieved, but instead judges the method in terms of the amount of dispersion remaining on average after alignment. Given that there is some uncertainty as to how often the dispersion correction will have to be made, the correction procedure should be designed to be as fast as possible. Also, the correction will be made by moving the quadrupoles with mechanical movers as opposed to using dipole corrector magnets to offset the quadrupole magnetic centers. This will be done in part because a large investment in mechanical movers will be made for the structures, so adding additional movers (about 14% more) for the quadrupoles will be straightforward. Also, having the beams nearly centered in the quadrupoles alleviates the need for a tight regulation of the quadrupole power supplies, and a tight limit on higher harmonics of the fields.

Given these considerations, we plan to use a quadrupole alignment algorithm that requires only beam trajectory data taken with the nominal linac lattice. Having readings from N BPMs in N quadrupoles will allow us to determine $N-1$ quadrupole offsets, with the alignment end-points being the beam position in the first quadrupole and the BPM zero of the last quadrupole: the outgoing beam angle is unconstrained. Using this algorithm, we will align N-1 quadrupoles at a time, one group after the next, similar to the way that "autosteering" is done in the SLC linac. However, some global limitations in the quadrupole moves would have to be made to prevent the mechanical movers from "ranging-out."

This method will require BPMs with resolutions of about a micron. Such BPMs already exist, however they must also be aligned to the quadrupole magnetic centers to this same level (see reference [Adolphsen 1993] for more detail). This alignment can also be computed in a beam-based manner, but may be disruptive to normal operation. For example, the offsets could be derived from the BPM data taken in which the strengths of individual or strings of quadrupoles are changed. However, the changes in the quadrupole strength would have to be fairly large—turning off one quadrupole yields a betatron oscillation with an amplitude that is only a few times the size of the beam offset in the quadrupole. Thus we want to minimize how often we have to perform this procedure. A calibration scheme that injects signals into the BPMs, and not just into the readout electronics, should help to stabilize the offsets. This is discussed in Section 7.10. Tests of the BPM stability in the SLC and FFTB will be done to study this problem.

Due to the effects of wakefields, it is hard to accurately estimate by analytical means the emittance growth that remains after applying the quadrupole alignment algorithm. Instead we simulate the application of this algorithm to the linac; the methodology and results are presented in Section 7.6.

Structure Alignment

As described in Section 7.3.3, the accelerator structures are supported in pairs on common strongbacks, which themselves are mounted on structure movers. The alignment of the structures will be based on measurements of the beam position relative to the structure axes that will be obtained by analyzing the dipole-mode signals from the structure damping manifolds. Although the original motivation for adding the structure manifolds was to damp the dipole modes, their capacity to be used as a BPM with micron-level resolution will be essential as well.

In the readout electronics, the signal from two modes near the ends of the structure will be selected with filters and measured so that both the position and orientation of the structure relative to the beam can be determined. The difference in the measurements from each structure pair will be used to check the relative structure alignment on the strongback, while the average of the measurements will be used to remotely adjust the mover positions at the micron level to better center the structure pair about the beam trajectory.

The accuracy of the structure alignment system will depend on the degree to which we can internally align the structures. Since we do not have much experience aligning single structures, let alone preserving the alignment of a pair of structures in an operating environment, we have tried to be conservative in our estimates. We believe that structure pairs can be made straight to better than 15 microns rms, and that this alignment can be maintained over long periods of time. Thus far, we have achieved straightnesses of a few microns for the 40-cell stacks that are built before being combined into 206-cell structures. As we assemble whole structures and monitor their straightness, we will be able to better characterize the misalignments.

For now, we assume 15-micron-rms misalignment. To estimate its effect on the beam emittance, we consider two cases whose contributions sum to the general case. In the first case, we assume that the beam travels along the mean axis of the structure pairs, which suppresses the short-range wakefield effects. This leaves the growth due to the long-range wakefields which depends on the spatial correlations of the misalignments. This dependence is shown in Figure 7-37 where the tolerances for piece-wise misalignments of the structures are plotted as a function of the length of the pieces. From these tolerances, a 20% vertical emittance growth is expected if the offsets are uniformly distributed in piece length. This growth will be larger if the offsets occur mainly on a length scale equal to 1/6 of the structure length. To be conservative, we have budgeted 40% emittance growth for these long-range wakefield effects.

In the second case, we assume that the structure pairs are perfectly aligned internally, and consider how well the beam can be aligned to the mean axis of the pair, which was assumed to be done exactly in the first case. Since we expect that the resolution on the beam position derived from the structure signals will be a few microns or better, the alignment accuracy will be dominated by the 15-micron-rms structure misalignments (note that we consider the internal misalignments for this purpose even though they are ignored in this case for the wakefields that they generate). Having four measures of the beam position relative to the axis of a structure pair yields a 7.5-micron-rms beam-to-structure alignment. The resulting vertical emittance growth, which is dominated by short-range wakefield effects, is about 50% based on the Figure 7-37 tolerance for an alignment length of two.

In this analysis, we have ignored systematic distortions of the structure pairs. However, they will likely occur on length scales where the internal alignment tolerances are large. For example, if the pairs bow with a 100-micron sagitta, the emittance growth due to long-range wakefield effects will only be a few percent. The short-range wakefield effects, which depend on the average bunch offset in the structures, would be suppressed in this case since the strongback would be aligned based on the beam offset measurements at the ends and middle, which would center it about the beam.

During the commissioning of the NLC, the structure alignment will be done with a low-intensity beam so as to minimize the wakefield steering effects (*i.e.*, one does not want large orbit changes after moving one pair of structures). During normal operation, it is likely that the structure alignment procedure will have to be iterated with the quadrupole alignment algorithm since moving the structures will kick the beam. If only the power in the wake signal is measured, a scan of the structure position versus signal would be needed to determine the direction to move the structure, which could significantly slow the alignment process. Prototype tests of a structure alignment system will be done in ASSET and the NLCTA to help resolve such issues.

7.5.3 Fast Transverse Feedback

In this section we discuss the feedback systems in the main linacs which operate on relatively fast timescales. The primary focus is on the transverse feedback loops which correct the average trajectory of the beam at the diagnostic stations along each linac, but the general principles are applicable to other loops as well.

A generalized feedback system has been developed and commissioned in the SLC, and has been essential to high-luminosity operation. Operational experience has provided valuable information on feedback-response characteristics, especially with regard to machine and feedback-system imperfections. The proposed NLC feedback is based on the SLC design, with some changes based on lessons learned from the SLC and performance requirements of the NLC. Appendix D provides more information on the design and characteristics of the feedback system. This chapter concentrates on design and performance issues for the NLC linacs.

Linac Feedbacks

In each linac, there are five diagnostic sections, each with a feedback loop. Each loop includes measurements of 10 BPMs for launch control, in addition to one or two BPMs which provide energy information. Each feedback loop calculates and controls five states: the X and Y positions and angles, and the beam energy. To provide feedback control of the launch parameters, two X correctors and two Y correctors are needed. For the energy control, klystron phase or amplitude controls may be used. The feedback design assumption is that the actuators can change to a new setting within one 180-Hz pulse, or 5.55 milliseconds. An additional beam pulse period is allowed for BPM digitization, feedback calculations, and communication. The result is that, after a beam perturbation is detected by the feedback system, the feedback begins to correct it two 180-Hz pulses later. For the initial NLC design, the correction begins two 120-Hz pulses after a perturbation.

Feedback System Design

The feedback design is based on the state space formalism of digital control theory. It uses a Linear Quadratic Gaussian (LQG) controller, which has a built-in model of the beam transport and the expected beam and BPM noise characteristics. Matrices are designed and calculated offline and downloaded for use by the real-time feedback system. The mathematical design goal for the feedback matrices is to minimize the rms of the beam states over time, given the noise inputs. By modifying the input beam noise design assumptions, it is possible to tune the feedback performance response characteristics. The initially proposed feedback algorithm does not adapt to modeling or noise spectrum changes, consistent with the current SLC design. It is hoped that in the future, adaptive methods may provide improved performance, but there is insufficient experience to make design assumptions with them at this point. The beam transport model within a single loop (*i.e.*, R12s which take beam position monitor readings and corrector settings to beam positions and angles) may either be derived from the accelerator model, or may be measured by an invasive online beam-based calibration method.

In the linacs, a series of feedback loops are controlling the same beam parameters (positions, angles, and energy) at different points along the beam line. If the loops do not communicate with each other, this would result in overshooting of the feedback corrections and excessive amplification of beam noise. To avoid this problem, a "cascade" system is developed. The goal of the cascade system is that each feedback loop responds only to perturbations which are generated immediately upstream of it. If the beam transport is approximately linear, this can be accomplished by having each loop send its calculated states to the next downstream loop. The downstream loop mathematically transports the upstream states to its own fit point, then subtracts them from the positions and angles calculated from its own BPMs. This scheme is depicted in Figure 7-41. With this design, each upstream feedback sends information

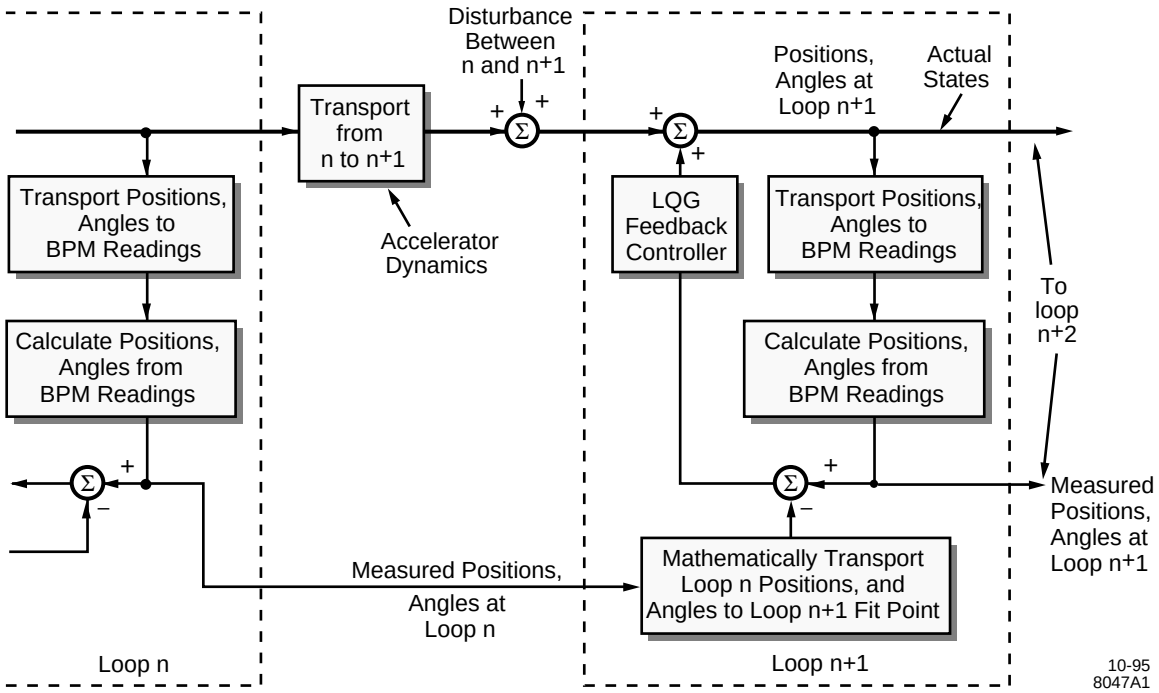

Figure 7-41. *Schematic of cascaded feedback system.*

only to the nearest downstream loop. The key is that each loop is sending the next loop information about what it measured in the beam, not what it is correcting. For example, if there is a perturbation upstream of Loop 1, this perturbation should be seen by all of the feedback loops. Loop 4, for example, will see it, and send this information to Loop 5, which will subtract the perturbation from what it has, so Loop 5 will correct nothing. Loop 5 doesn't know or care whether Loop 4 is correcting the perturbation, it just knows that someone upstream is taking care of it, and actually Loop 1 will correct it. This scheme assumes that the beam transport is linear and independent of the source of a perturbation. (If the NLC transport is excessively nonlinear, it may be advisable to consider a more complicated communications algorithm, where downstream loops receive information from all upstream loops and have sufficient information about the source of a perturbation.)

An important issue in the cascade design is how to mathematically transport the beam from one feedback loop's fit point to the next loop. The distance between feedback loops is so great that the accelerator model is not good enough, and SLC experience has shown that the interloop beam transport changes with time. In the SLC, adaptive techniques are used for the mathematical transport calculations, but the adaptively calculated transport matrices have had some performance problems which degrade the feedback system performance. These problems are described fully later in this chapter and in the feedback appendix. As a result, the proposed method for interloop mathematical beam transport for the NLC is to steal a small number of beam pulses each hour to measure the beam transport by perturbing the beam. It should be possible to provide an adequate measurement by producing a single set of perturbations upstream of the series of feedback loops, and measuring the interloop transport elements for all downstream loops at once.

Operational Performance Issues

SLC feedback performance studies have included five main areas of interest: slow correctors, downsampled feedbacks, poor modeling of beam transport within a feedback loop, poor cascade modeling of interloop beam transport, and optimization of the feedback design response. Slow corrector response has had a detrimental effect on SLC feedback performance, but a new design now allows response within a single beam pulse. In the SLC, due to CPU and BPM constraints, many feedback loops operate at lower than the full 120-Hz beam rate. This degrades the feedback response, and increases aliasing of higher frequency noise to lower frequencies. For the NLC, sufficient CPU and BPMs will be available so that the feedback loops may run at the full machine rate. The remaining performance issues are more challenging, and are interrelated.

While it should be possible to develop a nearly perfect model of the accelerator beam transport within a single feedback loop, SLC experience has shown that the model has imperfections in some cases. Performing the calibration procedure for several SLC feedback loops has provided data to quantify the effects of typical imperfections (these involve errors in the R matrices between correctors and states of 10–20%). NLC design simulations include consideration of comparable imperfections.

If the long-range beam transport in the NLC linacs is reasonably linear and not changing quickly with time, then measuring the interloop transport elements every hour should provide perfect cascade correction, and each loop should perform corrections only on perturbations generated immediately upstream. If this were true, the global system feedback response would be identical to the response of a single feedback loop. But to be conservative and account for small nonlinearities and changing beam transport properties, NLC feedback simulations assume that part of a given beam perturbation leaks through to the downstream loop, so that each loop incorrectly compensates for a portion of an upstream perturbation. In the simulations, it is assumed that each loop compensates for 15% of perturbations which are not immediately upstream.

The SLC design's noise response results in correction of a beam perturbation exponentially with a time constant of about six pulses. In other words, after six pulses, most of an incoming perturbation is fixed by the feedback. This design provides a good response to a step function and provides a stable feedback which does not over-react to white noise. For the NLC, it is preferred to have a feedback response which is tuned to damp strongly at low frequencies. In the NLC, high-frequency noise is expected to be damped by passive systems and the expected input noise spectrum would be dominated by low-frequency ground motion. Note that while it is possible to tune the feedback response curve, any design will damp at some frequencies while amplifying at others. Several alternative noise designs have been simulated and evaluated. While the more aggressive designs, which damp strongly at low frequencies, provide an excellent response curve under perfect conditions, these designs are more sensitive to imperfections in both intraloop modeling and interloop cascade transport. To provide a stable, robust feedback system with better response at lower frequencies, more work must be done. Figure 7-42 shows the feedback response curve for the SLC feedback design, which includes the effects of imperfections. Note that this curve is for a 120-Hz beam pulse and feedback rate. If the rate is 180 Hz, the response curve would be similar but shifted in frequency. At this point, the SLC design is proposed as a conservative initial approach, which provides adequate response and is not unduly sensitive to machine and modeling imperfections.

7.5.4 Bunch-by-bunch Transverse Feedback

The fast-feedback systems described in the preceding section operate on averages of the bunches in a train. The repetition rate of these loops is relatively fast. We turn next to loops which distinguish variations within a bunch train, but which perform corrections less frequently than the “fast” feedback loops previously described. It is probably not

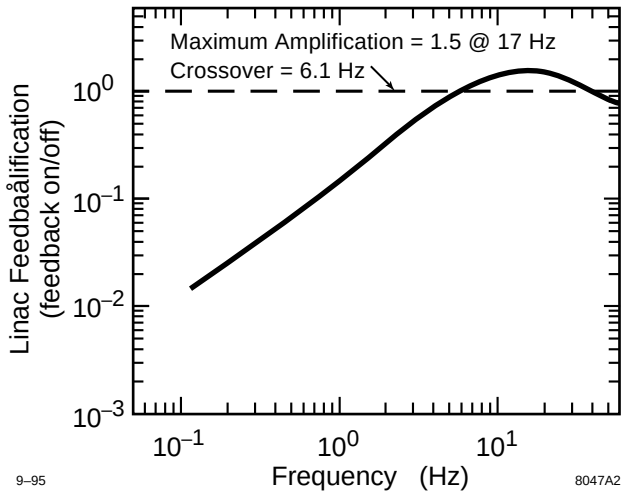

Figure 7-42. *Feedback response curve for the SLC feedback design with a 120-Hz beam pulse and feedback rate, including the effects of imperfections.*

necessary to resolve all the bunches individually, but it is necessary to have some resolution within the train in order to control the multibunch emittance (and also bunch energies and energy spread, as is discussed later in this section).

These bunch-by-bunch feedbacks will also be implemented in the five diagnostic/control sections along each main linac. Measurement of the individual transverse bunch positions will be at these stations using special fast BPMs. Trajectory correction will be done using high-bandwidth kickers, able to tailor the kick delivered to individual bunches assuming the variation is fairly smooth along the train. Simulations yielding the requirements on BPM resolution, kicker strength, and kicker speed are given in the next subsection, and a design for a high-speed kicker suitable for use in such feedback loops is given in 7.9.4.

Multibunch Kicker Simulations

In the multibunch kicker simulations, bunch-by-bunch trajectories were assumed to be measured by two fast BPMs located at consecutive vertically-focusing quadrupole magnets (90° phase difference) at five locations in the NLC-I linacs: 30 GeV, 60 GeV, 100 GeV, 150 GeV, and 250 GeV; these positions closely correspond to the locations of the diagnostic stations. Two fast kickers were also located at consecutive vertically-focusing quadrupoles just upstream of the BPMs and the bunches were kicked to line all bunches to the trajectory of the first bunch. One-to-one trajectory correction was also performed to ensure that the beam centroid passes through the center of every focusing quadrupole magnet.

The tracking was performed with 90 bunches including both single- and multi-bunch effects. Each structure was divided into seven pieces and the pieces were aligned independently with rms errors of 25 μm. This misalignment was chosen so that the multi-bunch effects are much stronger than single-bunch effects because we are concentrating on multi-bunch correction. But, because it is possible that single-bunch effects become significant due to a large bunch offset caused by the multi-bunch effects, the single-bunch effects were also considered in this simulation. The expected emittance growth without corrections was simulated to be $\Delta\epsilon_y/\epsilon_y$ = 133%.

Figure 7-43(a), (b), and (c) show emittance growth as a function of the kicker strength, BPM resolution, and kicker speed, respectively. The kicker strength of 56 kV corresponds to a deflection of roughly six times the beam size. The residual emittance that remains after the correction is primarily due to the single bunch emittance dilution that arises

from the misaligned structures and the large bunch offsets between correction stations. Finally, Figure 7-44 shows the effect of the kickers in one simulation with 25-μm-rms accelerator structure piece misalignments. The uncorrected emittance dilution was greater than 150% in this case. The residual dilution after correction is roughly 15%.

Given these results, we will design a kicker with a speed of 250 MHz and a strength of 56 kV, and a bunch-by-bunch BPM with a resolution better than 0.2 μm. This is discussed further in Section 7.9.4.

7.5.5 Linac Energy Management and Energy Feedbacks

The energy management of the main linacs includes the measurement of the energy, energy feedback and feedforward, the control of energy and magnet strength settings along the linacs, the handling of vetoes due to klystron faults, control of individual amplitudes and phases of the klystrons, and the confirmation of these parameters with beam-derived data. The energy spread within a bunch, which can be controlled by phase adjustments, is also discussed in this section.

Energy Measurement

The energy of the beam will be measured in high-dispersion regions that provide resolutions of about 0.1% or better. Five diagnostic stations are envisioned for this purpose, as discussed in Section 7.3.4. These stations will also be able to measure the energy variation along the bunch train.

Measurements of other quantities will also be important since they will influence the energy. Among these are the bunch train current and distribution, the beam phase, the state of the upcoming klystron pulses (*e.g.,* OK, veto, or in transition), cascaded information from upstream feedbacks, and any other information (such as history of slow ramps in current and energy) that is relevant to controlling the energy of the bunches.

Energy Correction

The energy correction consists of a system of phase shifters, which will adjust the phase on a pulse-to-pulse basis like the SLC energy feedback loops. The slope and higher orders of the energy profile of the bunch train will also need to be controlled (this is discussed in Section 7.4.5 and at the end of this section).

Depending on the information source, the correction will be a feedback or feed-forward system. These systems should have a very general design with a self-calibrating mechanism. They should also allow auxiliary inputs and outputs (for instance, dumping the beam instead of correcting it).

A feed-forward system like that in the SLC will be necessary for different beam currents. By measuring the charge of each bunch in the damping ring and correcting the rf amplitude by opposite phase settings of two subboosters, good beam loading compensation can be achieved. Due to the high beam loading of about 25%, small current changes of 1% already cause a 0.25% energy change. The feed-forward information needs to be forwarded to the five energy stabilization stations (upstream from the chicanes) and combined with the local feedback.

Linac Energy Management

The management of the energy along the linacs is as important as controlling the energy at the ends, especially if a change in the energy profile might change a tail cancelation into an addition. Switching a klystron is probably the

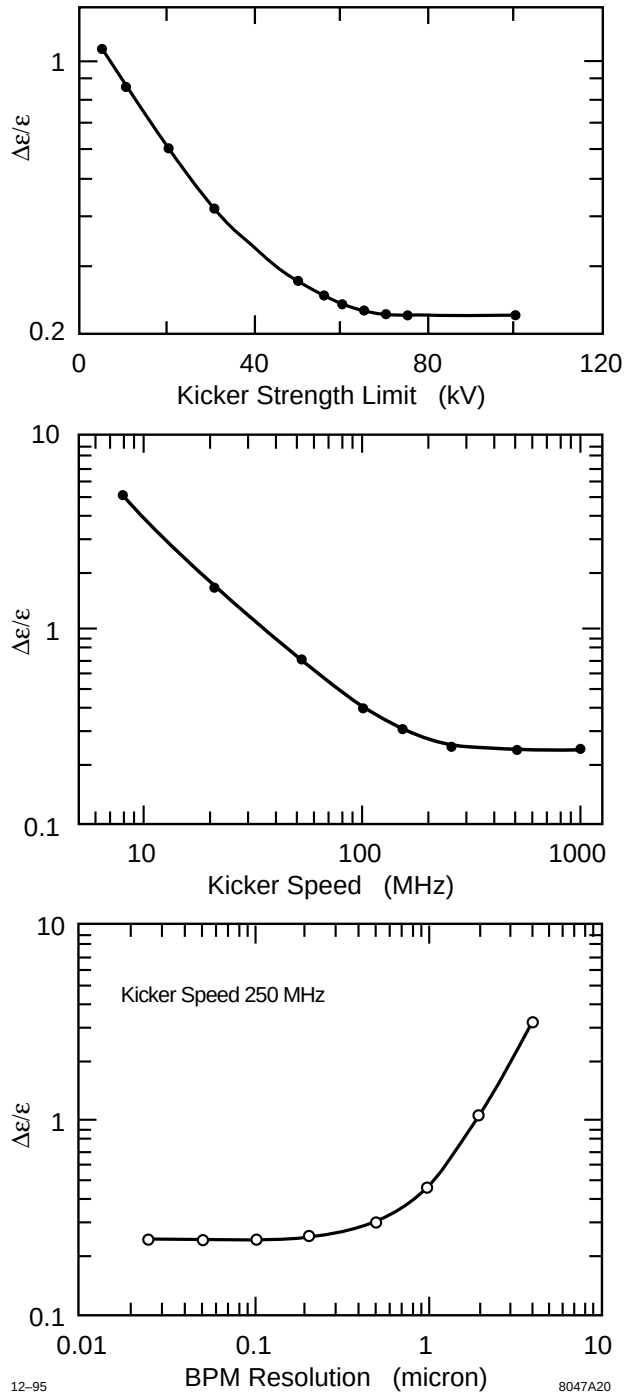

Figure 7-43. *Emittance dilution versus: (a) kicker strength for a kicker speed of 250 MHz and a BPM resolution of 0.2 μm; (b) kicker speed for a kicker strength of 56 kV and a BPM resolution of 0.2 μm; (c) BPM resolution for a kicker strength of 56 kV and a speed of 250 MHz. Each structure was divided into seven pieces with a random misalignment of 25 μm rms. Each symbol represents the average of tracking with 25 random seeds. The residual emittance dilution is due to the single-bunch dilutions arising from the trajectory and structure offsets.*

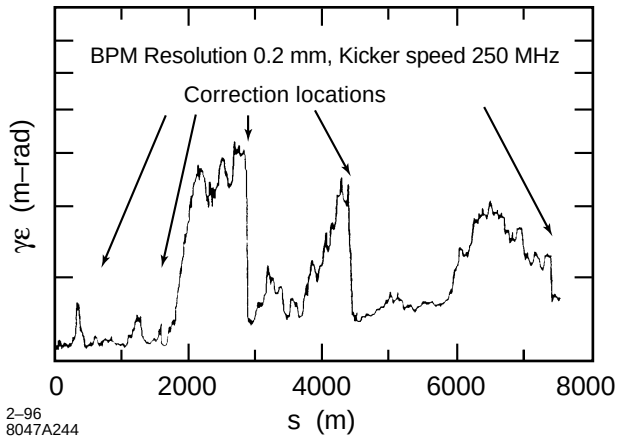

Figure 7-44. *Example of a kicker simulation with 25-μm rms accelerator structure piece misalignments.*

most important single event which requires a linac energy management (LEM) operation, that is, an adjustment of the magnets to reestablish the matching of the beam to the lattice. For this procedure we have to know the local beam energy and the energy gain (amplitude) and phase of the klystrons. The rf parameters should be checked with beam measurements. Also, the lattice should be checked with diagnostic pulses—special beam pulses which are transversely kicked and therefore oscillate down the linacs giving the required lattice information.

Another energy-related problem in the SLC that makes LEM necessary is changes in temperature which can generate energy variations of up to 2%. The linearized LEM adjustments help but are not sufficient so that the above mentioned additional tools will be helpful, especially in the front part of the main linacs. The NLC at 500 GeV is about 10 times less sensitive to energy changes of one klystron (230 MeV) than the SLC. But it has also to maintain 100-times-smaller emittances. One klystron powers two structures (NLC-I) producing 100 MeV, which is 0.1% of the energy at 100 GeV, but 1% at injection where the energy is 10 GeV.

Bunch-by-bunch Energy and Energy Spread Feedback

It will be necessary to control the effects on the energy and energy spread of the multibunch train due to variations in the energy profile delivered by the rf system and to variations in the bunch charges. As discussed previously in Section 7.4.5, multibunch energy compensation can be done by shaping the rf pulse to simulate the steady-state beam loading profile before the beam is injected. Nearly ideal compensation of the beam loading will be obtained by a programmed series of phase shifts during the rf pulse (see Chapter 8 for details). However, there is no reason that the phase variations cannot be modified to obtain a slightly different shape to the rf pulse. A feedback system could thus be designed to fix small variations in energy along the bunch train, assuming the variation is smooth enough that the klystron variability has sufficient bandwidth.

Bunches belonging to a given train in the damping rings ride at different synchronous phases due to the differing amount of beam loading from bunch to bunch. The beam loading in turn depends on the bunch charges, which may vary on a pulse-to-pulse basis. We may have to compensate for such pulse-to-pulse variations by feedforward of bunch charge information from the damping rings to the main linacs.

7.6 Simulation Studies

The previous sections describe the basic design of the NLC main linacs. The results of analytical estimates and numerical simulations were used throughout the text, mainly to discuss and justify specific design choices. In this section, we describe numerical calculations that were performed to study the NLC main linacs in greater detail. By assuming realistic errors in all major accelerator components, we can study the complex interactions between different mechanisms of emittance growth and the proposed correction algorithms. Since stability problems are of major concern for the NLC, we also discuss simulation results for the alignment stability in the NLC main linacs.

In the following, we will briefly describe the simulation program LIAR ("LInear Accelerator Research code") which was recently developed [Assmann 1995]. Then, we discuss the overall objectives for the NLC linac simulations and present the simulation results. A final outlook will present the conclusions and will describe directions for future work.

The goal of the simulation studies done so far is to show the feasibility of the acceleration and emittance preservation in the NLC linacs. Several important problems still do not have their final solutions. However, we will show that we have working solutions to the major problems that already fulfill the requirements.

7.6.1 Simulation Program

The simulation and tracking program LIAR ("LInear Accelerator Research code") is designed as a general tool to study the beam dynamics of linacs. LIAR's major design goals are to provide a simulation platform that includes all the basic accelerator physics for linacs, that allows to add easily advanced features and that is not bound to a specific linac design. Presently LIAR is used both for NLC and SLC simulations. We briefly describe its main features and observables.

All magnets are simulated using the thick lens representation. The beam line description includes "realistic" support points with a number of elements mounted on a common girder. Thus we can simulate the effects of ground motion and we can also study correction algorithms using movers at the support points. Rf structures can be divided into pieces and have an rf-BPM assigned at both ends.

The beam is described as a train of bunches. Each bunch is divided into slices along the longitudinal direction and each slice is described by a number of mono-energetic beam ellipses. The tracking part of the program performs a 6D coupled-beam transport including the beam-induced transverse and longitudinal wakefields in the rf structures.

The basic features of the simulation program are complemented by the ability to set random and systematic errors on most accelerator parameters:

1. Transverse misalignments and roll angles for most element types.
2. BPM misalignments with respect to the quadrupoles. Finite BPM resolution.
3. Strength errors for quadrupoles, bending magnets and correctors.
4. Phase and gradient errors of the rf structures.
5. Random or "ATL"-like misalignments of the accelerator support.
6. Misalignments of individual rf structure pieces ("bowing", etc.).

Given those capabilities we can simulate basic and advanced optimization schemes for the main linacs of NLC. So far the following correction methods have been implemented:

1. One-to-one steering using dipole correctors.
2. Trajectory feedbacks.
3. Beam-based quadrupole alignment.
4. Beam-based alignment of the rf structures.
5. SLC-type emittance bumps with deterministic optimization.

Other optimization schemes like dispersion-free steering or multibunch kickers will be added in the future. All those correction schemes can be applied and tested in the presence of multiple interacting error sources. Furthermore we can study the convergence of these techniques when they are iterated many times.

We use a number of different measures to describe the performance of the linacs. Many observables are available at each BPM so that they can easily be studied as a function of longitudinal position s:

1. Horizontal and vertical beam and bunch positions with respect to the design plane or the BPM centers (by beam we refer to the average of the bunches).
2. Horizontal and vertical emittances for all bunches.
3. Horizontal and vertical luminosity reduction for all bunches.
4. Energy spread of the beam.
5. Beam energy.
6. Horizontal and vertical B_{mag} (see Equation 7.3) for a selected bunch.

At every marker point the beam distribution in phase space is available for a selected bunch and the whole bunch train. Twiss parameters are available for every beam line element. All observables, together with other parameters like misalignments, can be saved into external files which then are further analyzed. LIAR also provides screen summary output about single and multibunch emittance growth, rms trajectory offsets and the other observables.

7.6.2 Objectives

The NLC main linac simulations are undertaken with the general objectives to study the complex interactions between different parameters and to get a complete and coherent picture of the relevant emittance growth and optimization processes. By studying multiple error sources we try to evaluate the main linac performance under "realistic" conditions. Here we give a list of relevant simulation studies.

- Static quadrupole and BPM misalignments and errors (compare Sections 7.4.4 and 7.4.6):
  - Dispersive emittance growth as a function of transverse quadrupole and BPM misalignments.
  - Sensitivity to lattice mismatch from quadrupole strength errors.

  - Sensitivity to betatron coupling from quadrupole rolls.

- Static structure misalignments and errors (compare Sections 7.4.4 and 7.4.6):
  - Emittance growth due to random structure misalignments. Sensitivity to different wavelengths of misalignments.
  - Emittance growth due to systematic structure misalignments ("bowing", etc.).
  - Lattice mismatch from gradient and phase errors.
  - Sensitivity of dispersive emittance growth to changes in the BNS phases.

- Beam tails:
  - Determination of the average beam power that needs to be collimated.

- Beam line stability (compare Section 7.5):
  - Emittance growth from ATL-like drifts of the quadrupole and structure alignment.
  - Emittance growth from jitter and vibrations of the accelerator support.
  - Feedback requirements for effective trajectory stabilization.
  - Effects from bunch-to-bunch variations of charge or initial position and angle.

- Emittance control techniques (compare Section 7.5.2):
  - Efficiency of interleaved quadrupole steering and rf structure alignment in the presence of errors (compare Section 7.5.2).
  - Dispersion-free and wakefield-free steering.
  - Emittance optimization with trajectory bumps.

Several of these studies are interdependent and some need to be done for both single-bunch and multibunch cases. We cannot yet present all the final results. However, most of the problems mentioned above are addressed in the simulations that we are going to present.

7.6.3 Simulation Parameters

The NLC tolerances are tighter for the higher bunch currents and the longer bunch lengths at the higher beam energies. Therefore we restrict the simulations to the 500-GeV version of NLC-II. This is the case "NLC-IIb" in Tables 7-1 and 7-2. The beam consists of 90 bunches, where each bunch contains 1.1×10^{10} particles, is 150-μm long and has an initial uncorrelated energy spread of 1.5%. We describe a single bunch at 10 longitudinal positions each with 3 monoenergetic beam slices. The initial bunch shape is Gaussian. The initial horizontal and vertical beam emittances are $\gamma\epsilon_x = 4.0 \times 10^{-6}$ m-rad and $\gamma\epsilon_y = 4.0 \times 10^{-8}$ m-rad. The beam is accelerated to a final beam energy of 500 GeV.

The full NLC-IIb lattice is used for the simulations and we assume that the chicanes in the diagnostics stations are switched off. Beyond that we assume that multibunch beam loading is perfectly compensated. Parametrizations for short-range and long-range wakefields were provided from detailed calculations as mentioned in Sections 7.4.1 and 7.4.2. The simulations that are presented here focus on the vertical plane where the small initial emittance makes it much harder to avoid dilutions.

Config	ϕ_1 (°)	E_1 (GeV)	ϕ_2 (°)	E_2 (GeV)	ϕ_3 (°)
1	4	30	-7	485	-30
2	8	30	-5	455	-30
3	10	30	-3	425	-30
4	12	30	-1	400	-30
5	14	30	1	380	-30
6	16	30	3	360	-30
7	18	30	5	335	-30
8	20	30	7	320	-30
9	22	30	9	300	-30

Table 7-8. *BNS configurations: ϕ_1, ϕ_2 and ϕ_3 are the three rf phases in the linac and E_1 and E_2 are the switching points.*

7.6.4 BNS Configuration

As explained in Section 7.3.2, BNS damping significantly reduces the emittance growth in a linac. If the BNS autophasing condition is fulfilled then an incoming betatron oscillation will propagate downstream without perturbation. In this case, there will be minimal emittance growth. Figure 7-4 shows the autophasing energy spread for a simple two-particle model (compare Equation 7.2). The figure suggests an average autophasing energy spread of about 1.1%.

In order to identify an optimal BNS configuration we studied a number of energy spread profiles along the linac, each of which is generated by adjusting the rf phases in three groups. The BNS configurations number 1 to 9 are defined in Table 7-8. All BNS cases were calculated to give the required final beam energy spread of about 0.3% rms. In Figure 7-45 we show the beam energy spread along the linac for the different cases. Figure 7-46 characterizes the different BNS configurations in terms of average energy spread and the energy overhead required to generate them. The energy overhead is defined as the energy difference between operating with the nominal average rf phase and operating with the BNS phases. In the following we refer to the BNS cases by their BNS energy overhead.

To study the BNS configurations in terms of emittance preservation, we simulated the emittance growth for an initial 1σ vertical beam offset (2.2 μm). The initial uncorrelated beam energy spread was set to zero. As is shown in Figure 7-47 we find the smallest emittance growth for a BNS energy overhead of 1.3%. For lower energy overheads, wakefields cause large emittance growth while dispersive emittance growth dominates for higher BNS energy spreads. Since the BNS overhead of 1.3% is well inside the specifications (up to 3%), we chose the BNS configuration number 3 for all further studies. However, we always made sure that this BNS case is a good working point. Later we will discuss our choice of BNS energy spread for two other emittance growth problems and we will see that the BNS configuration number 3 is still the optimal working point within the cases that are considered. We note that the rms energy spread for this BNS configuration is about half of what is expected for autophasing from Figure 7-4.

If the autophasing condition is fulfilled, then we would expect that the betatron oscillations from the initial 1σ beam offset, normalized with the beta function and the beam energy, propagate downstream without perturbations. Figures 7-48 and 7-49 show the normalized betatron oscillations and the vertical single bunch emittance growth along the linac. The first figure does not include any initial uncorrelated energy spread, while the second case includes the nominal 1.5% initial energy spread. It is easily seen that the amplitude of the normalized betatron oscillation is not maintained in either case. We note that the initial uncorrelated beam energy spread significantly changes the dynamics in the beginning of the linac. It causes strong filamentation and modifies tolerances for incoming jitter.

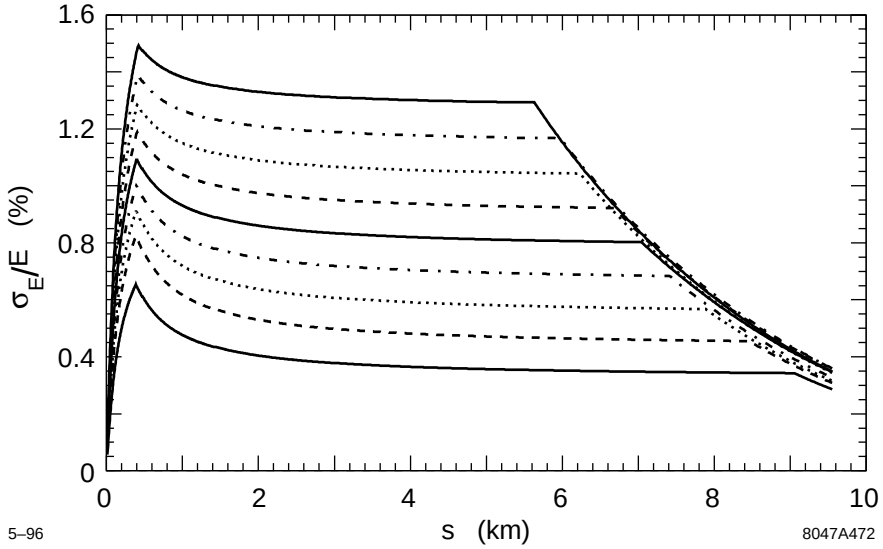

Figure 7-45. *Beam rms energy spread along the linac for different BNS configurations. Note that the initial uncorrelated energy spread was set to zero. The final extracted rms energy spread is fixed to about 0.3% as required by the final focus energy bandwidth. The different BNS configurations are defined in Table 7-8 and are referred to as number 1 to 9, where 1 is the lowest curve.*

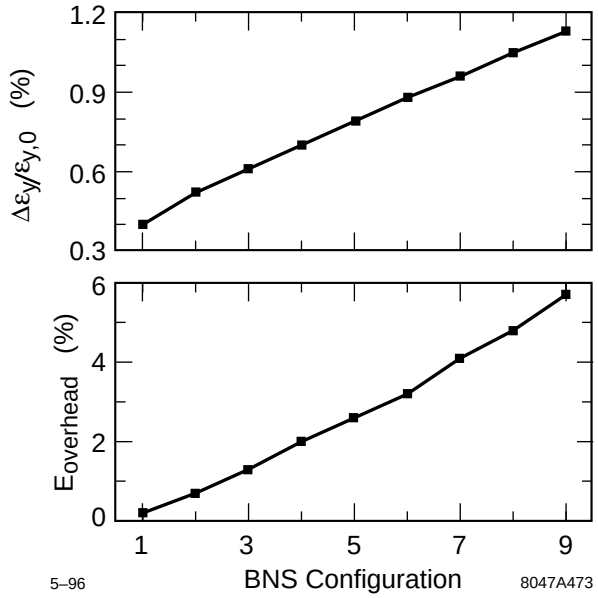

Figure 7-46. *The different BNS configurations from Figure 7-45 are characterized by the average energy spread σ_E / E along the linac and the BNS energy overhead E_{overhead}.*

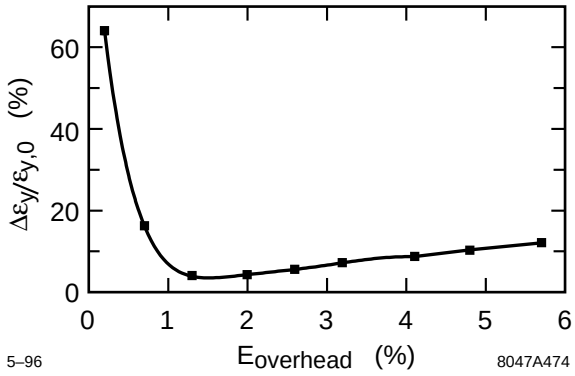

Figure 7-47. *Average vertical emittance growth $\Delta\epsilon_y/\epsilon_{y,0}$ for the different BNS configurations from Figures 7-45 and 7-46 and a 1σ (2.2 μm) initial beam offset. The initial uncorrelated beam energy spread is set to zero.*

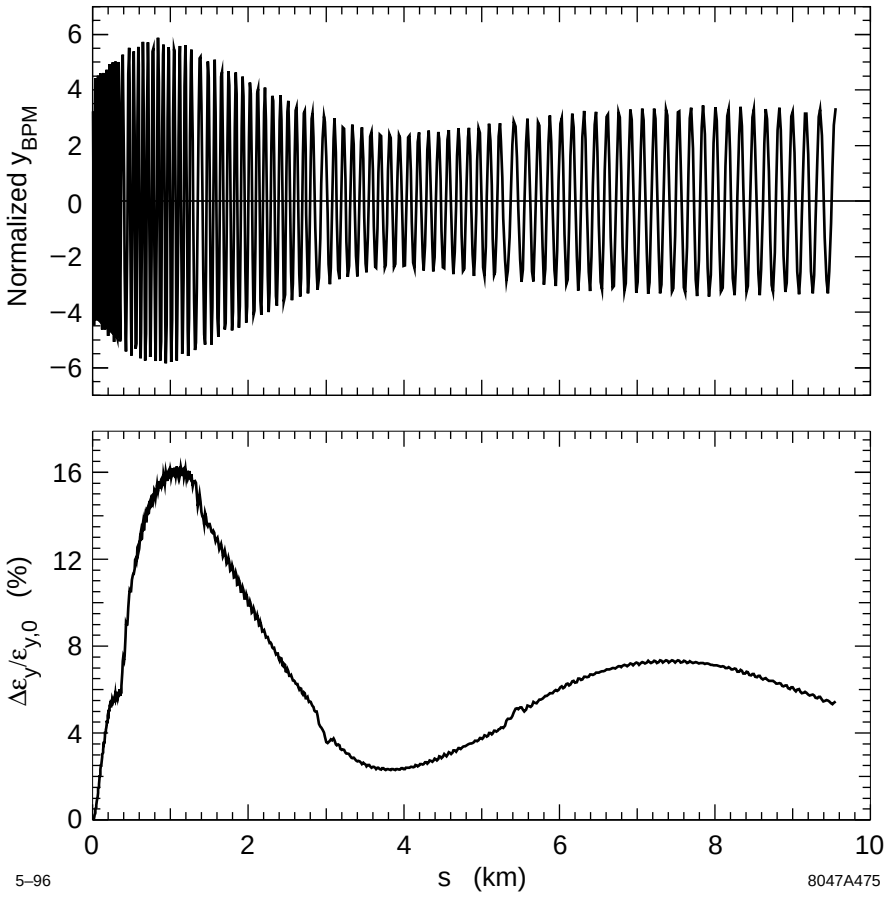

Figure 7-48. *Beam offsets y_{BPM}, normalized with the beta function and the beam energy, and emittance growth $\Delta\epsilon_y/\epsilon_{y,0}$ for a 1σ (2.2 μm) initial beam offset and no initial uncorrelated beam energy spread. The BNS configuration number 3 with a BNS energy overhead of 1.3% is used.*

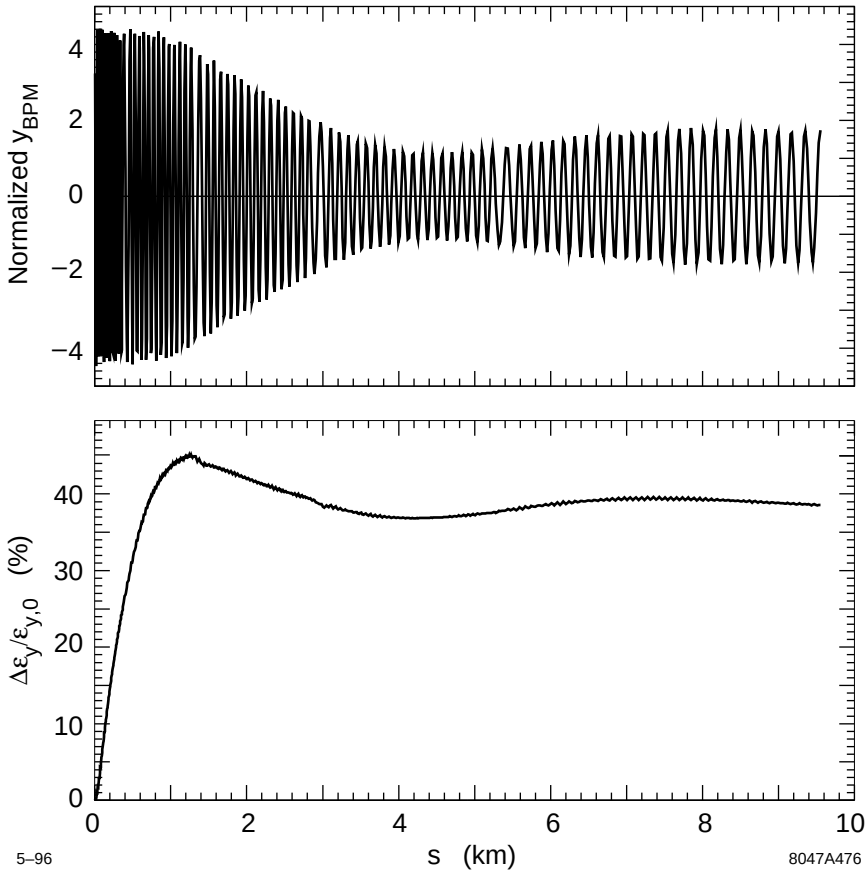

Figure 7-49. *Beam offsets y_{BPM}, normalized with the beta function and the beam energy, and emittance growth $\Delta\epsilon_y/\epsilon_{y,0}$ for a 1σ (2.2 μm) initial beam offset. Here the initial uncorrelated beam energy spread is set to 1.5%. Again we use the BNS configuration number 3 with a BNS energy overhead of 1.3%.*

7.6.5 Static Imperfections and Their Correction

Imperfections are called static if they do not change during the typical timescale of beam-based alignment and correction procedures. Initially static imperfections in the NLC linacs are allowed to be large compared to the final tolerances. In order to achieve the required tolerances the "conventional" (not beam-based) alignment must be complemented by beam-based alignment techniques. In this section we explain the algorithm proposed for beam-based alignment and its implementation in the simulation program. We discuss detailed simulations that show that the required precision levels can indeed be achieved, even when many additional error sources are included.

The Beam-based Alignment Algorithm for Quadrupoles and RF-structures

The emittance growth is driven by transverse offsets between the beam and the centers of quadrupoles and structures. Those offsets must be effectively minimized in order to maintain the normalized emittances.

The basic concept for the NLC beam-based quadrupole alignment is to use the available BPM information to solve for the beam-to-quadrupole offsets and the initial beam position and angle. Assuming that all beam deflections are caused by the quadrupoles, we can use N BPM measurements to solve for $N-2$ quadrupole offsets and the initial y, y' of the beam. The positions of the first and last quadrupole in the corrected section are fixed. The endpoint BPMs define the reference line for the alignment. If the alignment is done in many sections then the beam is launched from one section into the other with a single dipole corrector at the border between the two. Therefore, for all but the first section we adjust only the initial y'. In the first section we adjust both y and y' of the incoming beam ("launch feedback"). The quadrupoles are aligned with magnet movers at each quadrupole support. Since the optics model is perturbed by wakefields and to account for other imperfections, the alignment is implemented as an iterative process. Furthermore, the quadrupole alignment is interleaved with the alignment of the rf-structures.

The rf accelerator structures have an rf-BPM at each end. Two rf-structures are always mounted on a single support structure. Every support structure can be moved by stepping motors at either end. Thus, for each support structure a total of four rf-BPMs measure the beam positions in the structures and two movers align the girder. The movers are adjusted such that the average rf-BPM reading on a girder is minimized. The rf-structure alignment is performed after each iteration of quadrupole beam-based alignment.

Here, we assume that the step resolution of the magnet and girder movers is infinitely small. The typical step size of 0.25 μm is indeed small compared to the resolution of the rf-BPMs of about 15-μm rms and can therefore be neglected for the rf-structures. However, for quadrupoles the step size of the movers is an important limitation. The problem is avoided by having dipole correctors at each quadrupole that shift its effective magnetic center. Small quadrupole misalignments are therefore "cured" with dipole correctors. If the dipole strengths get large enough they are "exchanged" for a step of the quadrupole mover.

The alignment algorithm that was sketched above was implemented into the simulation program LIAR. First, we consider a simple case where we start with a random quadrupole misalignment of 100-μm rms and assume perfect BPMs and rf-BPMs. Both kinds of BPMs have no offsets and zero resolution. The quadrupole alignment is done in 14 regions to allow for best convergence. Each region contains about 52 quadrupoles and is iterated 15 times. The number of iterations is chosen higher than necessary in order to explore the optimal solution.

The misalignment of quadrupoles, BPMs and rf structures, after the application of the interleaved alignment procedure, is shown in the upper part of Figure 7-50. The dipole kicks at the boundaries between correction regions are shown in the lower part of the same figure. A very smooth alignment between the endpoints of each section is indeed achieved. At the endpoints the beam is deflected into the next section, causing sharp kinks. The endpoints are not moved and reflect the initial random quadrupole misalignment of 100 μm. Between the endpoints, the alignment is bowed towards zero. The absolute zero line is known to the system only because the initial misalignment was random about it. Constraints on the rms size of magnet movements bias the solution towards the initial average misalignment between endpoints.

The solution shown in Figure 7-50 is largely determined by the different weights on the "measured" BPM readings, the rms of the calculated magnet movements and the strength of the dipole kick that launches the beam into the alignment section. Changes in the relative weights will result in solutions that are not equivalent in terms of emittance growth. We have chosen to constrain the rms magnet movements and the rms of the "measured" BPM readings relatively strongly while allowing for large dipole kicks. This choice of weights results in a small final emittance growth.

The vertical single-bunch emittance growth and the trajectory along the linac are shown in Figures 7-51 and 7-52. The trajectory in Figures 7-52 shows residual sub-micron beam offsets in the quadrupoles that result from the "bowing" of the alignment trajectory. Figure 7-51 shows that these small beam offsets cause no significant emittance growth. The residual emittance growth occurs mainly at the transitions from one sector to the next. The large dispersive deflections cause a stepwise emittance growth behavior. One can imagine smoothing the transitions by distributing the beam

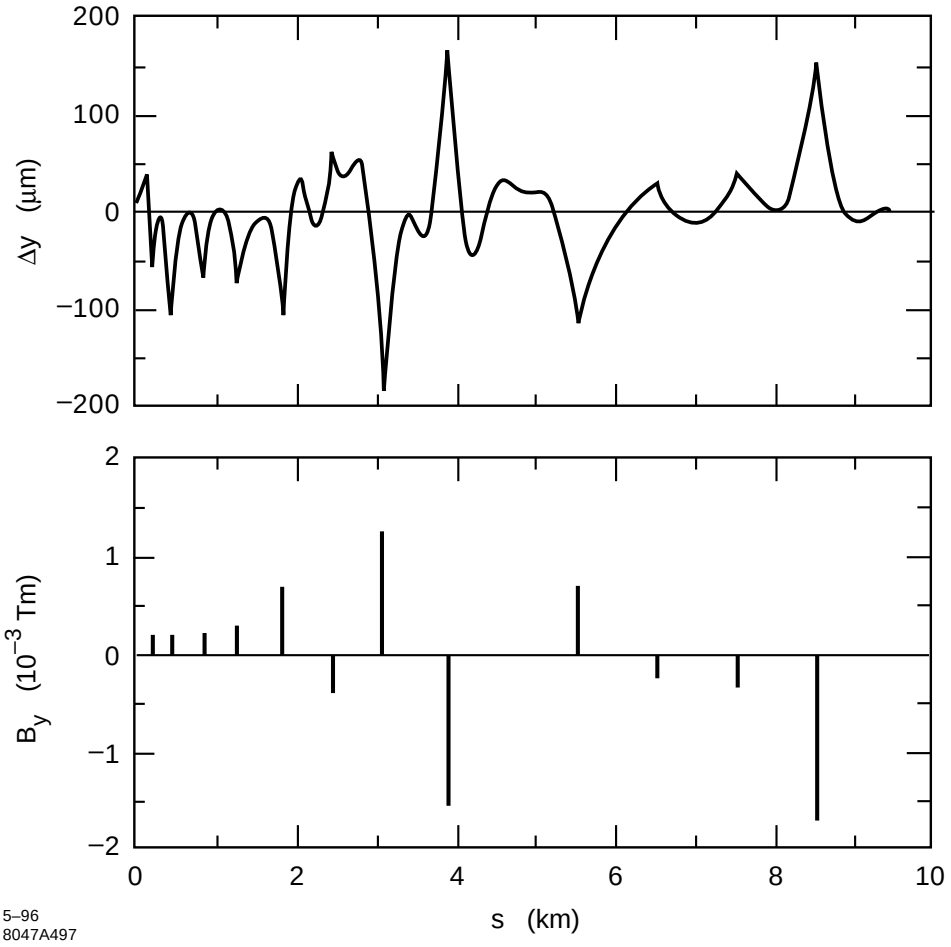

Figure 7-50. *Example of the beam-based alignment algorithm with perfect BPMs and rf-BPMs. The initial random quadrupole misalignment was 100-μm rms. The alignment is done in 14 sections and 15 iterations. At the end of each section a dipole corrector is used to launch the beam into the next section. The upper plot shows the misalignment Δy of quadrupoles, rf-structures and BPMs after alignment. The lower plot shows the integrated fields of the dipole correctors.*

deflection. A better method would be to also move the sector endpoint quadrupoles such that the deflection kicks are minimized.

We should stress that the present algorithm already works very well. The quadrupole and structure alignment is minimized over short wavelengths and beam offsets with respect to the BPMs are effectively reduced from many cm's to the sub-micron level. The smooth alignment of quadrupoles and structures minimizes the vertical emittance growth to about 20%. The convergence of the method is illustrated in Figure 7-53 where the vertical single-bunch emittance growth and the vertical rms beam offset in the BPMs are shown as a function of iteration number. It is seen that after about 5 iterations a very reasonable situation is achieved with almost no further improvements after about 15 iterations.

The emittance growth for the case of perfect BPMs is a function of the initial quadrupole misalignment which determines the magnitude of the dispersive deflections between sections. This is shown in Figure 7-54. The vertical single-bunch emittance growth and the rms trajectory offset at the BPMs are shown as a function of the initial rms

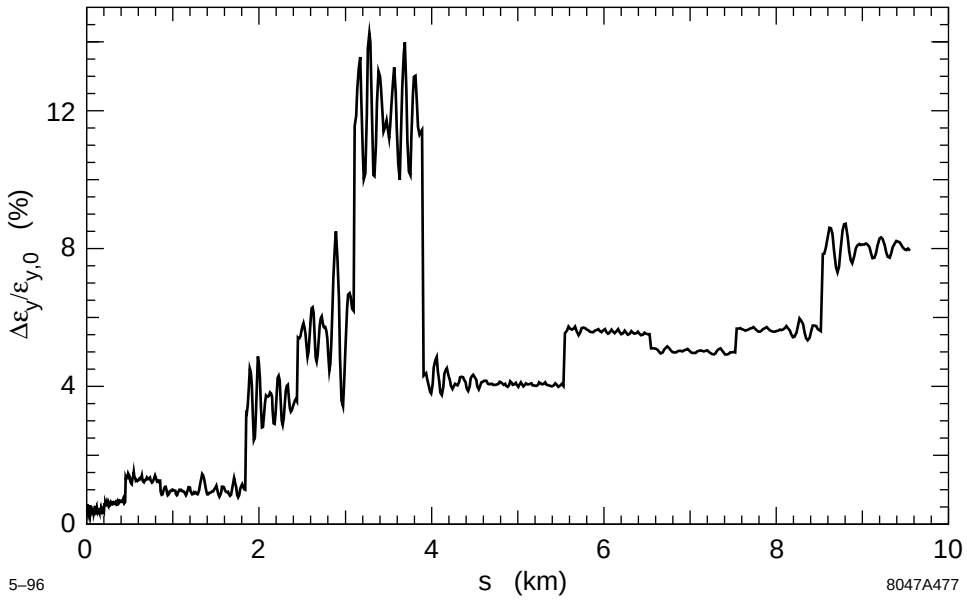

Figure 7-51. *Emittance growth $\Delta\epsilon_y/\epsilon_{y,0}$ along the linac for the example from Figure 7-50. Note that the steps occur at the end of the alignment sections where dipole kicks launch the beam into the next section.*

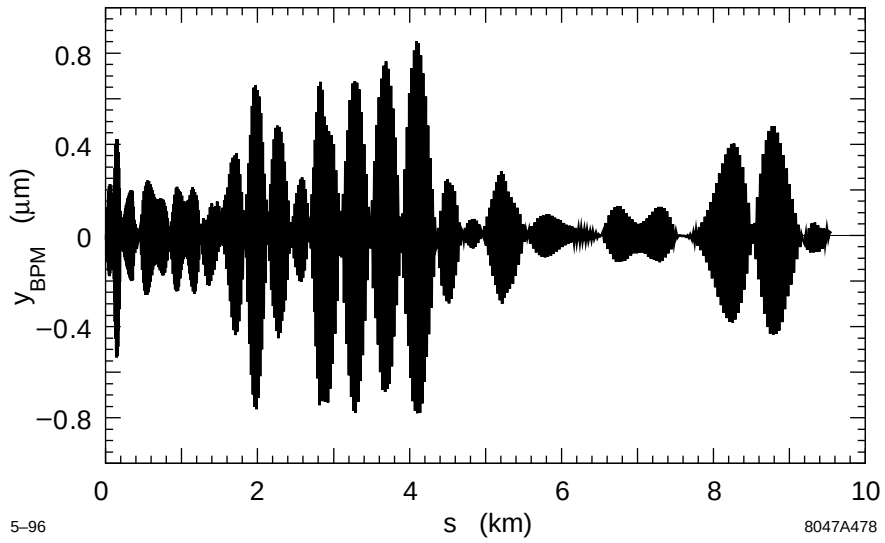

Figure 7-52. *Vertical trajectory offsets at the quadrupole BPMs along the linac for the example from Figure 7-50. The residual beam offsets in the quadrupoles bend the beam along the "bowed" beam line after alignment. They are not betatron oscillations and cause only negligible emittance growth (compare to Figure 7-51).*

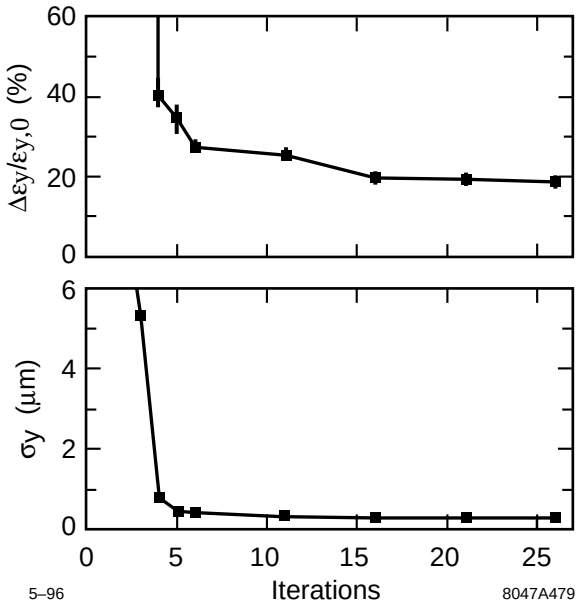

Figure 7-53. *Convergence of the alignment algorithm for an initial random quadrupole misalignment of 100-μm rms and perfect BPMs. The upper plot shows the average emittance growth $\Delta\epsilon_y/\epsilon_{y,0}$ as a function of the iteration number. The lower plot shows the corresponding rms trajectory offset with respect to the BPMs.*

quadrupole offset. As expected, the rms trajectory offset in Figure 7-54 increases linearly and the vertical emittance growth increases quadratically with the initial rms quadrupole misalignment.

Now we consider a more realistic case where the BPMs have a 2-μm-rms static offset with respect to the quadrupoles and a 1-μm-rms resolution. The initial quadrupole misalignment is 50-μm rms. We still assume perfect rf-BPMs. The alignment is done in 14 sections and 5 iterations. Figure 7-55 shows the average vertical single-bunch emittance growth for the different BNS cases and the imperfections defined above. The BNS configuration number 3 still yields the smallest emittance growth. However, due to the additional BPM imperfections, the emittance growth for the nominal BNS increased from about 7% to about 28%. This is well below the emittance growth budget of 175% for NLC-IIb.

The Effects of Transverse Long-range Wakefields

Thus far, we have only considered single-bunch effects. However, for the bunch train of 90 bunches, transverse long-range wakefields become important. In order to set the scale of those effects, we show the multibunch emittance blowup due to a 1-sigma initial vertical beam offset. Figure 7-56 shows the special case where each bunch is described as a single beam ellipse (zero bunch length). Single-bunch wakefields do not apply and the phase space distribution of the bunch train only reflects long-range wakefields. The phase space distribution of the bunches is compared to the beam ellipse that is obtained from the average single-bunch emittance. The bunches spread all over the beam ellipse but do not reach far beyond that. Multibunch emittance growth is therefore small and is found to be 25.6%.

Figure 7-57 shows the same case for a more realistic beam distribution. The bunch has a finite length and single bunch wakefields apply. Filamentation and BNS damping cause the phase space distribution of the bunches to be smaller. In this case the emittance of the first bunch grows by 38.7%, the average single-bunch emittance growth is 49.0% and the

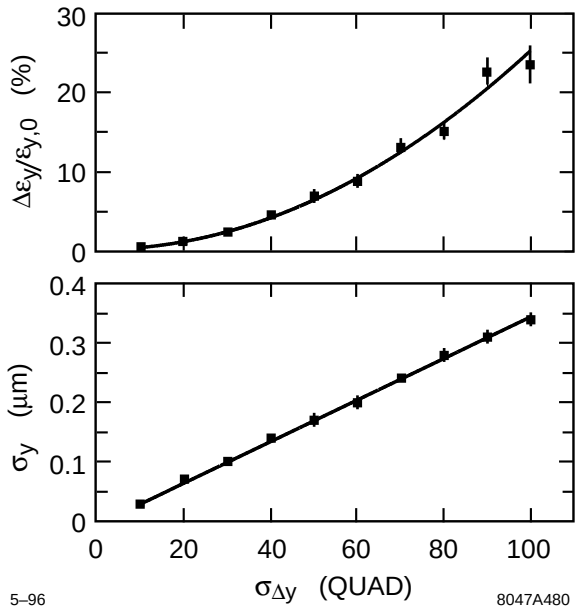

Figure 7-54. *The average emittance growth $\Delta\epsilon_y/\epsilon_{y,0}$ and rms trajectory offset σ_y after alignment versus the initial rms quadrupole misalignment $\sigma_{\Delta y}$.*

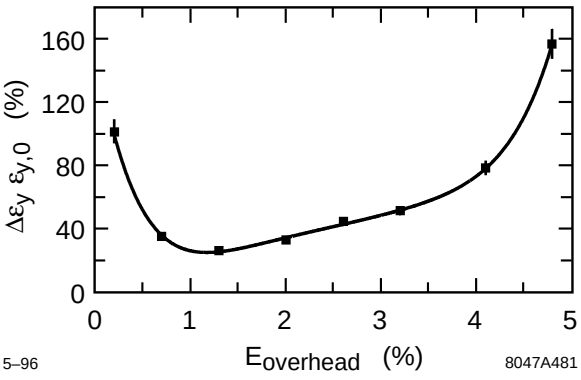

Figure 7-55. *Average emittance growth $\Delta\epsilon_y/\epsilon_{y,0}$ after alignment for different BNS configurations. Here we assume an initial quadrupole alignment of 50-μm rms, a static BPM to quadrupole offset of 2-μm rms, a BPM-resolution of 1-μm rms and perfect rf-BPMs. The alignment is done in 14 sections and 5 iterations.*

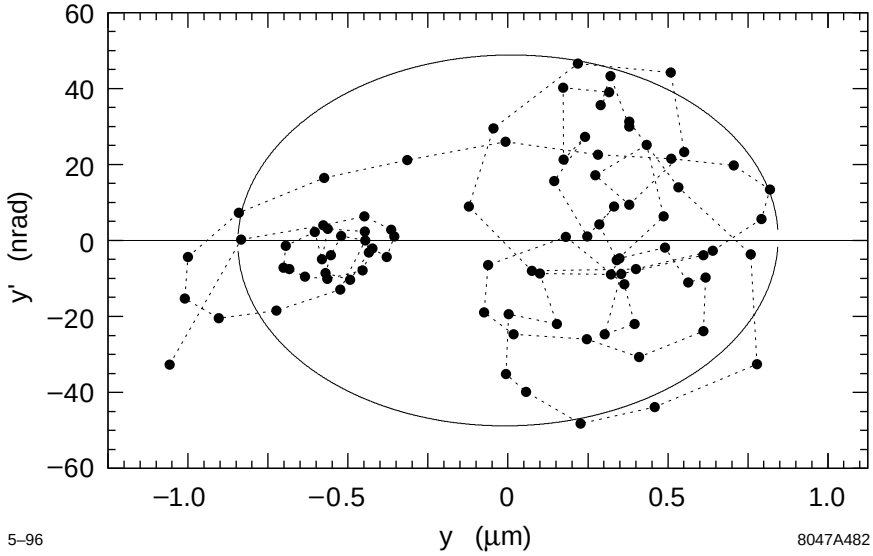

Figure 7-56. *Phase space locations y and y' of the bunches at the end of the linac for a 1-sigma initial vertical beam offset. y and y' are referenced to their average values. The bunch positions are compared to the beam ellipse from the average single-bunch emittance. Every bunch is tracked as a single beam ellipse so that no single-bunch wakefield effects apply. For this case a multibunch emittance growth of 25.6% was calculated.*

total emittance growth is 54.4%. The difference between the last two numbers reflects the impact of the long-range transverse wakefields. Here emittance growth is dominated by single-bunch wakefield effects.

Betatron Coupling

In the NLC, the horizontal emittance is about 100 times larger than the vertical emittance. Betatron coupling can couple part of the large horizontal emittance into the vertical plane. This effect is illustrated in Figure 7-58. Since the horizontal trajectory was kept flat for this study, no vertical betatron oscillations are induced from the coupling. If there were any, they would be absorbed into the alignment and trajectory correction. The emittance growth shows a quadratic dependence on the rms quadrupole roll angle. Assuming the tolerance value of the roll angle of about 300 μrad rms, the emittance growth is well below 10% and is not important.

7.6.6 Full Simulation

For a full simulation, we put the most important imperfections together, apply the correction algorithms and observe the emittance growth. In order to illustrate the importance of the several effects, we proceed in steps. For each case we quote the emittance growth $\Delta\epsilon_y/\epsilon_{y,0}$ at the end of the linac and the rms beam offset σ_y at the BPMs.

1. Initial random quadrupole misalignment of 100-μm rms. Rf structures are aligned to the beam.

$$\frac{\Delta\epsilon_y}{\epsilon_{y,0}} = (24.4 \pm 2.3)\% \tag{7.8}$$

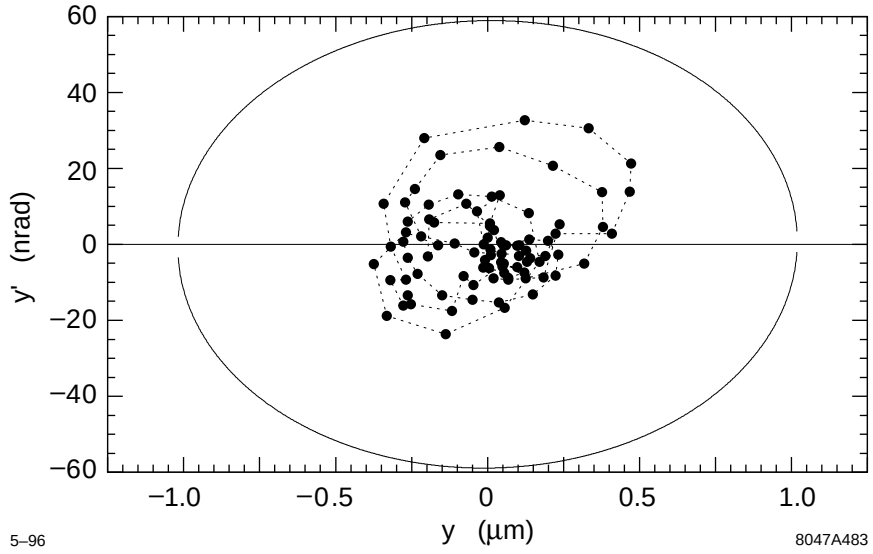

Figure 7-57. *Phase space locations y and y' of the bunches at the end of the linac for a 1-sigma initial vertical beam offset. y and y' are referenced to their average values. Single-bunch wakefield effects are included. The amplitude of the incoming betatron oscillation and the resulting long-range wakefield effects are reduced by filamentation. The bunch positions are compared to the beam ellipse from the average single-bunch emittance. Here we obtain a total emittance growth of 54.4%. The emittance growth of the first bunch is 38.7% and the average single-bunch emittance growth is 49.0%.*

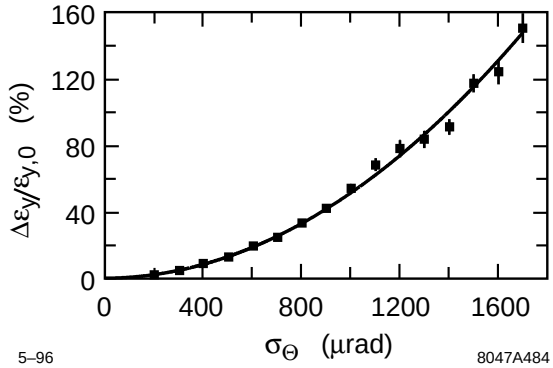

Figure 7-58. *Average vertical emittance growth $\Delta\epsilon_y/\epsilon_{y,0}$ as a function of the rms quadrupole roll θ around the longitudinal direction. There are no horizontal beam offsets in the quadrupoles. The data only shows "emittance coupling".*

$$\sigma_y = (0.35 \pm 0.01)\ \mu\text{m} \tag{7.9}$$

2. Add: BPM resolution of 1-μm rms. Static BPM-to-quadrupole offsets of 2-μm rms.

$$\frac{\Delta\epsilon_y}{\epsilon_{y,0}} = (41.1 \pm 2.4)\% \tag{7.10}$$

$$\sigma_y = (1.08 \pm 0.01)\ \mu\text{m} \tag{7.11}$$

3. Add: rf-BPM resolution of 15-μm rms.

$$\frac{\Delta\epsilon_y}{\epsilon_{y,0}} = (90.2 \pm 6.0)\% \tag{7.12}$$

$$\sigma_y = (1.21 \pm 0.01)\ \mu\text{m} \tag{7.13}$$

4. Add: Rf-phase errors of 1° rms. Rf amplitude errors of 0.2% rms. Quadrupole roll errors of 300-μr rms. Quadrupole gradient errors of 0.3% rms.

$$\frac{\Delta\epsilon_y}{\epsilon_{y,0}} = (97.8 \pm 3.6)\% \tag{7.14}$$

$$\sigma_y = (1.22 \pm 0.01)\ \mu\text{m} \tag{7.15}$$

5. Add: Multibunch long-range wakefield effects.

$$\frac{\Delta\epsilon_y}{\epsilon_{y,0}} = (106.6 \pm 3.9)\% \tag{7.16}$$

$$\sigma_y = (1.23 \pm 0.01)\ \mu\text{m} \tag{7.17}$$

All emittance growth numbers, apart from the last one, refer to the single-bunch emittance growth. The total multi-bunch emittance growth of about 110% is well below the allowed emittance dilution of 175% for NLC-IIb (compare Table 7-2). Internal structure misalignments, special multibunch imperfections and the effects of missing BPMs will be added to the simulations in future studies.

The most important imperfections considered so far are BPM and rf-BPM errors. They determine the quality of the correction and the residual emittance growth. In all cases, the correction and alignment is done on the first bunch, assuming that all other bunches behave similarly. The small additional multibunch emittance growth shows that this is a valid assumption, although we have not yet included the effects of internal structure misalignments. The distribution of emittance growth for different error distributions is shown in Figure 7-59 for the full simulation (last case). The exponential tail for large emittance dilutions tends to bias the average emittance growth towards larger values. It results from error distributions that have a large component at the betatron frequency. Fortunately, these errors are easily corrected using bump (global) correction methods.

Figure 7-60 shows an alternate way to quantify the effect of imperfections. The so-called "luminosity reduction" (L_y) is calculated from a cross-correlation of the bunch distributions with themselves. Beam tails are naturally de-weighted in this process. The result is quoted as the fraction of the maximum luminosity that would be achieved for the particular case. The luminosity reduction comes out to be 71.1% for the full NLC simulation. That means that on average about 70% of the maximum luminosity would be obtained with the given errors.

Figure 7-61 shows the average emittance growth along the linac for 100 seeds of the full simulation. The growth shows a square-root dependence on the longitudinal position s. No particularly bad region can be identified and the emittance

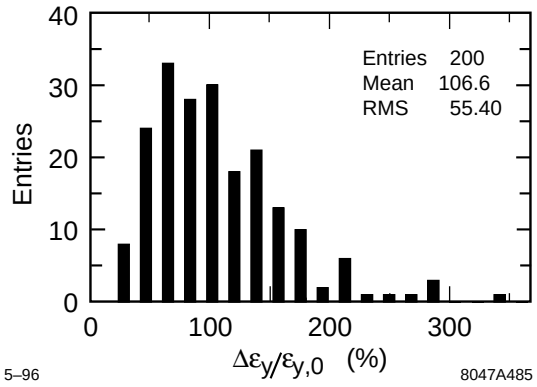

Figure 7-59. *Histogram of vertical emittance growth $\Delta\epsilon_y/\epsilon_{y,0}$ for 200 different error distributions. The average emittance growth is 106.6% ± 3.9%. Note the exponential distribution for large emittance dilutions.*

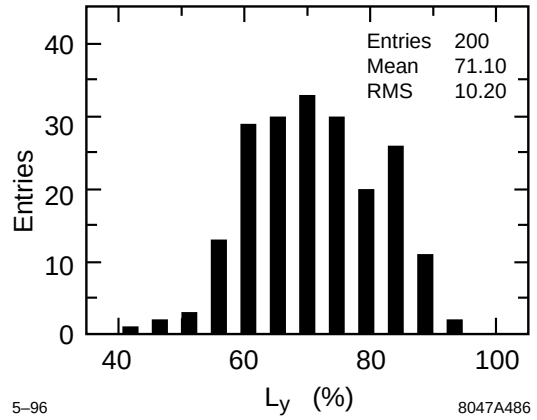

Figure 7-60. *Histogram of the luminosity reduction L_y for 200 different error distributions. The average luminosity factor is 71.1% ± 0.7%.*

growth behaves rather smoothly. Small residual step increases of the emittance can be seen. They are caused by the transitions between alignment sections. However, they are of little importance to the overall emittance growth.

Figures 7-62, 7-63 and 7-64 show an example of the long-range wakefield effects for the full set of imperfections. Figure 7-64 is of particular interest. The single-bunch emittance is shown as a function of the bunch number. It shows an oscillatory behavior and is even reduced below the value of the first bunch for some of the trailing bunches. Long-range wakefields induce bunch oscillations that can work as "emittance bumps" and reduce emittance. If one could measure the emittances and trajectories of all bunches one could pick the bunch with the smallest emittance and use multibunch kickers to correct the other bunches to this reference. The multibunch scheme can in principal be used to conveniently explore the phase space to find the smallest possible emittance dilution.

7.6.7 Stability

Stability questions determine how often the alignment and correction algorithms need to be applied. In the previous section we described a procedure that serves as both the alignment and trajectory correction algorithm. We have shown

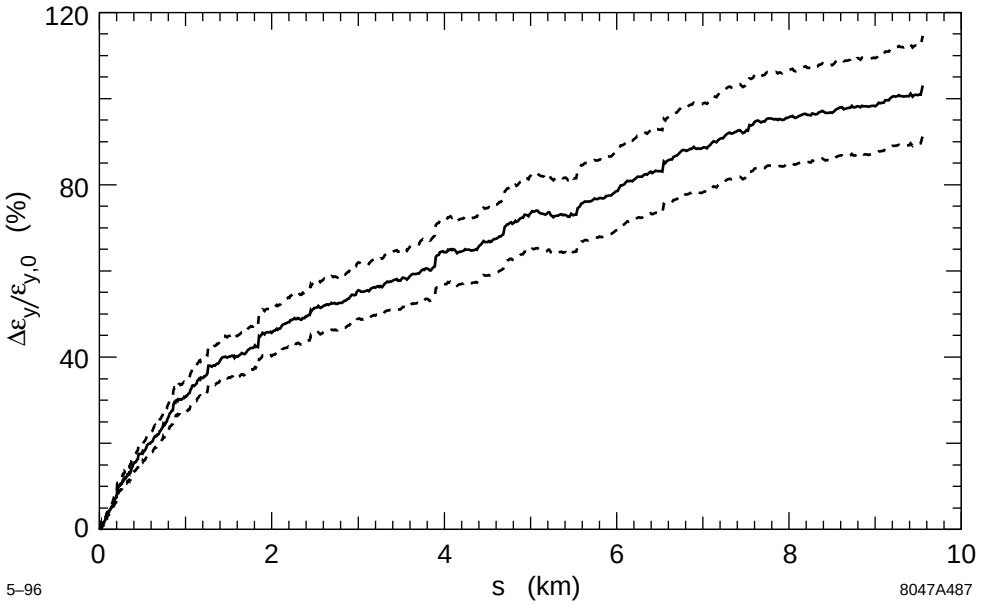

Figure 7-61. *Average emittance growth $\Delta\epsilon_y/\epsilon_{y,0}$ along the linac for the full simulation. The dashed curves specify the error bars around the average (solid curve).*

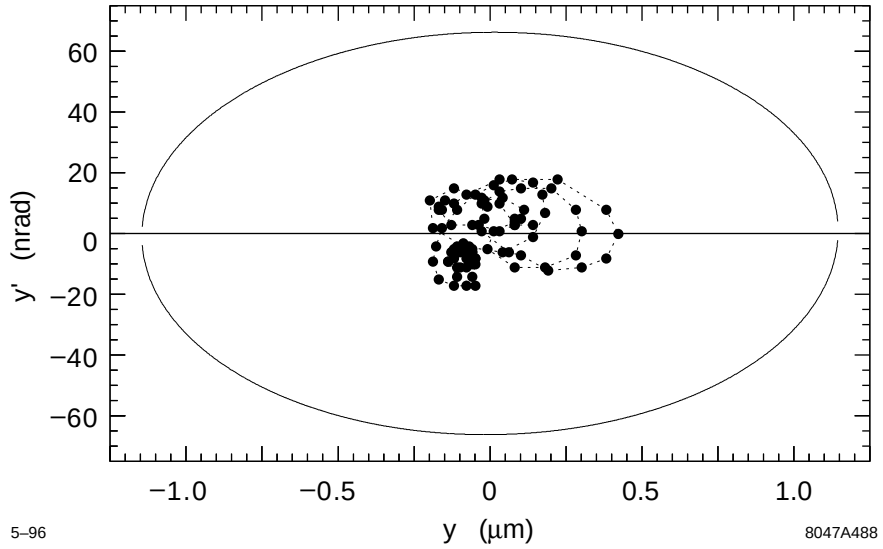

Figure 7-62. *Example of the vertical phase space distribution of the bunch train at the end of the linac. The bunch locations are compared to the beam ellipse as obtained from the average single-bunch emittance. The total vertical emittance growth is 89.0% for this case. This is to be compared to an emittance growth of the first bunch of 83.0%, and an average single-bunch emittance growth of 85.2%.*

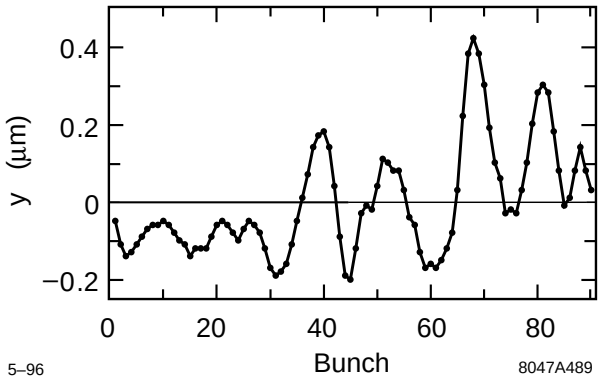

Figure 7-63. *Vertical bunch positions y as a function of bunch number at the end of the linac (same example as in Figure 7-62).*

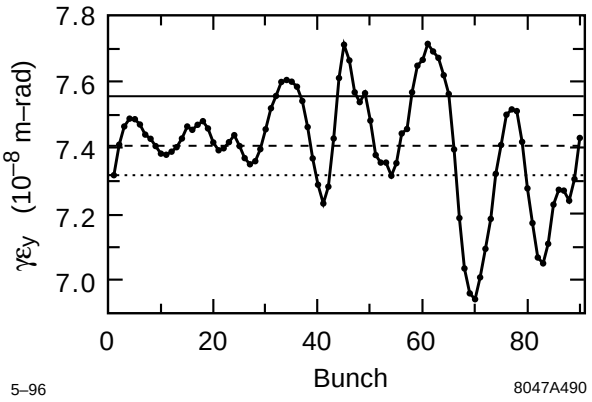

Figure 7-64. *Vertical normalized single-bunch emittance ϵ_y as a function of bunch number at the end of the linac (same example as in Figures 7-62 and 7-63). The three lines indicate the emittance growth of the first bunch (dotted), the average single-bunch emittance growth (dashed) and the total beam emittance growth (solid).*

that static imperfections can be corrected down to the required levels. Now we consider the question of how stable the optimized linac is and how fast it deteriorates. From the beam dynamics point of view, linac stability problems are dominated by quadrupole drifts; the quadrupoles generally have the tightest alignment tolerances.

Here we do not discuss BPM stability questions in detail. However, the requirements are tight. For the alignment algorithm we require a 2-μm static rms offset between the BPM and quadrupole centers. This tolerance can be achieved with a time-consuming beam-based alignment procedure and it must be stable over significant periods of time (days). The question of BPM stability is discussed elsewhere. Since quadrupoles and BPMs are mechanically mounted together, the BPM stability that can be achieved is mainly determined by the BPM electronics, cable lengths and similar factors.

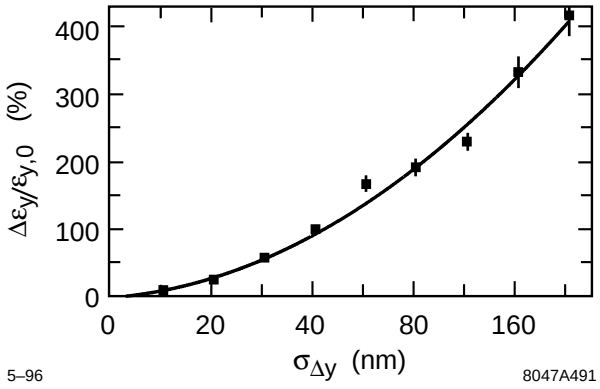

Figure 7-65. *Average single-bunch emittance growth $\Delta\epsilon_y/\epsilon_{y,0}$ as a function of the rms quadrupole offset Δy.*

Quadrupole Vibrations

Vibrations are fast random motions of the quadrupole alignment around its average position. Here we assume that the vibrations are white noise and that they are not damped by trajectory feedbacks. In reality the quadrupole vibrations due to ground motion, cooling water turbulence, etc will depend on frequency and will be partly suppressed by the trajectory feedbacks.

The average vertical emittance growth is shown in Figure 7-65 as a function of the vertical rms quadrupole offset $\sigma_{\Delta y}$. Here we only consider single-bunch emittance growth with respect to the beam centroid. Offsets that make the beams miss at the IP are assumed to be suppressed by fast feedbacks. Those effects are discussed in more detail in Section 7.4 and in the final focus chapter. From Figure 7-65 we see that the quadrupole white noise jitter should be kept below 20 nm in order to avoid single-bunch emittance growth in excess of 10%; this tolerance is well above the measured quadrupole jitter. Note that a tighter tolerance results if one considers the emittance growth with respect to the beam axis.

The emittance growth for quadrupole jitter is mainly caused by the uncorrected betatron oscillation that builds up along the linac. This will be discussed in the next section.

ATL-like Alignment Drifts

Next, we consider the question of how often the alignment and correction algorithm needs to be applied. Assuming a perfect starting point (flat trajectory, no emittance growth) we let the alignment drift and observe the deterioration of the trajectory and the emittance. In order to model alignment drifts we use the ATL-model. The ATL-model predicts that the rms vertical misalignment $\sigma_{\Delta y}$ (in μm) deteriorates with time T (in seconds) and over the length L (in m) as follows:

$$\sigma_{\Delta y}^2 = A \cdot T \cdot L \tag{7.18}$$

We use an A coefficient of 5×10^{-7} μm^2/s/m. This value was inferred from data taken on the SLAC site for times T over 30 hours. We should caution that the validity of the ATL-model (diffusive drifts) is not well established. Recent observations indicate a linear increase of the rms misalignment with time for longer periods (systematic drifts). Assuming diffusive alignment drifts from the ATL-model for time periods of the order of hours might well be overly pessimistic.

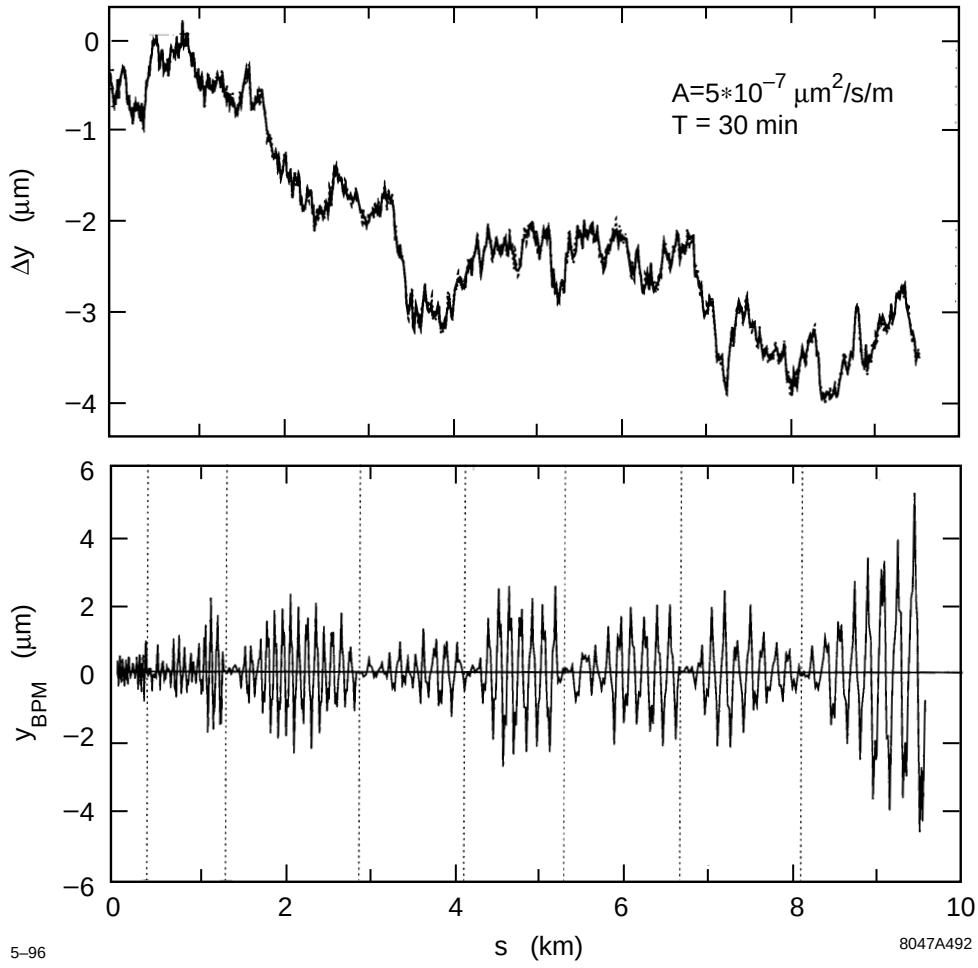

Figure 7-66. *Example of ATL-like alignment drifts. The upper plot shows the displacements of quadrupoles, rf-structures and BPMs after 30 minutes with an A-coefficient of* 5×10^{-7} μm^2*/s/m. The alignment was flat initially. The lower plot shows the corresponding trajectory offsets* y_{BPM} *at the BPMs. The dotted lines indicate the locations of trajectory feedbacks where* y *and* y' *are corrected back to zero. Thus the size of coherent betatron oscillations is constrained.*

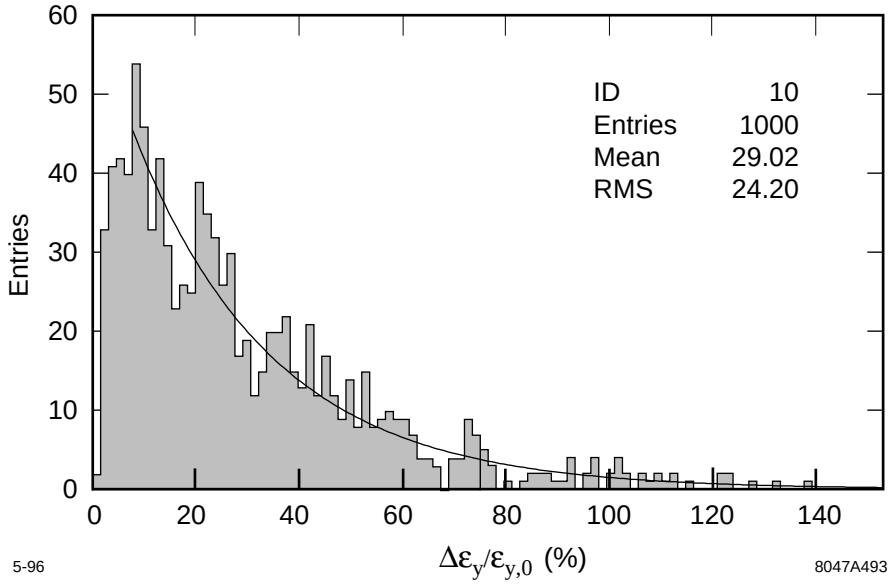

Figure 7-67. *Histogram of vertical emittance growth $\Delta\epsilon_y/\epsilon_{y,0}$ for 1000 different error distributions. The average emittance growth is 29.0% ± 0.8%. The solid curve shows an exponential fit for large emittance dilutions.*

Figure 7-66 illustrates ATL-like alignment drifts. It shows the displacements and corresponding trajectory offsets at the BPMs after 30 minutes of deterioration. The offsets of quadrupoles, BPMs and rf-structures are overlaid in the plot and are essentially indistinguishable. The trajectory offsets at the BPMs show the coherent betatron oscillations that build up. The dotted lines indicate the locations of seven trajectory feedbacks that constrain y and y' to zero. The coherent betatron oscillations are thus broken up into eight smaller oscillations. The oscillation amplitude is a few μm and is large enough to be detected with a BPM resolution of 1 μm.

A histogram of the vertical single-bunch emittance growth from alignment drifts after 30 minutes and an A of 5×10^{-7} μm^2/s/m is shown in Figure 7-67. The average emittance growth is found to be 29.0% ± 0.8%. This size of emittance growth will prompt a beam-based alignment of the quadrupoles, that serves as an effective trajectory correction at the same time. Note, however, the exponential distribution for large emittance dilutions. The most probable emittance growth is only about 10%. Figure 7-68 shows a histogram for the luminosity reduction in the same case. The distribution shows an approximately Gaussian distribution for smaller luminosity, with an average luminosity of about 90% of its ideal value.

The average emittance growth along the linac is shown in Figure 7-69. The locations of the trajectory feedbacks are clearly seen. As a coherent betatron oscillation builds up the emittance starts to grow exponentially. The feedbacks stop this exponential growth. More effective feedbacks can be imagined if the average y and y' is minimized up to the next feedback instead of correcting y and y' locally.

Figure 7-70 shows the average vertical single-bunch emittance growth for different BNS configurations. We consider the same case as above. All previous results were obtained using the standard BNS configuration with an energy overhead of 1.3%. Figure 7-70 shows that BNS configurations with higher energy overheads reduce the emittance growth from 29% to about 16%. This result is in better agreement with the simple two-particle model autophasing condition than the other results that were discussed before. One can therefore imagine to trade alignment performance against better stability. However, this is not necessary.

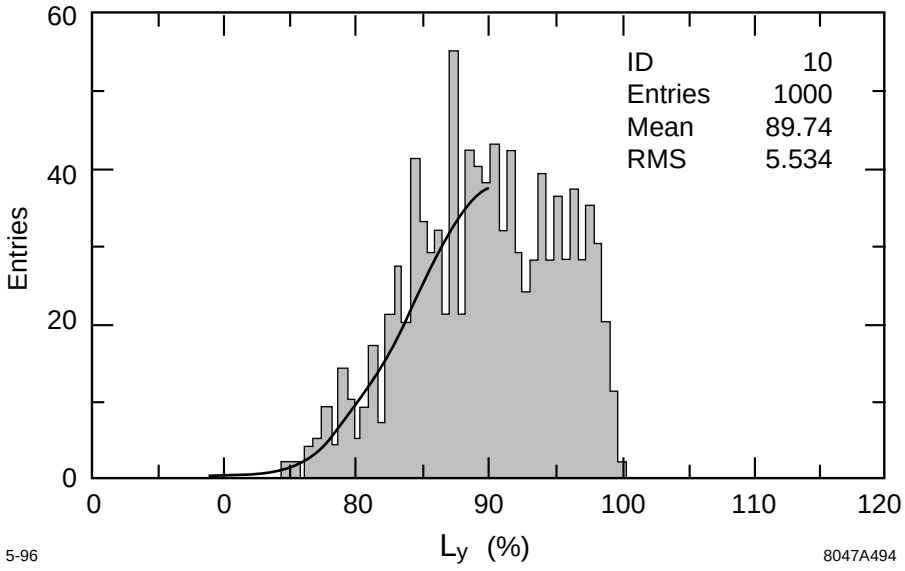

Figure 7-68. *Histogram of the luminosity factor L_y for 1000 different error distributions. The average luminosity is 89.7% $\pm$ 0.2%. The solid curve shows a Gaussian fit to the lower half of the distribution.*

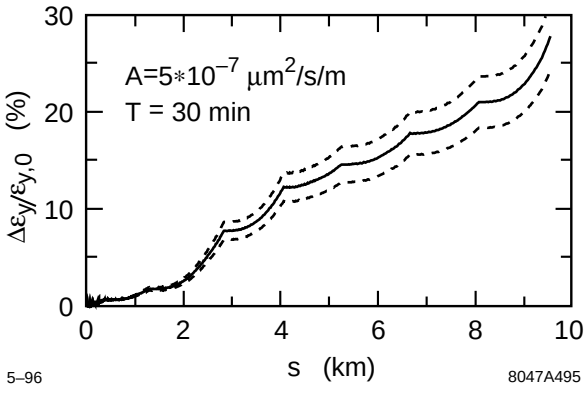

Figure 7-69. *Average vertical emittance growth $\Delta\epsilon_y/\epsilon_{y,0}$ along the linac for ATL-like drifts after 30 minutes. We assume an A-coefficient of 5×10^{-7} μm^2/s/m. The dashed curves specify the error bars around the average (solid curve).*

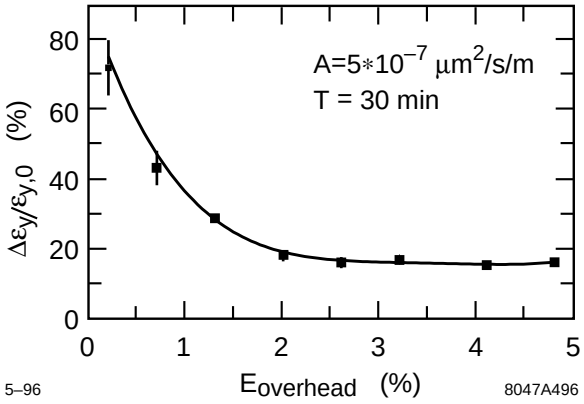

Figure 7-70. *Average vertical emittance growth $\Delta\epsilon_y/\epsilon_{y,0}$ from ATL-like alignment drifts for different BNS configurations.*

Let us relate the ATL-like alignment drifts to the other results. Since the emittance growth is linear in time we would get an additional average emittance growth of about 15% when we assume a beam-based alignment every 30 minutes. This is about a factor of six smaller than the emittance growth expected after beam-based alignment of quadrupoles and rf-structures. It is small enough not to be an important limitation of the NLC linac performance as long as the linacs are corrected regularly every 30 minutes. Since the alignment and correction algorithm does not interfere with the standard operation, its frequent application should be no major obstacle.

7.6.8 Summary and Outlook

A beam-based alignment algorithm for quadrupoles and rf-structures was simulated with a realistic BNS configuration. It was shown that the large initial misalignments from conventional alignment procedures can be corrected to acceptable levels. The emittance growth that finally can be achieved depends on the initial misalignment and most importantly on the performance of the BPMs and rf-BPMs. Assuming an initial misalignment of 100-μm rms, static BPM to quadrupole offsets of 2-μm rms, a BPM resolution of 1-μm rms and an rf-BPM resolution of 15-μm rms, we find an average emittance growth of 90.2% $\pm$ 6.0% for a single bunch. Adding errors of the rf-phases, rf-amplitudes, quadrupole roll angles and quadrupole gradient errors increases the emittance growth to 97.8% $\pm$ 3.6%. Adding the effects of transverse long-range wakefields on the bunch train yields the final multibunch emittance growth of 106.6% $\pm$ 3.9%. This emittance growth is smaller than the allowed total emittance growth of 175%. As the emittances roughly add in quadrature the impact of additional imperfections gets smaller with larger emittances. It is anticipated that the alignment algorithm can be further optimized by smoothing the transitions between alignment sections. Further details can be found in the text.

The dominant stability problem is caused by drifts of the quadrupole alignment. We simulated this effect by using the ATL-model with a coefficient $A = 5 \times 10^{-7}$ μm^2/s/m as measured at SLAC. The use of this model for times of about 1 hour might be overly pessimistic. We showed that the alignment drifts drive coherent betatron oscillations that lead to exponential emittance growth. The addition of seven trajectory feedbacks breaks the coherent betatron oscillation down into eight smaller oscillations. Assuming a beam-based quadrupole alignment every 30 minutes, we get an additional average emittance growth contribution of 15%. Since the emittances roughly add up in quadrature, this is small compared to the 107% average emittance growth after alignment. The alignment algorithm does not interfere with the normal linac operations, so that it can be applied very frequently. We conclude that we can handle alignment drifts safely.

Source		$\Delta\epsilon_y/\epsilon_y$	Dynamics
Quad alignment:		40%	Incoherent dispersion
BPM resolution	1 μm		
BPM-to-quad alignment	2 μm		
Quad drift between alignment:		10%	Coherent dispersion and wakes
Steering period	30 min		
Structure alignment:			
Internal alignment	15 μm	25%	Long-range wakes
Beam measurement accuracy	15 μm	50%	Short-range wakes
Other (*e.g.,* quad roll, ion effects, and rf deflections):		50%	
Total:		**175%**	

Table 7-9. *NLC-IIb linac emittance growth budget.*

Future simulation studies will include internal structure misalignments, multibunch imperfections (bunch-to-bunch charge, energy, etc. variations) and the effects of missing BPMs. In addition, we further want to apply emittance bumps in order to compensate the emittance growth below what has already been achieved. Finally, we need to study the impact of different bunch shapes on the linac emittance transport and we need to simulate the collimation requirements at the end of the linacs.

7.7 Tolerances

In this section we give a brief summary of the tolerances needed to control emittance growth in the main linacs. Simulation studies leading to these tolerance numbers have been discussed in previous sections, especially Section 7.6.

Unless otherwise noted, we assume the NLC-IIb parameters, *i.e.,* a charge per bunch of 1.10×10^{10} with a 150-μm bunch length and an injected normalized vertical emittance $\gamma\epsilon_y = 4 \times 10^{-8}$ m-rad. The tolerances are specified to deliver a beam with a vertical emittance of $\gamma\epsilon_y = 11 \times 10^{-8}$ m-rad. As noted earlier, the primary source of emittance dilution arises from the accelerator structure misalignments with respect to the beam. In the NLC design, the other sources are relatively insignificant, primarily because established beam-based alignment techniques can be used to attain accurate alignment of the BPMs and quadrupoles.

The total emittance budget is given in Table 7-9 for the NLC-IIb linac design. At the present time, we have budgeted roughly half of the allowed 175% total emittance growth to the misaligned accelerator structures. As stated, this partitioning arose because we have more confidence in the quadrupole alignment techniques. Regardless, in the future, we will probably redistribute the tolerances to allow a greater margin for the other effects; this work is awaiting more simulations that incorporate the interactions of these many disparate sources and account for stability errors.

Finally, we should note two points: First, we are calculating the *expected* average emittance growth. In any given case, the growth can be larger or smaller. The larger growths occur when there is a significant correlation of the errors at the betatron frequency, thereby driving the dilution resonantly. Fortunately, these cases are usually very straightforward to correct with simple global correction schemes and thus we are not very concerned about getting a bad "seed" in the collider.

Second, when considering large emittance dilutions, the rms emittance growth is not a very accurate measure of the luminosity degradation. This occurs because the emittance growth mechanisms, such as wakefields, are nonlinear. Thus, they populate the beam tails without degrading the core emittance as greatly as suggested by the rms emittance growth. A more representative quantity is the luminosity reduction which describes the decrease in the overlap of the beams at the IP; we will adopt this measure in the future.

dispersion ($\delta_{\rm eff}$=.2%)

7.8 Operations and Machine Protection System

The operation of the linacs is constrained by the requirements of the Machine Protection System (MPS); the MPS is described in greater detail in Chapter 16. Because the beams have extremely high charge densities, a single bunch train, or even a single bunch, incident on an accelerator structure could cause damage. The philosophy of the MPS is that all preliminary beam-based alignment, tuning, and diagnostics be performed with a full current high emittance single-bunch beam which cannot cause damage in the linac; these operations can be performed at low repetition rates.

As described, the accelerator structures are protected from this diagnostic single-bunch beam with spoilers which are located after every accelerator structure. The spoilers have an aperture that is 2 mm in radius, this is roughly half that of the accelerator structure irises, and they are 0.2 radiation lengths in length. If the beam is steered sufficiently far off-axis to intercept an accelerator structure, it must first pass through one of more spoilers. These will increase the beam angular divergence so that, by the time the single bunch beam strikes a structure, it will not cause any damage. To prevent damage to the spoilers themselves, the emittance of the diagnostic beam must be increased by a factor of ten.

Once the initial beam-based alignment, the basic beam trajectory, and the energy profile are established, a high repetition rate of 120–180 Hz can be established. At this point, the beam emittance can be decreased and additional bunches can be added to the bunch trains. All subsequent tuning must be performed at the high repetition rate.

To verify the beam loading compensation when going to the longer bunch trains, the train length will be increased in steps. Presently, we believe that the loading could be checked using only one intermediate train length, namely, going from one bunch per train to 10 bunches per train and then to a full 90 bunches per train; this needs further verification and increasing the steps has minimal implications for the rest of the systems. In addition, to prevent thermal changes of the accelerator structures when changing from low repetition rate to high rate and from the single- to the multibunch modes, the klystron phases are varied so that the addition power which normally would accelerate the missing bunches is dumped into loads rather than into the accelerator structures; this is discussed further in Chapter 8.

To prevent the high rate beams from striking accelerator components, a $\pm 200\,\mu$mtrajectory window and 10% energy window are established about the nominal values. If the beam deviates beyond these limits in any single pulse, the collider is returned to the high-emittance single-bunch diagnostic mode while the source of the problem is diagnosed from data that was taken during the errant pulse. Extensive logic will be used to prevent erroneous MPS faults due to bad BPMs readings.

This system relies on the fact that there are no transverse deflecting fields that can change sufficiently, within a single interpulse period (roughly 8 ms), to deflect the beams from the operational trajectory window into the accelerator structures. This is attained by limiting the strength of all fast correctors and limiting the decay time of the quadrupole and bending magnet fields by using solid core magnets and thick conducting vacuum chambers.

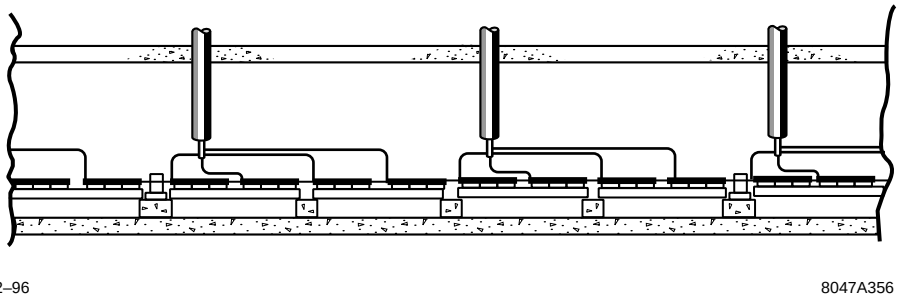

Figure 7-71. *Tunnel cross section and accelerator supports.*

In addition, the MPS must verify that the rf systems are operational before the beams are launched into the linacs. However, fairly large energy deviations can be tolerated. For example, a 20% energy deviation in combination with 100-μm random quadrupole misalignments, which are well in excess of what we expect, would only cause 1-mm orbit offsets.

Thus, the MPS system must only verify that 85% of the rf systems are operational. To this end, all modulators will be polled roughly 100-μs before beam time. At the same time, the klystron timing and phase information will be checked. If there are a sufficient number of failures, the beams will be aborted downstream of the damping rings; this verification procedure is described in greater detail in Chapter 8. Finally, there will be sacrificial spoilers and dumps located in the diagnostic station chicanes to prevent energy errors larger than 25% from propagating further down the linac.

7.9 Linac Components

In this section we give more detailed information on various components of the linacs. In the case of supports and movers, we present our most recent design ideas, and discuss the issues that impact the design.

7.9.1 Supports and Movers

Support Layout

The beam line components will be supported 0.5-m above the tunnel floor at roughly four-m intervals (Figure 7-71). This low height minimizes amplification of ground vibrations but still leaves access below the accelerator. Between supports, accelerator modules will consist of two 1.8-m-long sections of disc loaded wave guide which will be assembled and aligned on a common support girder. Focusing quadrupole magnets will be mounted to the supports at intervals along the accelerator. The spacing between quadrupoles will increase in five discrete steps, scaling roughly as the square root of the beam energy along the accelerator. Figure 7-71 shows the support layout at approximately the 200-GeV point.

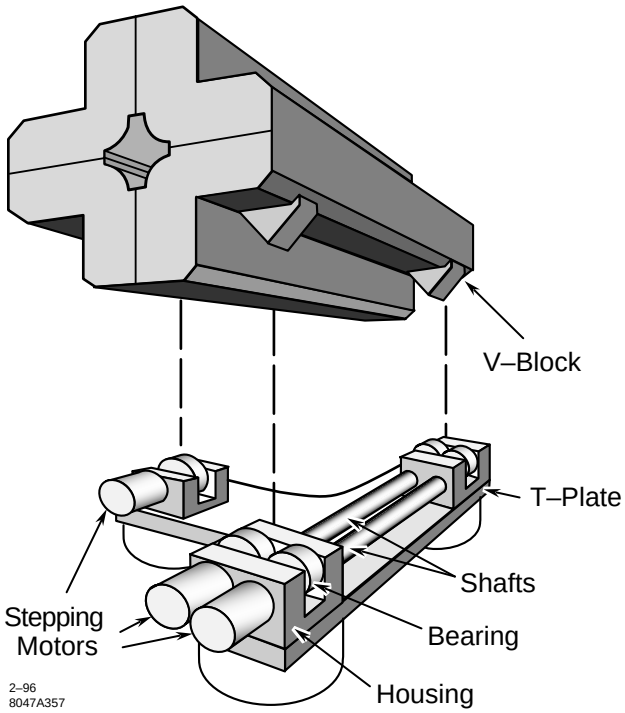

Figure 7-72. *Quadrupole roller cam support.*

Support Design

Both the quadrupole and accelerator structure positions will be remotely controllable. All accelerator and magnet supports will have stepper motor positioning mechanisms with a $\pm$1.5-mm range and a 0.3-μm resolution. Both the accelerator structures and quadrupoles will be kinematically supported in cradles formed by motor-driven roller cams as illustrated for a quadrupole in Figure 7-72.

These mover systems will be similar to the Final Focus Test Beam (FFTB) magnet movers which provide a $\pm$1.5-mm range with 0.3-μm position resolution. The type of kinematic support which will be used, where the number of contact support points equals the number of spatial degrees of freedom, is similar to the kinematic support designs for laboratory optics. It insures reproducible zero-play fixturing of components and will be free of all bending moments which might distort magnets or accelerator modules when they are remotely repositioned. The accelerator modules will rest on 5 cams: cams (1,2,3) on one support will fix roll and the x, y coordinates of that end. Cams (4,5) on the next support will fix the x, y position of the module's other end. Thus each module will be adjustable in x, y, roll, pitch and yaw as illustrated in Figure 7-73.

During operation only the inner eccentric shaft of a support cam will rotate under motor control. The outer bearing race remains fixed in contact with the magnet or module contact foot as shaft rotation lifts the module. Motion is strictly bounded by the design geometry. Limit switches and electronic override protection are not needed. Control system failures can only cause a cam to continue rotating. This is an important advantage for any system with as many as 30 thousand channels of motion. All support cams are arranged so that gravity applies a load torque to each cam shaft drive removing all backlash. All parts move by pure rolling motion and are free of hysteresis from intermittent and reversing sliding friction. These features make sub-micron positioning of heavy objects practical using inexpensive mass produced ball or roller bearings. Details of this mechanism are fully covered in [Bowden, 1996].

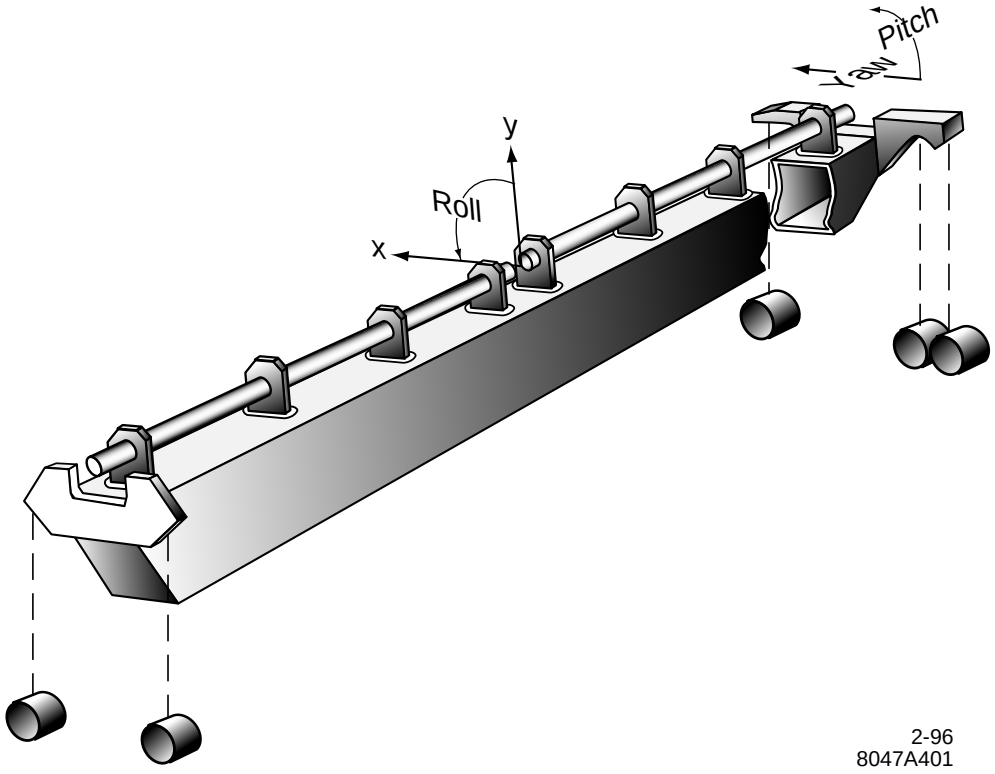

Figure 7-73. *Accelerator girder module support geometry.*

Initial Alignment

All supports will incorporate standard screw and shim manual adjustments which will be used during initial installation to align each support. After the support is manually aligned, accelerator modules and quadrupole magnets will be lowered into their cam cradles as illustrated in Figure 7-74. No further manual alignment is possible or needed. Each module or magnet has had its cam contact feet aligned to their nominal position during assembly. This guarantees the relative alignment between module and quadrupole on installation, reducing, by a factor of two, the number of objects to be manually aligned during installation in the tunnel.

Tunnel Heat Transfer

During operation, thermal distortion can cause serious misalignment of the accelerator. Any successful support system design must avoid or accommodate temperature gradients which could alter alignment. Thermal distortion is the result of thermal gradients which develop when heat is lost by the accelerator to its immediate surroundings. The accelerator cooling system temperature must be set at a temperature sufficiently above the outside air temperature that heat can be expelled even on the warmest days. For example, the existing SLAC accelerator runs with 45°C cooling water because summertime temperatures sometimes reach 40°C in that part of California. This cooling system heats the buried accelerator tunnel to about 40° which is 20° warmer than the surrounding earth. The temperature field for heat flow up from the warm tunnel to the cooler surface is illustrated in Figure 7-75.

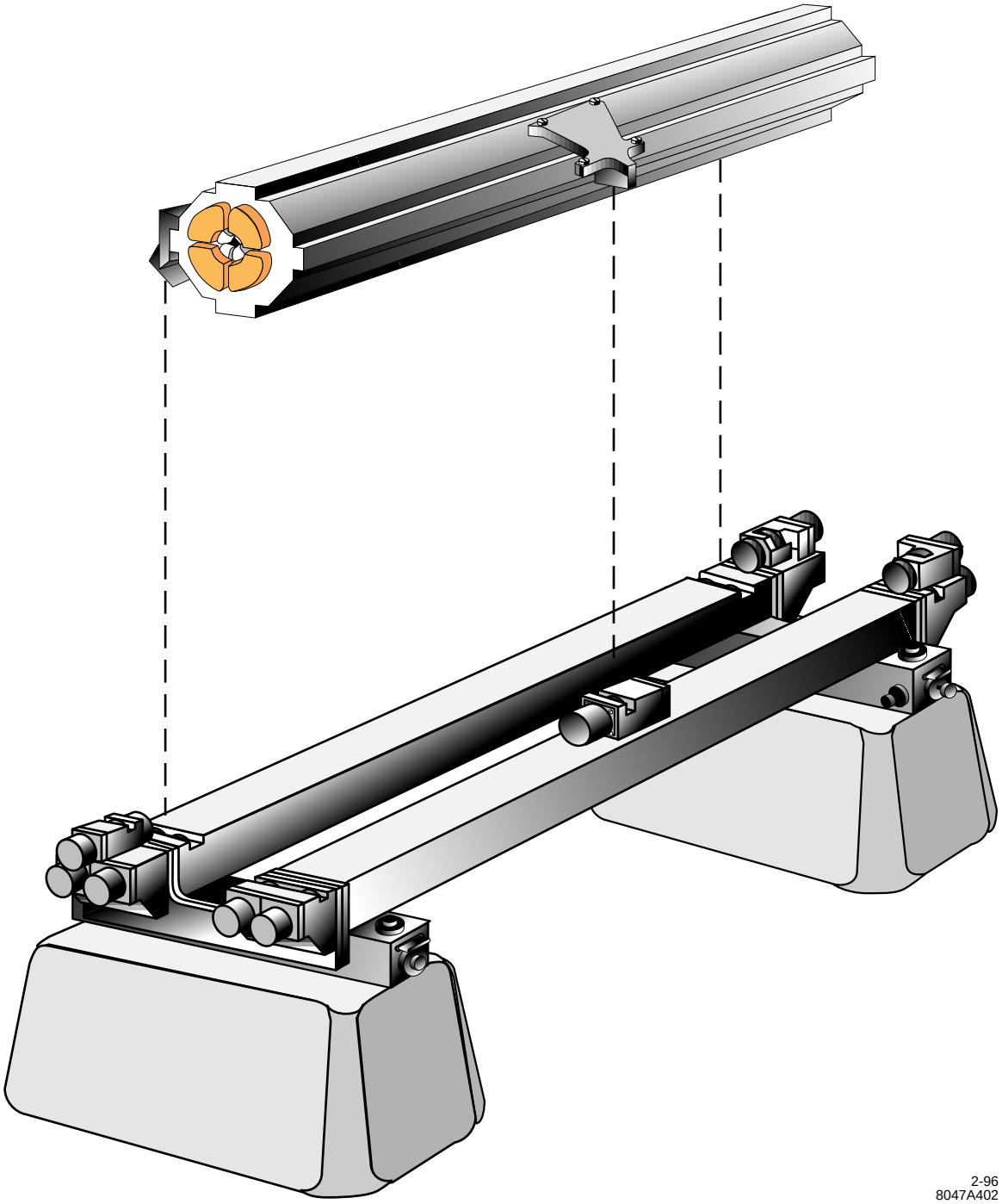

Figure 7-74. *Floor-mounted accelerator remote positioning support assembly.*

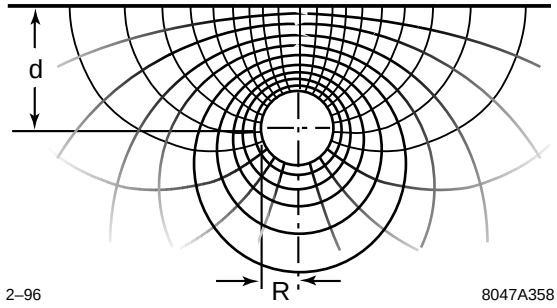

Figure 7-75. *Thermal field of a buried heat source*

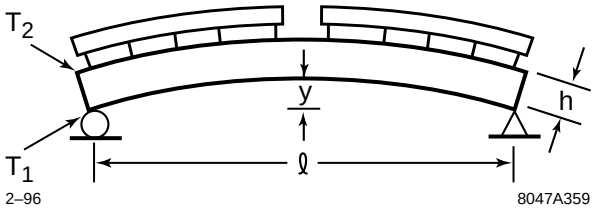

Figure 7-76. *Thermal distortion of a girder*

The thermal conductance between a circular tunnel and the surface is;

$$\kappa = 2\pi\lambda \left(\cosh^{-1}\left(\frac{d}{R}\right)\right)^{-1} \quad (\mathrm{W/\,m^{\circ}C}) \tag{7.19}$$

Heat loss depends on thermal conductivity of the earth λ and the ratio of tunnel depth to radius d/R. For the SLAC accelerator ($\lambda_{\mathrm{sandstone}} = 1.85\,\mathrm{W/\,m^{\circ}C}, d = 10\,\mathrm{m}, R = 1.5\,\mathrm{m}$), approximately 100 W is lost by the tunnel every meter of its length. Although this heat is small compared to the several kW/m carried away from the accelerator structure by cooling water, it is the source of thermal distortions which disturb accelerator alignment.

Girder Distortion

Accelerator modules consist of two 1.8-m-long accelerator structures mounted to a support girder. If the accelerator is mounted on top of its support girder, heat flow will create a thermal gradient across the girder section. The top surface of the girder will be warmer than the bottom which is further away from the source and cooled by natural convection. Differential expansion will cause the girder to arch up toward the warm accelerator, misaligning it. If the girder temperature gradient is linear across its depth, then the distortion is a circular arc of sagitta:

$$y = \frac{\alpha l^2}{8}\left(\frac{T}{h}\right) \qquad \alpha = \text{expansion coefficient } \frac{\Delta l}{l}/^{\circ}\mathrm{C} \tag{7.20}$$

This is illustrated in Figure 7-76. To limit the sagitta to 100 μm, for example, for a 4-m-long, 150-mm-tall, aluminum girder, the thermal gradient can not exceed $\Delta T = 8(100 \times 10^{-6}\,\mathrm{m})(.150\,\mathrm{m})/[(4\,\mathrm{m})^2(23 \times 10^{-6\circ}\mathrm{C}^{-1})] = 0.33^{\circ}\mathrm{C}$. For comparison, measurements across a similar support girder on the SLAC accelerator during operation show a ΔT of .25°C.

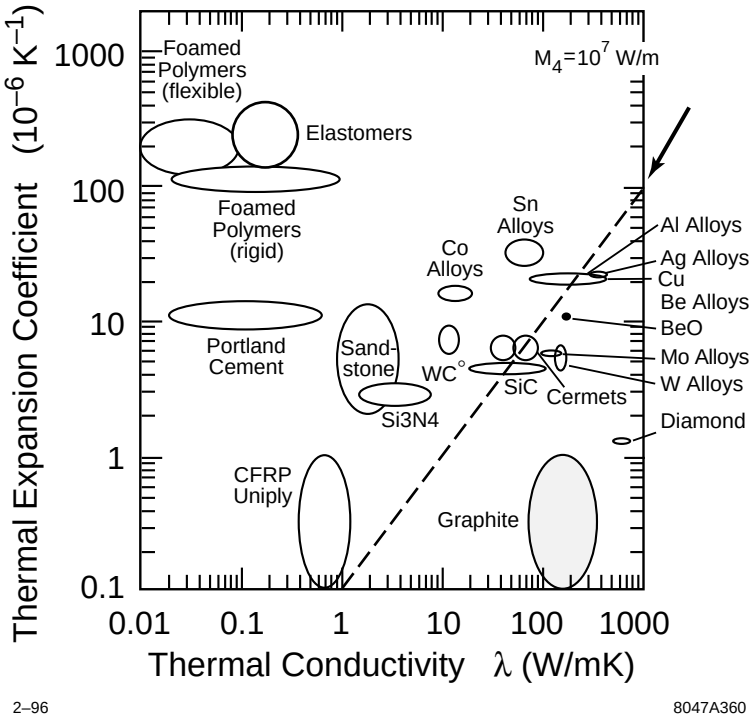

Figure 7-77. *Thermal properties of materials.*

Material Choice

Aluminum has a moderately high expansion coefficient which might appear to make it a poor choice for girder construction. Since thermal gradients are inversely proportional to thermal conductivity, thermal distortion depends on the ratio of conductivity to expansion coefficient λ/α. Judged by this criterion, aluminum is a good choice because of its high thermal conductivity. In a plot of conductivity versus expansion coefficient (Figure 7-77) aluminum proves superior to such low expansion coefficient materials as carbon fiber reinforced plastic (CFRP). Furthermore aluminum has an expansion coefficient $(23 \times 10^{-6\circ}\mathrm{C}^{-1})$ similar to copper $(17 \times 10^{-6\circ}\mathrm{C}^{-1})$ which is used for the accelerator structure and wave guides.

Low Distortion Girders

One method of removing the thermal gradient which distorts girder alignment is to heat the cooler side of the girder, perhaps with a cooling water tube. It may also be possible to enclose the girder in a common insulation jacket together with the temperature stabilized accelerator. From the standpoint of thermal distortion, the girder, ideally, should be an insulated shell enclosing the accelerator.

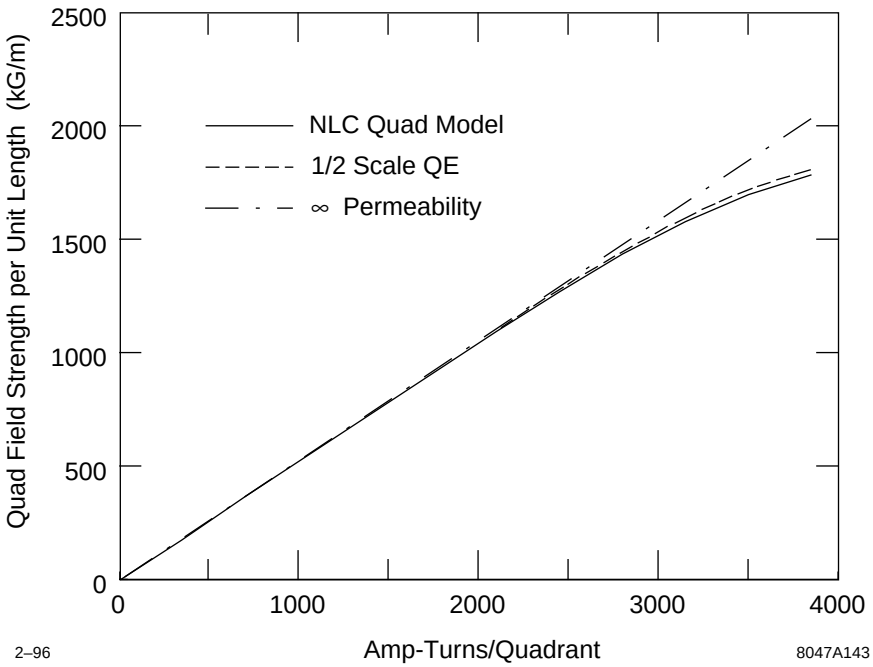

Figure 7-78. *Excitation curve for the NLC model quadrupole magnet and the half scale SLC linac QE magnet. Also shown is the ∞ permeability result, which is essentially the same for both magnets.*

7.9.2 Quadrupole Magnets

Based on the optics requirements, a design study for these quadrupoles was done by scaling the "QE" quadrupole design that is used in the SLC linac. As a starting point, the transverse quadrupole size was halved so the resulting gap width of 13.8 mm will comfortably accommodate a stripline BPM and still not be a limiting aperture compared to the structure irises. To allow the use of standard-sized conductor (0.1875″ square with a 0.100″ diameter cooling hole), and to reduce the magnet power consumption, the coil pocket size was increased while taking care not to significantly reduce the field strength to amp-turn ratio near saturation. A reasonable solution was found even after roughly doubling the coil pocket size. Figure 7-78 shows the resulting excitation curve together with the QE result with a 50% scaling, and the result if the magnet material had infinite permeability (1010 steel was assumed nominally). The NLC quadrupole model magnet would accommodate 17 turns of the standard sized conductor per quadrant compared to 35 turns in the nominal size QE design. This yields a conductor current density of 8.3 kA/in^2 at the maximum current setting (226 A) in Figure 7-78. The field harmonics of this design are also reasonable: 2.6% 12 pole and 2.9% 20 pole at the pole-tip radius, which easily meet the NLC field-quality requirements.

Based on this quadrupole design, quadrupole lengths were chosen to match the linac optics requirements plus allow some overhead (generally more than 30%) at the highest energy operation. Five lengths were chosen which range from 0.2 m to 0.8 m. The operating properties of these magnets can be estimated from Table 7-10 which lists the properties of a somewhat shorter (0.1 m) and longer (1.0 m) magnet that is operated at high current.

Property at I = 225 A	0.1-m magnet	1.0-m magnet
Power Dissipation	1.1 kW	6.9 kW
Water Flow	0.5 gpm	1.5 gpm
Water Δ T	8.7°C	17°C
# of Water Circuits	2	8
Total Coil Resistance	26 mΩ	160 mΩ
Magnet Inductance	0.96 mH	9.6 mH
Time Constant	37 ms	59 ms

Table 7-10. *NLC linac quadrupole magnet properties for two magnet lengths.*

7.9.3 Quadrupole Power Supplies

Since the maximum power dissipation levels in the quadrupoles will be under 10 kW, the quadrupoles can be powered individually at a cost that is competitive with powering them in strings and using shunts. This is because much of the cost is in the control electronics, and because the individual power supplies can be of the simple rack-mounted variety. Having individual control of the quadrupoles is very desirable for beam-based alignment measurements, so we will likely power them individually. This also eases the supply stability tolerance—a regulation of 6×10^{-5} will be required, which should not be difficult to meet.

7.9.4 Multibunch Kicker

The kicker for the bunch-by-bunch trajectory correction is assumed to be a terminated TEM-mode parallel plate vacuum transmission line. The electric and magnetic kicks are equal in magnitude, but cancel unless the TEM wave is traveling in the direction opposite to the beam, so it is not possible to synchronize the wave with the beam. If the stripline length is shorter than half the bunch spacing, different bunches are deflected by entirely independent parts of the driving waveform.

The Fourier spectrum of the kicker was assumed to cut off abruptly at some frequency for the beam dynamics studies. There was no improvement for cutoffs above 250 MHz, which is lower than the bunch frequency of 714 MHz. This indicates that it is not necessary to have independent control of each bunch. A stripline of length 60 cm would have a zero-crossing in its response at 250 MHz, but the response is not flat. A 30-cm stripline length would have a flatter response out to 250 MHz, and would have its first zero-crossing at 500 MHz.

The kicker strength available was assumed to be 56 keV/c for the beam dynamics studies. For $E = 100$ GeV, $\epsilon = 3 \times 10^{-8}$ mr, and $\beta = 10$ m, we have $\sigma_\theta \approx 0.1\,\mu$r. This is equivalent to $\sigma p_\perp \approx 10$ keV/c. Thus the kicker strength is about 6σ in the beam dynamics simulation.

A deflection of 10 keV/$c \approx 1\sigma =$ requires about 30 Gauss-cm. For a deflection of 10σ, the magnetic field integral is $BL \approx 300$ Gauss-cm $= 3 \times 10^{-4}$ T m. Generating a magnetic field B between strips of width w separated by gap g requires a current $I = Bwf/\mu_0$, where f is a geometrical form factor that depends on g/w and is of order 2. In terms of BL, this can be written $I = (BL)(w/L)f/\mu_0$. For $L = 30$ cmfor independent bunch control, and $w = 1$ cm, a 10-σ deflection requires 16 A of current. The impedance of the stripline structure is $Z \approx (g/w) \times 377\Omega$. Assuming $Z = 200\Omega$, 3.2 kV are required for 16 A. These parameters are within the range of solid-state components. The instantaneous power is 50 kW, but with a very low duty factor.

Chicane	Max. Energy (GeV)	Num. Bends	Max. B (kG)	$L_{\rm eff}$ (m)
1st	32	4	5.25	1.60
2nd	80	4	2.26	3.50
3rd	165	8	1.63	2.65
4th	290	8	1.27	3.50

Table 7-11. *Dipole magnets for the linac diagnostic chicanes.*

There are several conservative assumptions in the above estimates. The kicker strength is 100 keV/c, where 56 keV/c was adequate. The electric kick was neglected, though it is equal to the magnetic kick. Doubling the strip length would allow the same kick strength at half the voltage and current, although it would cost some strength near the 250-MHz cutoff.

The striplines would see the full beam image current, which would be coupled into the input and output ports. The coupling should be very strong, to avoid trapped modes on the strips. The drivers and terminations would be exposed to the coupled image currents. Since the bunches are very short compared to the drive bandwidth, low-pass filters would protect the equipment. Reflections of the image currents would disturb subsequent bunches. A simple way to avoid this problem is to use cables or waveguides with delays longer than half the bunch-train length between the striplines and the filters, drivers, and terminators.

7.9.5 Chicanes

The chicanes are constructed from relatively low field rectangular bending magnets. They have 2-cm vertical gaps and a horizontal good field region $\Delta B/B \leq 10^{-3}$ of 4 cm; the magnet lengths and fields are listed in Table 7-11. All magnets in each chicane, *i.e.*, the four or eight magnets, are powered in series with a 20-kW power supply that is rated at 100 V and 200 A and has a stability of $\Delta I/I \leq 1 \times 10^{-4}$ over the period of one hour.

7.9.6 Beam Dumps

The present design does not have any beam dumps located along the linacs. There is a high power dump after the final diagnostic station at the end of each linac. These dumps will be able to absorb the full 16-MW beam power so that the linacs can be commissioned and studied without sending beams downstream. The design is the same as final beam dumps located after the IPs which is described in Chapter 11.

The beams will be deflected to the dumps using pulsed kickers that operate at the full 180-Hz repetition rate. This allows tuning of the linacs before sending full-rate beam downstream as required for the MPS. At this time we do not have designs for the dump line kickers, but they are straightforward magnets, similar to pulsed dumper magnets in the SLC.

Resolution (minimum variation meas.) at 10^{10} ppb	1-μm rms
Position stability during 24 hours timescale	1-μm rms
Position absolute accuracy	0.2 mm
Position dynamic range	0–2 mm
Number of bunches	1–90
Bunches separation	1.4 ns
Beam current dynamic range	$5 \times 10^8 - 1.4 \times 10^{10}$ ppb
Maximum cycle frequency	180 Hz
Maximum time for data processing	1 ms
Total number of monitors	3000

Table 7-12. *Requirements for "Q" BPMs.*

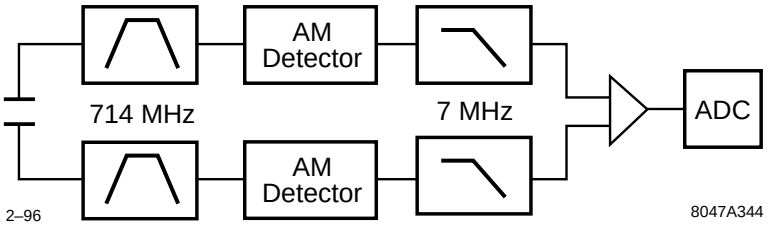

Figure 7-79. *"Q" BPMs signal processing block diagram.*

7.10 Instrumentation

The NLC Beam Position Monitor System (BPM) must measure the average beam position of a single pulse containing from 1 to 90 bunches, and must provide bunch-by-bunch position information to the feedback system. Different systems are used to accomplish these tasks: quadrupole BPMs ("Q"), feedback BPMs ("FB"), and structure BPMs ("S"). There are about 3000 "Q" BPMs, 200 "FB" BPMs, and 9700 "S' BPMs. The "Q" and "FB" BPM mechanical detectors are realized with four buttons or short striplines, two in each plane. The "S" BPMs are realized with rf couplers within the cavities. The BPM layout is not included in this study, and therefore no cable plan or signal attenuation is considered in the analysis.

General design considerations should be applied: keep as much electronics as possible out of the tunnel for low radiation and easy maintenance, keep as much preprocessing as possible at the BPMs electronics rack location to reduce the communication bandwidth and expedite the feedback system.

7.10.1 Quadrupole and Feedback Beam Position Monitors

The quadrupole BPMs ("Q" BPMs) must be able to detect the average position of the train of bunches, that can contain from 1 to 90 bunches in the single pass. The system's requirements are shown in Table 7-12.

The toughest requirement is the position stability, which asks for better than 1-μm systematic error. This means 0.005-dB stability for a 6-mm-radius circular beam pipe. In order to achieve such a good performance, a special calibration scheme is necessary.

A synchronous detection technique is used to process the signals from the striplines, which amplitude demodulates the signal and provides either linear or logarithmic functions, as shown in Figure 7-79.

The expressions to calculate the position are respectively:

$$x = \frac{b}{2}\frac{A-B}{A+B} \tag{7.21}$$

for linear demodulation, where b is the beam pipe half aperture, and:

$$x = \frac{1}{S_x}\log\left(\frac{A}{B}\right) \tag{7.22}$$

for logarithmic demodulation, where S_x is the sensitivity (in dB/mm), dependent on the electromagnetic sensor geometry.

The expected signal level for a gaussian beam with a bunch length much shorter than the bunch spacing, is given by:

$$V(\omega) = \sqrt{2}\frac{Ne}{T}gZ\sin\left(\frac{\omega l}{c}\right) \tag{7.23}$$

where N (=10^{10}) is the number of particles per bunch, T (=1.4 ns) is the bunch spacing, g (=0.2) is the electrode coverage, Z (=50) is the impedance, l (=20 mm) is the stripline length, and ω is the processing frequency (= $2\pi \times 714$ MHz). Under these assumption the rms voltage at the stripline is:

$$V = 1.3V \quad . \tag{7.24}$$

The system's resolution is given by the following formula:

$$x[mm] = \frac{b}{4}\left(\frac{N}{S}\right) \tag{7.25}$$

where b is the beam pipe radius (in mm) and N/S is the voltage signal-to-noise ratio. One of the resolution limits is the thermal noise, which is:

$$P_n[dBm] = -174 + 10\log(BW) + NF \tag{7.26}$$

where BW is the electronics bandwidth and NF is the electronics noise, while the signal strength must be computed for the different type of electromagnetic pickup and electronic processing.

The rms noise voltage, using 7-MHz bandwidth and 15-dB noise, is:

$$V = 7\ \mu\text{m}\ V \tag{7.27}$$

and the expected resolution due to the thermal noise is:

$$x = 8\,\text{nm} \quad . \tag{7.28}$$

Another resolution limit is given by the amplifier's Common Mode Rejection Ratio (CMRR) which is defined as the ratio of response for a differential change signal when both signals have the same amplitude. A hard but achievable value is 80 dB, which corresponds to:

$$x = 150\,\text{nm} \tag{7.29}$$

according to the expression in Eq. 7.21. If ADCs are used to digitize the values and the difference is digitally calculated, 14 bits are required for a comparable resolution. Things get worse when additional dynamic range must

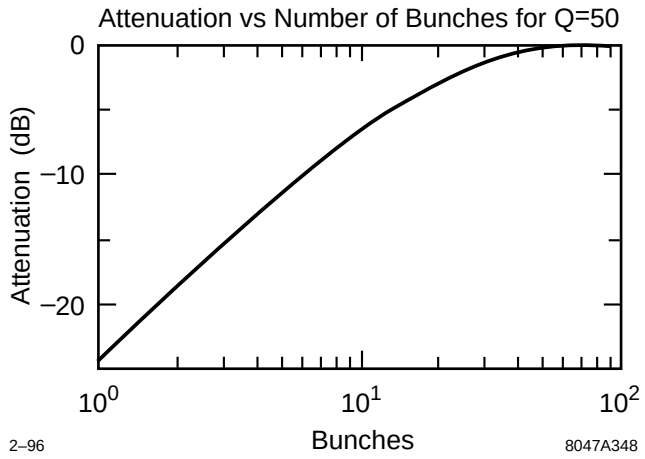

Figure 7-80. *Attenuation vs. number of bunches.*

Number of channels	4
Analog bandwidth	1 GHz
Sampling rate	10^9/s
Number of bits	10
Triggering	int/ext

Table 7-13. *Single-bunch BPM characteristics.*

be used for beam current fluctuation, because part of the CMRR must be used to take care of it. When the signal generated by the single bunch pass through the bandpass filter that has 714-MHz center frequency and $Q = 50$, to give 7-MHz bandwidth to the electronics, it produces a ringing whose amplitude is attenuated by 24 dB with respect to the 90 bunches case, as shown in Figure 7-80. This number was derived assuming the demodulation process bandwidth to be limited by the single-pole low-pass filter.

The expected resolution due to thermal noise in single-bunch s therefore:

$$x = 127\,\text{nm} \tag{7.30}$$

to which the CMRR contribution should be added as well.

7.10.2 Feedback BPMs

The “FB” BPMs must be able to detect the position of individual bunches within the pulse, for feedback correction. The same “Q” BPMs system requirements in Table 7-12 apply, the only difference being the resolution:

$$x = 0.25\,\text{nm} \quad . \tag{7.31}$$

The electronics processing is realized with four channels digitizers that sample the signal peaks from the striplines. An example of such a module is the Tektronix TVS545, a $20k VXIbus based module whose pertinent characteristics are shown in Table 7-13.

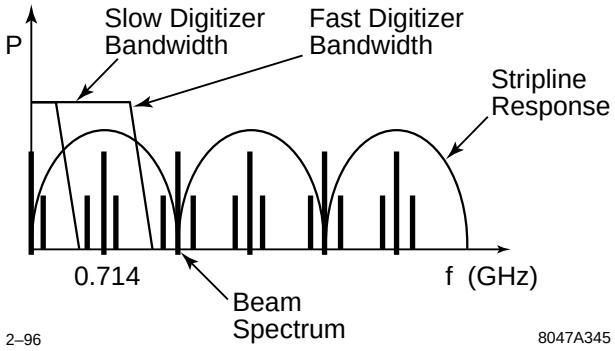

Figure 7-81. *Principle of "FB" BPMs*

The trigger is either generated on the signal's peak, or generated by the timing system. It is very important to minimize the trigger jitter, because it produces 1-μm position error each 5 ps jitter, given the 12-mm beam pipe full aperture. A possible solution to this problem is to oversample the signals and to reconstruct the waveform, but higher sampling rate than currently possible will be required. This technique will reduce the jitter performance requirements and will not require the clock to be beam synchronous. The expected signal level peak for a gaussian beam with a bunch length much shorter than the stripline length, is given by:

$$V = \frac{gZ}{2}\frac{Ne}{\sqrt{2\pi}\sigma}\left(1-\exp\left(-\frac{\tau^2}{2\sigma^2}\right)\right) \approx \frac{gZ}{2}\frac{Ne}{\sqrt{2\pi}\sigma} \quad . \tag{7.32}$$

Where N (=10^{10}) is the number of particles per bunch, g (= 0.2) is the electrode coverage, Z (= 50) is the impedance, $\tau = 2l/c$ (0.7 ns), l (=20 mm) is the stripline length, $\sigma = 1/(2\pi BW)$, and BW is the filter -3 dB point. Under these assumption the rms voltage at the stripline is:

$$V = 14V \tag{7.33}$$

and the rms noise voltage, using 1-GHz bandwidth and 15-dB noise, is:

$$V = 80\,\mu\mathrm{m}\,V \quad . \tag{7.34}$$

The expected resolution is:

$$x = 9\,\mathrm{nm} \quad . \tag{7.35}$$

Another resolution limit is given by the ADC number of bits. The TVS545 module, with its 10 bits, guarantees:

$$x = 1.5\,\mu\mathrm{m}\,\mathrm{m} \quad . \tag{7.36}$$

In order to achieve the required resolution performance, the ADC must provide at least 13 bits or the use of hybrids must be included to reduce the system's required CMRR.

If the technology becomes available and the cost is affordable it might be possible to include the "FB" BPMs in the "Q" BPMs using a wideband AM detector, working, for example, with 11.4-GHz carrier and 350-MHz bandwidth. An interesting possibility is to reduce the system bandwidth to 350 MHz and maintain the oversampling process. The equivalence of the two processes is shown in Figure 7-81 where the beam spectrum is relative to a 714-MHz pulses repetition, with sidebands indicating amplitude modulation due to current and position fluctuation, and the length of the stripline is adequate to peak the pulse repetition rate. The fast digitizer samples synchronized with the bunch spacing, and in this way amplitude demodulates the signal, providing the equivalent power of the first three sidebands. When the slow digitizer is used, there is still signal available, but the power is only given by the first sideband.

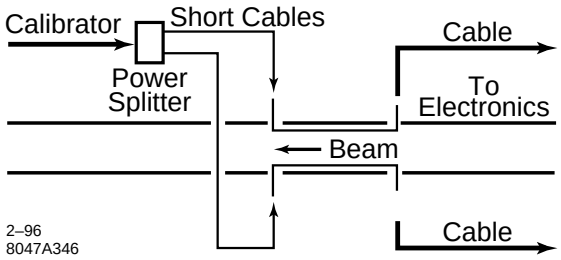

Figure 7-82. *Calibration scheme.*

The best condition for the slow digitizer option is when the length of the stripline is approximately 15 cm: in this case its response notch corresponds to the bunch repetition frequency.

This slow digitizer principle is different from the amplitude demodulation in the sense that there is no DC signal available because of the stripline transfer function. A way of defining this type of signal processing would be: AC coupled amplitude demodulation, where the modulation signal is the position variation versus time. It is important to notice that when the beam doesn't move there is no modulation, and therefore no signal. In a sense this type of signal processing provides the modes of the position variation: if the beam presents a bunch-by-bunch displacement, the output of the BPM will show a 357-MHz line in the frequency plot, if it presents a sinusoidal displacement with period 10 bunches, the output will be a 71.4-MHz line in the frequency plot, and so on.

It is possible to deduce from the picture in Figure 7-81 that the amplitude of the signal increases with the frequency of the modulation signal, that is the position variation. It is possible, in principle, to recover the signal information using the transient at the beginning of the pulse. The idea is to calibrate the system with a single bunch, measuring the impulse response. The position is then available by deconvolving the measured signal with the impulse response.

Calibration

In order to achieve 1-μm stability from the "Q" and "FB" BPMs, which corresponds to 0.005 dB for a 6-mm-radius circular beam pipe, it is necessary to include an efficient calibration scheme.

The calibration scheme in Figure 7-82 includes a signal to be injected at the other end of the striplines. The power splitter divides the signal between the two striplines simulating the beam on center. In this way both electronics and cables will be calibrated. This calibration scheme is more expensive than the conventional one, where the signal in injected at the electronics through a combination of three power splitter/combiner, because each stripline needs two feedthroughs instead than one and each BPM needs one more long cable for the calibration signal. The possible sources of instability are the power splitter unbalance and the short cables insertion loss. Off-the-shelf stripline power splitters have 0.2-dB typical amplitude unbalance, which corresponds to 40 μm in our case, and 0.005-dB drift over 10°C temperature change.

The short cables insertion loss variation can be kept under control by using good cables as short as possible. A typical temperature change for 12-ft coaxial cable is 0.05 dB/10°C: that means that the cables must track to better than 10% in order to maintain within the required tolerance.

7.10.3 Structure Beam Position Monitors

Overview

In this section, we outline the physical scalings and technique for use of accelerating structures as monitors of beam position and beam phase. We also discuss briefly their employment as monitors of higher-order moments.

The "S" or structure BPMs are the damped detuned accelerating structures, operated parasitically as beam position monitors. In this structure, as described in Chapter 8, four nearly rectangular vacuum manifolds are situated parallel to and mated in the structure in such a way as to couple out deleterious "dipole" modes which otherwise would disturb the beam. These manifolds effectively lower the Q of the dipole modes of the structure, reducing the multibunch wakefield and aiding in the control of emittance growth. At the same time these manifolds provide a conduit for microwave signals that can provide information about the beam. Our use of this structure as a BPM is entirely parasitic to this manifold-damping.

The S-BPM allows one to monitor the transverse position of the bunch train with respect to the *electrical center* of the front, rear, or other specific portions of the structure. This is distinguished from other BPMs that measure the transverse position of the bunch train (Q-BPMs) or a single bunch (F-BPMs) with respect to a locus (the BPM structure centroid) with no *a priori* dynamical significance, except that established by accurate alignment with respect to other beam line elements (*e.g.*, quadrupole centroids). Misalignments revealed by an S-BPM could (on a time-scale to be determined) be subject to feedback to zero them out, as such offsets give rise to deflecting wakefields that tend to produce emittance growth. The feedback might take the form of a pair of movers (X and Y) at the front and rear of each structure.

Physical Principles

Structure "dipole" modes are rather similar to the TM_{11} modes of cylindrical guide, insofar as they couple linearly (for sub-mm displacements) to the beam offset from the electrical center of the structure. However, each structure consists of some $N_{\rm cell} = 206$ coupled cavities or "cells," and thus there are some 206 different dipole modes, each of which tends to be synchronous with the beam over only a limited region of a few cells. For the DDS as presently designed, the mode frequency is correlated with position along the structure, such that the lower frequency range (14 GHz) modes tend to couple well to the beam near the entrance of the structure, while the higher frequency range modes (16 GHz) tend to couple well near the exit. Thus the filtered microwave signal emanating from the manifold ports provides information on the misalignment of the beam relative to different portions of the structure. The raw phase and amplitude of a dipole mode can only be interpreted as a signed displacement if we have knowledge of beam phase and amplitude. The phase information will come from the timing system and the amplitude will come from "Q" BPMs located in the nearest quadrupole. We expect to be able to measure the position of trains of 90 bunches of 5×10^9 particles per bunch to a resolution of better than 1 micron rms for at least several modes corresponding to both ends of each structure.

Some simple scalings can be employed to describe the rf structure as a pick-up. In one 1.8-m structure the $N_{\rm cell}$ modes will be distributed in frequency from 14–16 GHz (roughly a mode-spacing of 10 MHz) and a mode $Q_e \sim 1000$, corresponding to a decay time $2Q_e/\omega \sim 20$ ns. Modes will overlap since the typical FWHM = $\omega/4\pi Q_e \sim 15$ MHz. The energy deposited in one mode by a single bunch of charge Q_b is $U = k_l Q_b^2 (x/a)^2$, with x the beam offset, a ~0.3–0.7 cm the iris radius, and k_l ~1–4 V/pC/cell the loss factor for the mode in question. For a bunch train, the figure for stored energy is U multiplied by a train form factor F, which is a function of mode frequency and the number of bunches in a decay-time, $N_{bf} \sim 14$. This form factor can be computed by convolving a periodic sequence of delta-functions with a damped sinusoid. For modes with frequencies that are integer multiples of the bunch train frequency

(714 MHz), $F = N_{bf}^2 \sim 200$. These frequencies are 14.280 GHz (0.714 $\times$ 20), 14.994 GHz ($\times$ 21), 15.708 GHz ($\times$ 22), 16.422 GHz ($\times$ 23). For modes that are half-integer multiples of the bunch train frequency, $F = 1/4$. These frequencies are 14.637 GHz ($\times$20.5), 15.531 GHz ($\times$ 21.5), 16.065 GHz ($\times$ 22.5). For other modes, $F \sim N_{bf} \sim 14$. A rough estimate of peak power flowing through one manifold arm from a given mode is just $P \sim \omega U/2Q_e$. For the time being, we adopt this as an estimate for power coupled out of the manifold port, recognizing that the actual figure will depend on attenuation and propagation characteristics in the manifold.

To appreciate these scalings, consider the extreme cases. Maximum peak power from one mode, resonantly excited by a bunch train steered into an iris would be 1×10^3 W, assuming $k_l \sim 4$ V/pC/cell, and 5×10^9 particles per bunch (0.8 nC). Peak power in the full bandwidth (14.5–16.5 GHz) would be about 1×10^4 W. Average power deposited in this case would be less than 1 W. Minimum power would correspond to the case of a single bunch of 3×10^9 particles (0.5 nC) offset by 5 μm, $P \sim 6\mu\,\mathrm{W}(-22\,dB)$, assuming $k_l \sim 1$ V/pC/cell and $a \sim 0.7$ cm. For comparison note that thermal noise in any 15-MHz interval is $N \sim -102$ dB, roughly the power level corresponding to a 0.5-nm beam offset. In addition one wants to compare this figure with that for the $m \neq 1$ terms in the impedance (both broadband and resonant terms if there is any coincidental overlap) over the bandwidth of interest, a figure not yet calculated.

Technique

Each structure has four damping manifolds. The manifolds must be terminated on each end to dissipate the higher-order mode power. Two of the terminations, one on a horizontal manifold and one on a vertical manifold, will be provided by waveguide to coaxial vacuum feedthroughs which bring the higher-order mode power out onto external cable to provide the position signals. The other six terminations are probably internal to the manifold to minimize costs. Coaxial cable can be used since a run of no more than 80 ft will extend out of the accelerator housing proper to a front-end electronics rack. Cable losses are high in this frequency range, *e.g.*, ~30 dB/100′, but signal power is plentiful if we're only trying to achieve micron resolution. No special requirements for temperature-stability of the cable are envisioned.

Rf pre-processing modules are located at the top of the nearest tunnel penetrations. These integrated microwave modules bandpass filter, attenuate (through fixed and programmable attenuators), and selectively mix down any frequency in the dipole band to a fixed intermediate frequency (IF). Mode selection is accomplished by tuning the local oscillator provided at each crate of rf processing modules. The down-conversion mixers can be protected from burnout by a combination of fixed attenuation and PIN diode limiters even if programmable attenuators are inappropriately set. The IF signals are pre-amplified and sent to the nearest instrumentation alcove for further processing.

In the instrumentation alcove is a VME crate containing IF processors for the structure BPMs. Each IF processor measures the phase and amplitude of the X and Y IF signals from each of four structure BPMs. The input signals are quadrature demodulated, sampled at a time specified by the timing system, and digitized. Phase rotation and amplitude normalization is provided by an onboard signal processor. The processor will provide simultaneous X and Y position measurements for all four structure BPMs on the same beam pulse. Since the local oscillator is shared across BPMs, they all measure the same mode (frequency) on any one machine pulse.

Other Issues

We intend to study two additional signals as possible candidates for the list of raw signals to be processed. These are a second-moment coupled signal (TM_{21}-like, at f_2) and a third-moment signal (TM_{31}-like, f_3). Such signals derived from several structures can provide single-shot measurements of beam emittance and beam profile asymmetry, at least, in the horizontal. A rough estimate of energy deposited in such modes would be $U = k_l Q_b^2 (x/a)^{2m}$ where $m = 2$ or 3. Assuming $Q_e \sim 5000$, $k_l \sim 1$ V/pC/cell and $a \sim 0.7$ cm, and a single bunch of 3×10^9 particles (0.5 nC), this

corresponds to $P_2 \sim -40$ dB for a 100-μm beam feature and $P_3 \sim -77$ dB. These numbers indicate that pursuit of still-higher moments is probably not practical. The third moment is looking a bit problematic for a single bunch.

The contribution of the $m \neq 1$ terms in the impedance to the 14.5-16.5-GHz-band signal offset will be studied at ASSET.

Conclusion

The electronics alluded to here and the structure itself are still being designed and will be tested with beam during the next ASSET experiment and at the NLCTA. It is expected that modifications and improvements will derive from practical operating experience.

Primary issues will be cost, reliability, dynamic range, and circuit protection. For a simple nonsigned S-BPM, the primary cost is the GADC unit. For a signed S-BPM, the primary cost is likely to be in the microwave electronics (LOs, mixers, etc.). An assessment of reliability awaits experimental studies at ASSET. The need to protect the processing electronics in the worst case (bunch train steered into an iris) will probably limit the useful dynamic range.

To summarize, S-BPM resolution is favored by minimum insertion loss for microwave signals emerging from the manifold. The S-BPM will be capable of resolving 5-μm beam offsets shot-to-shot relative to specific portions of the structure, *e.g.,* near the entrance and the exit. The limits of S-BPM resolution and functionality, as well as tests of the electronics await experimental studies at ASSET.

7.10.4 Laser Wire Scanners

Laser-based beam profile monitors, to be used with damped beam, will be described in this section. The laser-based profile monitors will be similar to the one under construction for the SLC/SLD IP. This device uses a diffraction limited, 350-nm wavelength, laser. The laser beam will be scanned across the particle beam on a consecutive sequence of pulses. The system will have four components, a single synchronized laser, a transport line to deliver photons to several interaction chambers, the interaction chambers themselves and scattered radiation detectors that detect boosted photons and/or degraded e^+ or e^- from the interaction of the laser light with the particle beam. The amplitude of the light can be varied in order to accommodate a very wide dynamic range of beam size and intensity.

Laser

A laser will be used to provide a 10-mW peak power pulse to six interaction chambers. In these chambers the particle beam will be brought into collision with the focused laser beam. The light pulse will be 0.1-ns-long, short enough to interact with only one of the 90 bunches. The synchronization of the light pulse with the particle beam will done using a mode locked seed laser. The seed laser output can be amplified using a regenerative YAG 20-pass amplifier. Expected synchronization accuracy is at worst 10 ps. The laser phase space is defined by a high-power pinhole spatial filter. The laser will be located in an accessible area.

The laser can be operated in the lowest transverse spatial harmonic mode or in a higher mode. In the first mode, a null is generated where the center of the gaussian beam would ordinarily be. Two side lobes are arranged around the null and this structure can be scanned across the beam as an alternative to scanning the gaussian zero mode spot. The spacing between the lobes provides an estimate of the performance of the laser focusing and transport optics.

Transport

The transport is used to bring the laser light to up to one of six interaction chambers. It can be of roughly any length provided the surface figure of its optics is good enough. Typical surfaces must be l/40 or better. Starting from the spatial filter and progressing through the transport and the interaction chambers, the accumulated optical errors must be kept below a modest surface figure budget of about a half wave. The transport must be evacuated and free from significant contaminants. Steering elements are required for trajectory stabilization and optimization. Diagnostic imagers are needed to maintain transport alignment and monitor optical quality.

Interaction Chambers

The function of the interaction chambers is to focus the light to a spot small compared to the expected beam size. This can be done using an F2 focusing system with a 95% transmission aperture. In this system demagnification is traded off against diffraction-related tails and distortion. Absorbing materials are needed to keep the optics free from the contamination caused when metal material is removed by stray laser light.

The locations of the interaction chambers will be dictated by the local optics. For the measurement of an uncoupled beam matrix a minimum of three scanners, separated by 45 degrees of optical phase advance, are required. For the determination of a fully-coupled beam matrix, six scanners are needed. The placement of the scanners in the diagnostic stations is described in Section 7.3.4.

The laser beam will be scanned across the particle beam using piezo-electrically-driven mirror actuators. The laser beam can either be scanned slowly, so that it advances a fraction of a bunch size on each successive machine pulse, or scanned rapidly, so that it crosses the entire bunch train during a single passage. In the latter case, an estimate of the projected full train emittance can be derived from the response of a single high-bandwidth detector or group of detectors. The focused laser spot must move <4 sigma during the 100-ns passage time. Fine synchronization is required to time the collision between the light and the particles.

Detectors

Scattered radiation detectors are needed to detect the degraded particles and the boosted photons. In the latter case, the beam line geometry requires a bend to remove the electron beam from the path of the photons. A very large signal of about 1000 photons is expected for the single-bunch parameters and laser power listed above. In some cases the Compton scattered signal may be used as an indication of the degree of polarization of the beam.

7.11 Discussion

In this chapter, we have presented the design of the NLC main linacs and have described how the linacs will be operated so as to prevent large dilutions of the beam emittances. We have presented the emittance dilution budgets for the different operating modes of the linacs: NLC-Ia—NLC-IIc. The budgets are generous and have been chosen to allow for reasonable fabrication and construction tolerances.

As discussed, the approach to preserving the small beam emittances is two-fold. First, many problems have been explicitly `designed-out'. In particular, the damping and detuning of the accelerator structures will make the wakefield effects associated with multibunch operation manageable. Similarly, the thermal regulation in the tunnel and gallery

will prevent significant fluctuations in alignment and instrumentation response. Second, we will utilize beam measurements to suppress unavoidable imperfections that are not readily solvable by design. These include the alignment of the quadrupole magnets and accelerator structures and the stabilization of the beam orbits and energies.

To perform the alignment, each quadrupole and pair of accelerator structures will have remotely adjustable supports. With this control, the only tight alignment tolerance that will have to be achieved prior to operation is that for the straightness of the accelerator structure pairs. The beam-based alignment algorithms that will be used are fairly straightforward. The quadrupole alignment method is a variation of one that has been successfully applied in the SLC and FFTB, although it places higher demands on the BPM stability and the performance of the control system. The structure alignment technique is more novel in that it uses the signals from the structure damping manifolds to infer the beam offset in the structure. With this information, each pair will be aligned to the beam after a suitable orbit has been established.

It is important to note that these beam-based alignment techniques do not need to interrupt standard operation and we have shown that the emittance growth due to slow alignment drifts (ATL-model) can be controlled by re-aligning every 30 minutes. To further stabilize the beams, there are trajectory and energy feedback loops, like those used in the SLC, implemented throughout the linacs. These feedbacks will heavily suppress the effect of low-frequency (<0.1 Hz) sources of beam jitter and drifts. At higher frequencies where the feedbacks are not effective, we do not foresee any significant sources of jitter. The primary source of high frequency jitter is due to ground motion which, as discussed in Appendix C, we have measured and found to be well below tolerance.

The estimates of the emittance growth in both NLC-I and NLC-II are based in part on detailed simulations of beam transport in the linacs that include the significant deleterious effects and have been calibrated against SLC experience. Smaller effects have been estimated analytically with guidance from SLC observations. Furthermore, we have a number of fallback methods available to control the emittance growth, such as orbit bumps, which we are confident will provide additional suppression.

In the future, we plan to continue to optimize the linac design. Additional simulations and experience from operating the NLCTA and the SLC will guide the work. In particular, the NLCTA will give us a measure of the energy gain stability and beam-loading compensation in an NLC-like multibunch environment. In addition, there are number of dedicated studies planned for the next year that will develop or verify other key design concepts. These include tests of the structure alignment technique, development of stable stripline BPMs, and monitoring of the long-term straightness of the accelerator structures. From this work, we will be able to transform the linac design to a full CDR in the near future.

References

[Adolphsen 1993] C. Adolphsen and T.O. Raubenheimer, "Method to Evaluate Steering and Alignment Algorithms for Controlling Emittance Growth", Presented at the 1993 IEEE Part. Acc. Conf., Washington D.C. (1993).

[Assmann 1995] R. Assmann, C. Adolphsen, K. Bane, T.O. Raubenheimer, R. Siemann, K. Thompson, "LIAR: A Computer Program for Linear Collider Simulations", SLAC–AP–NOTE–103 (1996); to be published as a SLAC–REPORT.

[Balakin 1983] V. Balakin, A. Novokhatsky, V. Smirnov, "VLEPP: Transverse Beam Dynamics", Proceedings of the 12th Int. Conf. on High Energy Accelerators, Fermilab, 119 (1983).

[Bane 1980a] K. Bane and P. Wilson, "Longitudinal and Transverse Wake Potentials in SLAC", Proceedings of the 11th Int. Conf. on High Energy Accelerators, CERN, Birhäuser Verlag, Basel, 592 (1980).

[Bane 1980b] K. Bane and B. Zotter, "Transverse Modes in Periodic Cylindrical Cavities", Proceedings of the 11th Int. Conf. on High Energy Accelerators, CERN, Birhäuser Verlag, Basel, 581 (1980).

[Bane 1993] K.L.F. Bane and R.L. Gluckstern, "The Transverse Wakefield of a Detuned X-Band Accelerating Structure", *Particle Acclerators* **42**, 123 (1993).

[Bane 1994] K.L.F. Bane, C. Adolphsen, K. Kubo, and K.A. Thompson, "Issues in Multibunch Emittance Preservation in the NLC", Fourth European Particle Accelerator Conference, London, England, (June 27-July 1, 1994).

[Bane 1995] K. Bane, "The Short-range NLC Wakefields", NLC–Note 9, (February 1995).

[Bowden, 1996] G. Bowden, P. Holik, S.R. Wagner, G. Heimlinger, R. Settles, "Precision magnet movers for the Final Focus Test Beam", *Nucl. Instr. and Methods* **368A**, 579–592, (1996).

[Brandt 1982] D. Brandt and B. Zotter, "Calculation of the Wakefield with the Optical Resonator Model", CERN-ISR/TH/82-13 and LEP Note 388 (1982).

[Brandt 1984] D. Brandt, "Optical Resonator Model for the Wakefields of the Deflecting mode $m = 1$", CERN-LEP Note 484 (1984).

[Gluckstern 1989] R. Gluckstern, "Longitudinal Impedance of a Periodic Structure at High Frequency", *Phys. Rev. D* **39**, 2780 (1989).

[Heifets 1989] S.A. Heifets and S. Kheifets, "High-frequency Limit of the Longitudinal Impedance of an Array of Cavities", *Phys. Rev. D* **39**, 960 (1989).

[Keil 1972] E. Keil, "Diffraction Radiation of Charged Rings Moving in a Corrugated Cylindrical Pipe", *Nucl. Instr. and Methods* **100**, 419 (1972).

[Kroll 1994] N. Kroll *et al.*, "Manifold damping of the NLC detuned accelerating structure", 6th Workshop on Advanced Accelerator Concepts, Lake Geneva, WI, June 12-18, (1994).

[Palmer 1990] R. Palmer, "A Qualitative Study of Wakefields for Very Short Bunches", *Particle Acclerators* **25**, 97 (1990).

[Panofsky 1956] W. Panofsky and W. Wenzel, "Some Considerations Concerning the Transverse Deflection of Charged Particles in Radio-frequency Fields", *Rev. Sci. Instr.* **27**, 967 (1956).

[Raubenheimer 1992] T.O. Raubenheimer and P. Chen, "Ions in the Linacs of Future Linear Colliders", presented at LINAC 92, Ottawa, (1992).

[Raubenheimer 1995] T.O. Raubenheimer and F. Zimmermann, "A Fast Beam-Ion Instability in Linear Accelerators and Storage Rings", *Phys. Rev. E* **52**, 5487 (1995).

[Schnell 1987] W. Schnell, "Microwave Quadrupoles for Linear Colliders", CERN-LEP-RF/87-24, (1987).

[Schnell 1991] W. Schnell and I. Wilson, "Microwave Quadrupole Structures for the CERN Linear Collider", Proc. of the 1991 IEEE Particle Acc. Conf., San Francisco, 3237, (1991).

[Thompson 1990] K.A. Thompson and R.D. Ruth, "Controlling transverse multibunch instabilities in linacs of high energy linear colliders", *Phys. Rev. D* **41**, 964 (1990).

[Thompson 1993] K.A. Thompson and R.D. Ruth, "Simulation and Compensation of Multibunch Energy Variation in NLC", in Proceedings of 1993 Particle Accelerator Conference, Washington, D.C. (17–20 May 1993).

[Thompson 1994] K.A. Thompson *et al.*,, "Design and Simulation of Accelerating Structures for Future Linear Colliders", *Particle Acclerators* **47**, 65 (1994).

[Weiland 1983] T. Weiland, "On the Computation of Resonant Modes in Cylindrically Symmetric Cavities", *Nucl. Instr. and Methods* **216**, 329 (1983).

Contributors

- Chris Adolphsen
- Roberto Aiello
- Ralph Assmann
- Karl Bane
- Gordon Bowden
- Franz Josef Decker
- Linda Hendrickson
- Tom Mattison
- Kiyoshi Kubo
- Yuri Nosochkov
- Tor Raubenheimer
- Kathy Thompson
- Dave Whittum
- Frank Zimmermann